Computational Vorticoacoustic Stability Analysis of the Bidirectional Vortex Engine

by

Paul Andrew Kovacic

A thesis submitted to the Graduate Faculty of
Auburn University
in partial fulfillment of the
requirements for the Degree of
Master of Science

Auburn, Alabama
May 7, 2016

Keywords: aeroacoustics, stability, vortex

Approved by

Joseph C. Majdalani, Chair, Professor and Department Chair of Aerospace Engineering
Roy J. Hartfield, Woltosz Professor of Aerospace Engineering
David E. Scarborough, Assistant Professor of Aerospace Engineering
Joshua W. Batterson, Director of Modeling & Simulation, Gloyer-Taylor Laboratories

Abstract

Since the invention of combustion-based propulsion systems, the presence of resonating, broadband waves has often been associated with the onset of a phenomenon known as "combustion instability." These waves commonly take the form of pressure oscillations in the combustion chamber, reaching amplitudes that can match or even exceed that of the mean chamber pressure. Left unabated, these oscillations can affect the system's overall performance, dramatically increase heat transfer to the chamber walls and injector faceplates, and, in some cases, compromise the structural integrity of the entire propulsion system. Treatment of the problem entails determining potential instabilities during the design phase of the engine. Oftentimes, mitigation efforts lead to program cancellation due to the excessive amount of testing and engine redesigns that follow. Thus, there is a strong need to develop the necessary computational tools to analyze complex propulsion systems that can effectively and accurately determine the stability of large chambers, while also minimizing both computational and financial costs.

The present study of a bidirectional vortex engine seeks to illuminate one such tool, which utilizes a linearized, energy-based approach to analyze the acoustic, vortical, and energy fields within the combustion chamber. By computationally discretizing field values across the domain by means of a finite differencing scheme, the tool enables us to return the stability margins of the chamber-specific modes in a relatively short amount of time. The results of this study show that the steep temperature gradient across the shear layer between the primary driving vortices, as well as the high density areas immediately surrounding the inlets, dramatically affect the acoustics of the system. In addition to the primary shear layer, secondary vortex cells can have an appreciable impact on instability. The stability calculations reveal that the first pure tangential mode of 1243 Hz is the most unstable mode, while the first longitudinal mode of 1321 Hz will be stable. Though the thermodynamic nature of this engine creates a unique acoustic environment, the instability of the tangential modes follows suit with traditional, axially-driven liquid rocket engines, where the prevalent modes are often those oscillating tangentially. Thus, while unable to recover the nonlinear, limit-cycle amplitudes of the resonating waves, the presently used linearized approach may be perceived as an efficient method to pinpoint the specific modes and associated physical mechanisms within the chamber that contribute to combustion instability in a rocket engine.

Acknowledgments

It is truly humbling to think about all of those who have poured into me throughout my life and shared their contagious passion for lifelong learning with me, to the point that I am now able to be completing a document such as this. As such, there are numerous individuals who warrant recognition, but there are a few who deserve special acknowledgment.

First, to my immediate and extended family, thank you for your unwavering support of me over the course of my life, especially during my college years. It is a testament to your steadfast parenting, dedication, and love, that I have reached this point in my life, both academically and personally. All of you truly mean the world to me.

To Mrs. Barbara Hart, Mr. Darrick Bowman, Mrs. Myra O'Steen, and my mom, thank you for your dedication to your professions of passing on knowledge, wisdom, and passion to me and many other generations of your students. From marigolds and Saturn V outlines to journal writing time and discussion time, I owe an enormous debt of gratitude to each of you for instilling in me a spark of unquenchable curiosity and thirst for seeking both knowledge and wisdom.

Lastly, to Dr. Josh Batterson, Dr. Joe Majdalani, and the faculty and staff of the Auburn University Department of Aerospace Engineering, thank you for your invaluable teaching, mentoring, and input into this document and my academic career in general. I will forever carry the Auburn University name with a sense of great pride.

Table of Contents

List of Figures

List of Tables

List of Abbreviations

$\bar{q}$	instantaneous flow variable denotation
β	phase
$\boldsymbol{u}$	velocity
$\mathbf{\Omega}$	vorticity
$\boldsymbol{\psi}$	viscous stress vector
$\mathcal{H}$	total enthalpy
$\hat{q}$	acoustic field variable denotation
κ	coefficient of thermal conducitivity
μ	dynamic viscosity
ω	frequency
ϕ	dissipation function
ρ	density
σ	scalar potential
$\mathbf{A}$	vector potential
$\tilde{q}$	vortical field variable denotation
φ	acoustic velocity potential
ζ	second coefficient of viscosity

D	energy source terms
E	system energy
F	vector field
G	Rayleigh index
J	Bessel function
M	injection Mach number
m	mode number
n	mass flux
P	period
p	pressure
Q	heat
q	generic flow variable magnitude
q'	fluctuating quantity denotation
q_m	flow variable modal magnitude
R	specific gas constant
r	spatial coordinate
s	entropy
T	temperature
t	time
V	total volume

W	work
α_m	modal linear stability
a_0	speed of sound
c_p	specific heat
k_l	longitudinal wave number
k_{mn}	transverse wave number
k_m	tangential wave number
k_n	radial wave number
q_0	mean flow variable denotation
R_m	total modal amplitude function

Chapter 1

Introduction

At the core of chemical-based propulsion systems is the combustion process, which causes a highly energetic release of the stored energy in the chemical bonds of the fuel. Ultimately, this propels the system forward through a transfer of momentum between the gaseous products and the propulsion device itself. The combustion process and the resulting flow exiting the combustion region is naturally unsteady due to the inherent random fluctuations in flow properties such as pressure, temperature, and velocity. Many times, these random fluctuations can be seen in liquid propulsion systems with no material consequences. At other times, these random fluctuations drive large amplitude pressure waves that are energized by a coupling between the combustion process and the flow itself. The resulting oscillations are often manifested at distinct frequencies that are specific to the chamber geometry and, to a lesser extent, the mean flow [1]. When these oscillations reach at least 10% of the mean chamber pressure [2], a phenomenon known as "combustion instability" occurs [3], in contrast to the random, unforced fluctuations that have no significant time-dependent growth. This terminology is somewhat a misnomer, as the combustion process itself is not the only driver. Rather, it is the emergence of pressure oscillations, or resonant waves, in the combustion chamber that is of concern in combustion instability. The corresponding resonant waves can occur over a broad range of frequencies, but for simplicity's sake, are generally classified as either existing in a low or high frequency range.

The low-range frequencies are those that are approximately a few hundred cycles per second or less. Commonly referred to as "chugging," these waves are mostly spatially invariant and exhibit coupling primarily with variations in the feed system. As a result, the mixture ratio and flow rates of the incoming propellant can be significantly altered, causing reduced engine performance. Although this unsteadiness can be controlled by a damping system that is attached to the feed lines, the oscillations can couple with the natural modes of larger systems, or even the entire vehicle, to the extent of causing intense axial vibrations that can damage or destroy the larger systems in the vehicle. To overcome these structural "pogo" oscillations, the natural frequencies of the overall vehicle structure and the engine itself are widely separated by engine designers in order to suppress coupling mechanisms [4].

An intermediate range exists between the high and low frequency categories, though these resonant waves are of lesser concern. Known as "buzzing," these medium-range frequency entropy waves emerge as a coupling between the combustion process and the injection system. They are named as such due to axial mixture ratio gradients that cause a reflected pressure wave which, in turn, becomes a discontinuity in the entire chamber's mixture ratio gradient. Thus, occurring at the same velocity as the mean flow, this pressure wave creates an entropy discontinuity physically manifested as a buzzing instability [5]. Though these waves are not normally destructive themselves, they can promote the emergence of waves in the high frequency range [6].

When frequencies reach several hundred cycles per second and higher, "screeching" waves develop as energy released by the combustion process couples with the resonance properties of the combustion chamber geometry. In fact, the frequencies at which these waves occur are usually similar to those of a natural organ pipe with acoustic modes that could occur even in the absence of combustion, and are thus often referred to as "acoustic" combustion instabilities. The appearance of these waves, with pressure fluctuations sometimes much greater than 100% of the steady state chamber pressure [7], can in some cases, result in severe structural vibrations, greatly increased heat transfer to critical engine parts such as the injector faceplate, or outright catastrophic failure of the entire engine [8, 9].

A defining characteristic of the high-frequency instabilities is not only at what frequency they resonate, but what shape they take in the combustion chamber. The resonant waves can take the shape of either pure longitudinal, radial, tangential modes, or some combination

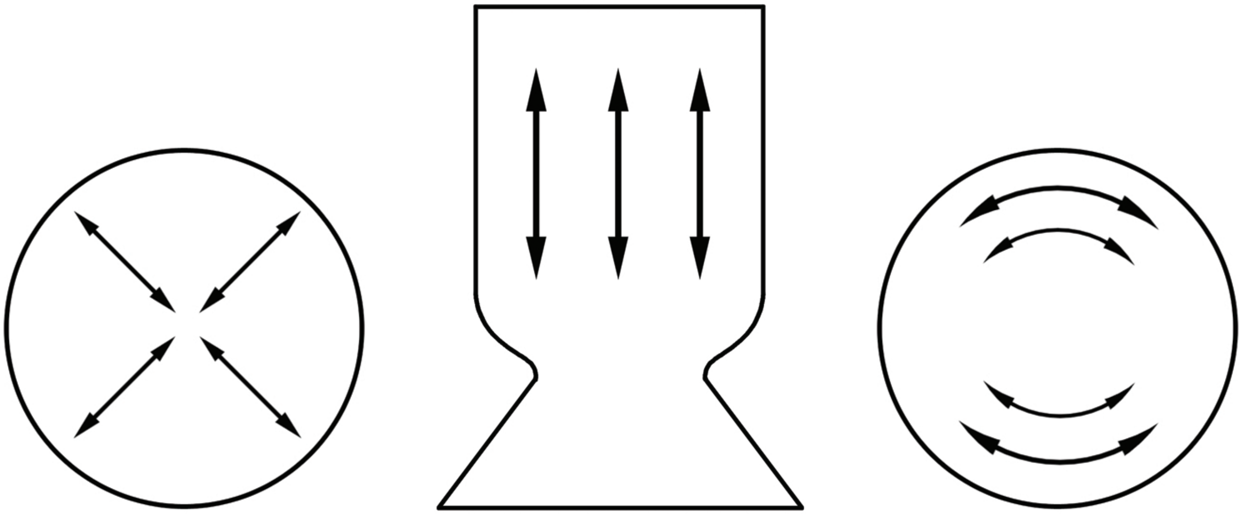

(a) First Radial Mode. (b) First Longitudinal Mode. (c) First Tangential Mode.

Figure 1.1: Mode shapes in a cylindrical combustion chamber.

thereof as shown in Figure 1.1. Experience has shown that tangential modes tend to be the most commonly reported in the developmental stages of liquid rocket engine design and testing, while longitudinal modes prevail in solid rocket motors. These modes usually result in the most damage, especially in the liquid-propelled engine case, where pressure nodes form at the highly sensitive injector faceplate [4].

The final, and perhaps most important, defining characteristics of the oscillating pressure waves are their amplitudes and respective growth rates. Whether the instabilities arise from the infinitesimal fluctuations inherent to real flows, or are triggered from an impulse in the flow, experience has shown that complex nonlinear effects govern how the amplitude grows in time and what limit-cycle amplitude the wave finally reaches under steady-state conditions. Flow nonlinearities can also lead to other related phenomena, such as wave steepening, where changes in the local speed of sound cause acoustic waves to converge to a shock-like structure. As a result of the work done on the fluid by the steepened wave moving throughout the combustor, a positive shift in the mean chamber pressure can occur with potentially detrimental effects on the engine [1,10].

Though clearly nonlinear considerations are crucial to understanding the evolution of resonant waves in combustion chambers, they also make obtaining any type of analytical solution exceedingly difficult. Historically, the primary method to combat this issue has been to linearize the fluid dynamics equations in order to make the problem analytically tractable. However, by doing so, several features of resonant waves are lost. Namely, the limit cycle amplitude cannot be recovered, as a linear analysis would suggest that the resonant wave grows exponentially without bound. Furthermore, much experimental data consists of pressure measurements made when the combustor has reached a steady-state equilibrium [11]. Consequently, this makes comparing linear theory to experimental results difficult. However, a linearized approach provides a useful, albeit limited, glimpse into the mechanics of instability by producing a parameter that accounts for whether the individual resonant modes decay or grow with time and how quickly that occurs. By analyzing this parameter for each mode present, a total stability diagnosis can be determined for a given combustor geometry and flow conditions. Thus, while the stability of a combustor can be estimated, the linear approach results in a linear differential equation that describes the amplitude growth of a given mode as going to infinity. Furthermore, this unrealistic amplitude reveals no information about the energy cascade into higher modes, which is a phenomenon that occurs as energy in the lower modes spills into higher modes and causes the resonant wave to reach its limit cycle amplitude. Nonetheless, given that the complete nonlinear model remains strongly tied to the linear model, it stands to reason that a thorough understanding of the inner workings of linear instability is justified not only as an academic interest, but also as a necessary component of modeling combustion instability through recovering the stability margin of each mode present [1].

To summarize, it is evident that an efficient approach that not only captures nonlinear wave growth, but also the various modal contributions, is the ultimate goal in the field of combustion instability. However, a linear approach can provide insight into the stability margins of a combustor without having to deal with the roadblock of nonlinearity. Whatever the approach, the emergence of resonant waves in large combustors continues to stand as arguably one of the most unresolved obstacles that is consistently reported in the developmental stages of new propulsive systems.

1.1 Historical Background

The extensive history of combustion instability began in 1777, when the Irish physician Brian Higgins [12], while attempting to produce water from burning oxygen and hydrogen in a jar, stumbled upon an unexpected phenomenon. He found that when he inserted a flame into an open-ended glass tube, a clear sound was produced. Furthermore, he discovered that as he tried tubes of various widths, lengths, and radii, the flame could be diminished and the pitch of resulting sound could be altered. After his findings were published, others observed similar phenomena, such as the "dancing flame" discovered by Le Conte [13] who, while attending a musical performance, noted that a gas burner near the piano exhibited fluctuations that were precisely synced with the beat of the music. He was so struck by this occurrence that he remarked, "A deaf man might have seen the harmony." Perhaps the most commonly used example, though, is that of the Rijke tube. Discovered in 1859 by P. L. Rijke [14], the Rijke tube consisted of a heated metal gauze placed about a quarter length up inside an open vertical tube. Upon heating the gauze with a flame or electrical current [15], a loud sound would be emitted from the tube. Though these examples differ in energy sources and boundary conditions, the underlying theme of self-excited oscillatory behavior is the defining characteristic that attracted the greatest academic interest. Throughout the following years, there were many attempts to explain the connections between sound and flame behavior. One explanation put forth was by de la Rive [16], who came to the conclusion that the sound produced was the result of water vapor that periodically condensed on the tube. This idea was soon refuted by Faraday [17], who disproved de la Rive's explanation by performing the same experiment while using a carbonic oxide flame, which did not produce water. Faraday instead posited that there were periodic explosions caused by the mixing of gas and air that produced the sound. Still other theories [18–20] circulated in later years, but it was not until 1877 that Rayleigh [21–23] rightly determined the phase lagging between heat release and the resonant acoustic wave. He found that when the heat was released at maximal wave compression, the acoustic wave would grow. However, should heat be released when the acoustic wave's amplitude reached a peak, the oscillations would be damped. In effect, he was describing the Carnot engine cycle, in which the combustion process works on the acoustic field in the tube instead of a piston. An important ramification of Rayleigh's observation is that if heat is released at a pressure oscillation node, no contribution is made whatsoever to the pressure oscillation [6]. This concept of phase coupling between combustion and acoustic oscillation became known as the Rayleigh criterion, which is described in the following equation:

$$G\left(x\right) = \frac{1}{P} \int\limits_{P} Q'\left(x,t\right) p'\left(x,t\right) dt \tag{1.1}$$

where the Rayleigh index, $G(x)$, is maximized when pressure fluctuations and heat release rates happen to be in phase.

While the connection between the flame and sound remained only an academic curiosity in the 1800s, the dawn of the Industrial Revolution sparked renewed interest in the subject as industrial burners, pulsed combustors, and other combustion devices began to exhibit some of these same phenomenal characteristics. In some cases, the reported instabilities were even considered desirable, as they increased the efficiency in devices such as heat exchangers, oil refineries, and gas-heating machines [15]. However, it was the development of the modern rocket engine that really spurred much of the technical interest in this subject. Among the first to document instabilities in rocket engines was a group of scientists in 1940 [11]; these researchers found that pressure amplitudes in a solid rocket motor combustion chamber can exceed twice that of the predicted values. Interest during World War II was limited primarily to tactical solid rocket motors, then expanded to include the newly developed intercontinental ballistic missiles [24]. Most of the research performed during this period was focused on the linear regime of instability, which was concerned with infinitesimally small pressure disturbances that occur naturally [11]. Foundational work during this time includes the studies of Crocco [25], Hart and McClure [26, 27], Hart and Cantrell [28], Cantrell and Hart [29], Culick [30, 31], and Scala [6], all of whom sought to reveal the connection between resonant acoustic waves and oscillatory motion in combustion chambers.

The daunting charge by John F. Kennedy to land a man on the moon by the close of the 1960s quickly escalated combustion instability research to full force during the Apollo Era. Out of this time period came perhaps one of the most widely cited examples of a successful bout with combustion instability, the F-1 engine shown in Figure 1.2, which was the towering main stage engine used in the Apollo program. From the early stages of development, the F-1 engine was plagued by combustion instabilities as a result of pressure fluctuations well above 100% of the mean pressure. Particularly, the injector faceplate would typically become eroded by strong tangential and radial resonant waves. Understanding the urgency of the situation, engineers spearheaded a program in 1962 known as "Project First," which made focused attempts to address these issues. At the conclusion of this effort four years later, scientists had performed over 2000 full-scale engine tests related to combustion instability mitigation efforts. Much of the testing included changing the injector pattern, as well as analyzing several different baffle designs, all with the intent that the changes would placate the resonant waves [32]. However, by late 1964, the combustion instability problem was brought under control, both from linear and impulsive, nonlinear disturbances that might occur in the normal operation of the engine. In fact, even when artificial, impulsive instability was induced in the engine, the engine would damp out within a fraction of a second [33]. The F-1 engine was thus man-rated and declared flight-ready several years before the first Saturn V vehicle would take flight [32], thus concluding one of the most expensive combustion instability studies ever undertaken [34].

(a) Rocketdyne F-1 engine exterior [35].

(b) Injector faceplate with the addition of baffles [36].

Figure 1.2: The Rocketdyne F-1 engine.

1.2 Modern Approaches

The early investigations into combustion instability were almost exclusively experimental in nature, focusing on a trial-and-error approach to stabilizing engines. However, it became clear that an analytical approach was necessary to fully understand and predict the onset of instability in the future. Thus, many studies, such as those performed by Scala [6], Reardon [7], and Culick [30], probed into the inner workings of what caused the resonant waves and how they might be attenuated at any stage of engine design. Due to the inherent nonlinearities of the flow, many of these frontier works were based on linear assumptions, where instabilities were assumed only to arise from infinitesimal flow fluctuations, not impulsive triggers [11]. Realizing this notable shortcoming, Priem [37], Povinelli [38], and others, sought to encompass the complete set of one dimensional governing equations. The end result of these and many other analytical studies was to lay the foundation for the establishment of stability models of simplified geometric chambers that exhibit Helmholtz-type acoustic modes. Concurrently, combustion instability experiments played an important role in both validating analytical and computational approaches as well as highlighting areas of interest that may not have been seen otherwise. Some, such as Brownlee and Marble [39], Temkin [40], and Chester [41] focused on how longitudinal waves formed and what structure they took. Still others, such as Crocco [42], Reardon, Crocco, and Harrje [7, 43], Krieg [44], and Heidmann [45], sought to understand how transverse waves affected stability.

While combustion instability research largely fell by the wayside in the 1970s and early 1980s, it began to pick up momentum in the the late 1980s with focused efforts on low frequency instabilities in ramjets [24] and vortex shedding as a contributor to instability as shown with the incidents of the Minuteman III third stage [46] and the space shuttle solid rocket boosters' instabilities [47]. This encouraged many researchers, such as Majdalani [48–52] and coworkers (Akiki [53, 54], Batterson [55, 56], Elliott [57–59], Fischbach [60–62], Flandro [63], and Haddad [64, 65]), Casalis [66] and coworkers (Griffond [67, 68], Chedevergne [69, 70], Boyer [71, 72]), and others to study how vorticity production at resonant frequencies affected stability. Traditionally, the vortical wave had been treated as simply an "acoustic boundary layer" [73]. However, the problem of this boundary layer shedding discrete vortex cells into the mean flow led Majdalani [50] and Majdalani and Flandro [51] to develop a framework that accurately described the physical connection between the traditionally understood acoustic modes and the vortical wave at their respective frequencies. This framework found confirmation in both computational fluid dynamics simulations [74] and experiments [75]. More recently, some studies [64, 65] have sought to illuminate the spatial dependence of transverse waves by means of an asymptotic framework that also captured vortical wave development along the sidewall and headwall of a combustion chamber. These, and other, analytical models play an important role in the understanding of general design trends that might be more prone to instability. However, an important caveat with analytical models is that they all must be simplified to a rough approximation of the real chamber mean flow and geometry. Attempting to move beyond this to include varying geometry or injection properties removes the possibility for analytically tractable solutions.

Thus, while these analytical studies lay important groundwork for stability analysis, computational simulations of real systems that have been made realistically possible through increased modern computing power enables us today to solve the complete set of fluid dynamic equations with fewer limitations than those used to develop analytical solutions. This approach has allowed for nonlinear considerations to be taken into account, whether through reduced-order modeling [24] or complete direct numerical simulations [76]. However, to easily break down the total flow field into the various acoustic modes, a linear approach remains essential. The linear formulation that we pursue not only serves to computationally resolve a complex chamber geometry, but to double as a rapid design optimization tool. Ultimately, this approach stands as the next logical step toward understanding and using vorticoacoustic solutions in real engineering design and stability analyses of modern rocket engines.

Chapter 2

General Formulation

The technique used in the present study can be traced to foundational work outlined by Chu and Kovsznay [77], who realized that the total instantaneous flow field can be broken into a linear combination of a mean flow component and a linearly-independent unsteady disturbance. If any changes in the mean flow component occur at least over several unsteady periods, the steady and unsteady flow field components could then be treated as locally time independent of each other. Furthermore, Chu and Kovsznay found that the first order unsteady disturbance was comprised of "mass-like," "force-like," and "heat-like" components, which respectively represented the acoustic, vortical, and entropy waves in a given system. Mathematically, a representative, instantaneous flow variable, $\bar{q}$, may be decomposed into

$$\bar{q} = q_0(\mathbf{r}, t) + q_1(\mathbf{r}, t, \omega_m t) \tag{2.1}$$

where t represents the slow time scale and ω_m represents the fast time scale of the unsteady component. Breaking down q_1 gives

$$q_1(\mathbf{r}, t, \omega_m t) = \hat{q} + \tilde{q} + \overset{\smile}{q} \tag{2.2}$$

where $\hat{q}$ is the acoustic field, $\tilde{q}$ is the vortical field, and $\overset{\smile}{q}$ is the entropy field. The resonance field of greatest importance is the acoustic field, which has long been established as the significant contributor to combustion instability problems. The vortical and entropy field are acoustically-driven fields which evolve in tandem with the acoustic field at its specific resonant frequencies. These acoustic waves, which are manifestations of an eigensolution, physically reveal themselves as resonant modes of the combustion system, where they are strongly tied to the effects of thermodynamic variables, the chamber geometry, and the mean flow. The vortical field enters into the picture as a Stokes-like boundary layer correction to the irrotational acoustic wave in order to satisfy the no-slip condition. In some instances, however, the unsteady vorticity generated at the solid boundaries of the chamber can be convected into the chamber due to the influence of the mean flow [48, 63, 73]. Together, these two fields make up the vorticoacoustic wave. It can be shown that, for ideal cases, the vortical pressure, density, and temperature appear at two orders of magnitude below the velocity and can, therefore, arguably be ignored [78]. This assumption leads to the conclusion that the presence of combustion or compressible effects influences the development of the vortical field to a negligible degree, a concept that is backed up both by experimental [75] and numerical [74, 79] studies.

In a similar manner to the vortical field, the entropy field is driven by the acoustic motion within the combustion zone and can be a primary source of instability. It has been shown that the combustion related phenomena that the entropy field seeks to capture, such as temperature fluctuation, heat release, and heat transfer, can be significant and must be considered in order to form a complete model [80, 81]. Furthermore, there can be cross-contributions between the unsteady entropy and velocity in a system, where unsteady entropy and temperature fluctuations are generated from the vortical field and, as such, can themselves generate unsteady velocity. These cross-contributions, however, tend to be relatively negligible in light of the dominating contributions of unsteady entropy and velocity to their own respective fields [82].

2.1 Linear Decomposition

In order to derive the equations that define the vorticoacoustic and entropy fields, the instantaneous flow field must first be defined through the following compressible conservation equations of continuity,

$$\frac{\partial \bar{\rho}}{\partial t} + \bar{\boldsymbol{u}} \cdot \nabla \bar{\rho} + \bar{\rho} \left(\nabla \cdot \bar{\boldsymbol{u}} \right) = 0 \tag{2.3}$$

momentum,

$$\bar{\rho}\left(\frac{\partial \bar{\boldsymbol{u}}}{\partial t}+\bar{\boldsymbol{u}}\cdot\nabla\bar{\boldsymbol{u}}\right)+\nabla\bar{p}=\mu\left[\frac{4}{3}\nabla\left(\nabla\cdot\bar{\boldsymbol{u}}\right)-\nabla\times\left(\nabla\times\bar{\boldsymbol{u}}\right)\right] \tag{2.4}$$

energy,

$$\bar{\rho}c_p\left(\frac{\partial \bar{T}}{\partial t}+\bar{\boldsymbol{u}}\cdot\nabla\bar{T}\right)=\frac{\partial\bar{p}}{\partial t}+\bar{\boldsymbol{u}}\cdot\nabla\bar{p}+\kappa\nabla^2\bar{T}-\nabla\cdot\bar{q}+\frac{\partial\bar{Q}}{\partial t}+\bar{\Phi} \tag{2.5}$$

and state.

$$\bar{p}=\bar{\rho}R\bar{T} \tag{2.6}$$

As shown in Eq. (2.1), all instantaneous flow variables can be broken down into mean and unsteady components as shown below.

$$\begin{cases}\bar{p}\left(\boldsymbol{r},t\right)=p_0\left(\boldsymbol{r},t\right)+p_1\left(\boldsymbol{r},t,\omega t\right)\\ \bar{\rho}\left(\boldsymbol{r},t\right)=\rho_0\left(\boldsymbol{r},t\right)+\rho_1\left(\boldsymbol{r},t,\omega t\right)\\ \bar{\boldsymbol{u}}\left(\boldsymbol{r},t\right)=\boldsymbol{u}_0\left(\boldsymbol{r},t\right)+\boldsymbol{u}_1\left(\boldsymbol{r},t,\omega t\right)\\ \bar{T}\left(\boldsymbol{r},t\right)=T_0\left(\boldsymbol{r},t\right)+T_1\left(\boldsymbol{r},t,\omega t\right)\\ \bar{q}\left(\boldsymbol{r},t\right)=q_0\left(\boldsymbol{r},t\right)+q_1\left(\boldsymbol{r},t,\omega t\right)\\ \bar{\Phi}\left(\boldsymbol{r},t\right)=\Phi_0\left(\boldsymbol{r},t\right)+\Phi_1\left(\boldsymbol{r},t,\omega t\right)\end{cases} \tag{2.7}$$

Thus, substituting Eq. (2.7) into Eqs. (2.3), (2.4), (2.5), and (2.6), the total unsteady field is recovered, as shown here by the unsteady continuity,

$$\frac{\partial\hat{\rho}}{\partial t}+\hat{\boldsymbol{u}}\cdot\nabla\rho_0+\boldsymbol{u}_0\cdot\nabla\hat{\rho}+\hat{\rho}\nabla\cdot\boldsymbol{u}_0+\rho_0\nabla\cdot\hat{\boldsymbol{u}}=0 \tag{2.8}$$

unsteady momentum,

$$\begin{aligned}&\rho_0\left[\frac{\partial\hat{\boldsymbol{u}}}{\partial t}+\nabla\left(\boldsymbol{u}_0\cdot\hat{\boldsymbol{u}}\right)-\hat{\boldsymbol{u}}\times\nabla\times\boldsymbol{u}_0-\boldsymbol{u}_0\times\nabla\times\hat{\boldsymbol{u}}\right]\\ &+\hat{\rho}\left(\frac{\partial\boldsymbol{u}_0}{\partial t}+\frac{1}{2}\nabla\boldsymbol{u}_0\cdot\boldsymbol{u}_0-\boldsymbol{u}_0\times\nabla\times\boldsymbol{u}_0\right)+\nabla\hat{p}=\mu\left[-\nabla\times\nabla\times\hat{\boldsymbol{u}}+\frac{4}{3}\nabla\left(\nabla\cdot\hat{\boldsymbol{u}}\right)\right]\end{aligned} \tag{2.9}$$

unsteady energy,

$$\begin{aligned}&\rho_0 c_p \left(\frac{\partial \hat{T}}{\partial t} + \boldsymbol{u}_0 \cdot \nabla \hat{T} + \hat{\boldsymbol{u}} \cdot \nabla T_0 \right) + \hat{\rho} c_p \left(\frac{\partial T_0}{\partial t} + \boldsymbol{u}_0 \cdot \nabla T_0 \right) \\ &= \frac{\partial \hat{p}}{\partial t} + \boldsymbol{u}_0 \cdot \nabla \hat{p} + \hat{\boldsymbol{u}} \cdot \nabla p_0 + \kappa \nabla^2 \hat{T} - \nabla \cdot \hat{q} + \frac{\partial \hat{Q}}{\partial t} + \hat{\varphi}\end{aligned} \tag{2.10}$$

and unsteady state equations.

$$p_1 = R \left(\rho_0 \hat{T} + \hat{\rho} T_0 \right) \tag{2.11}$$

2.2 Nonlinear Considerations

Though this general formulation for stability analysis is centered around the linear decomposition of the instantaneous field, it is worth a brief aside to explain what a nonlinear analysis would entail and the justification behind the linear approach as performed in the present study.

Starting with Eq. (2.1), there is a more general form of the equation that can be written as shown below.

$$\bar{q}\left(\boldsymbol{r}, t, \omega_m t\right) = q_0\left(\boldsymbol{r}, t\right) + \sum_{m=1}^{\infty} q_m\left(\boldsymbol{r}, t, \omega_m t\right) \tag{2.12}$$

As previously outlined, the resulting terms from the first order expansion capture the effects of the unsteady field based on the short and long time scales associated with acoustics. Effects at q_2 are generally assumed negligible through scaling arguments. It is not until q_3 is reached that nonlinear effects appear and the wave steepening process is captured. Thus, the physical, time-dependent amplitudes of the resonant waves can then be recovered [10].

There are two broad categories dealing with the nonlinearities of physical wave growth. The first is a linear decomposition, as outlined in the present study, that allows for each of the modes to be easily recovered by means of an eigensolver and analyzed for their respective contributions to the total unsteady energy transfer [83]. The caveat here is that, as previously mentioned, the ability to recover the physical wave amplitude is lost. Furthermore, the linear approach only allows for one-way coupling, where the mean flow affects the unsteady component, but not the reverse, which would be referred to as two-way coupling [69]. The second category is a thorough direct numerical simulation of the entire nonlinear wave equation. While revealing the physical wave amplitude, this approach can have the downside of hiding individual modal contributions to unsteady energy transfer. Effectively, it provides the entire solution without detailing anything about the composition of that solution. Thus, the ultimate end is to combine both approaches in such a way as to determine the true total amplitude, along with all contributing modes and their interactions with each other. This approach has been pursued by Culick [84] and Wicker et al. [85], and more recently by Sirignano and Popov [8] and Jacob et al. [86].

Chapter 3

Acoustic Field Formulation

3.1 Helmholtz Solutions

As a straightforward baseline comparison, simple Helmholtz solutions serve a purpose primarily for computing and validating resonant frequency calculations with complex geometries and mean flows [87]. These solutions are derived from the following classical wave equation,

$$a_0^{-2}\frac{\partial^2 \varphi}{\partial t^2} - \nabla^2 \varphi = 0 \tag{3.1}$$

where the acoustic potential can be related to a field variable [88], such as velocity or density. Then, solving Eq. (3.1) results in the well-established suite of Helmholtz solutions, where the variance in variables is due only to how the boundary conditions are defined.

As an example pertinent to rocket chamber geometry, the Helmholtz solution for an axisymmetric cylinder is known to be

$$\begin{cases} \hat{p} = R_m \sin(\omega_m t)\, J_m(k_{mn} r) \cos(m\theta) \cos(k_l z) \\ \hat{u}_r = R_m k_{mn} (\rho_0 \omega_m)^{-1} \cos(\omega_m t)\, J'_m(k_{mn} r) \cos(m\theta) \cos(k_l z) \\ \hat{u}_\theta = -R_m m (\rho_0 \omega_m r)^{-1} \cos(\omega_m t)\, J_m(k_{mn} r) \sin(m\theta) \cos(k_l z) \\ \hat{u}_z = -R_m k_l (\rho_0 \omega_m)^{-1} \cos(\omega_m t)\, J_m(k_{mn} r) \cos(m\theta) \sin(k_l z) \end{cases} \tag{3.2}$$

where the frequency is defined by $\omega_m = a_s \lambda_m$, $\lambda_m \equiv \sqrt{k_{mn}^2 + k_l^2}$, and the transverse and longitudinal wave numbers are denoted by k_{mn} and k_l, respectively. This formulation of the acoustic field finds its roots in several foundational studies performed by Hart [26–28], Cantrell [29], and Culick [30, 31] in the late 1950s and early 1960s.

3.2 Convected Acoustic Wave Equation

Easily-recoverable solutions to the classic wave equation are limited in their applicability to resonant waves in combustion chambers for several reasons. The most pressing issue is that mean flow effects are not accounted for in this equation. Thus, most approaches use a mean-flow-corrected wave equation [88, 89] which captures either a one-way or two-way coupling between the steady and unsteady fields. This approach has been applied to various problems in aeroacoustics, such as the cavity flow problem, where the speed of sound encapsulates the varying thermodynamic properties of the flow. Generally, this approach utilizes the velocity potential formulation of the acoustic wave, where the velocity potential, φ, is defined as a scalar function whose gradient satisfies the irrotationality condition,

$$\nabla \times A = 0 \tag{3.3}$$

which, from the following vector identity,

$$\nabla \times (\nabla \varphi) = 0 \tag{3.4}$$

it follows that,

$$A = \nabla \varphi \tag{3.5}$$

leading to the common description of the acoustic field as being irrotational and isentropic [80]. Therefore, with the irrotationality condition, the conservation equations of fluid dynamics are combined together to form the “Convected Wave Equation” [88], also known as the “Acoustic Velocity Potential Equation” [90, 91].

The Convected Wave Equation can be derived in a few ways, namely, through a potential flow, energy-based formulation as shown in Appendix C, and a different approach, which starts with the unsteady conservation Eqs. (2.8)-(2.11). According to Helmholtz, a given vector field, $\boldsymbol{F}$, can be decomposed into a curl-free field and a divergence-free field, namely,

$$\boldsymbol{F} = -\nabla\sigma + \nabla \times A \tag{3.6}$$

The two subfields, in this case, represent the irrotational acoustic field, where $\nabla \times \hat{\boldsymbol{u}} = 0$, and the incompressible vortical field with the condition of $\nabla \times \tilde{\boldsymbol{u}} = 0$ [73]; these remain tied together through their boundary conditions. When applying the irrotational condition to the unsteady continuity and momentum equations, the set of convected acoustic wave equations are recovered, specifically

$$\frac{\partial \hat{p}}{\partial t} + a_0^2 \hat{\boldsymbol{u}} \cdot \nabla \rho_0 + \boldsymbol{u}_0 \cdot \nabla \hat{p} + \hat{p} \nabla \cdot \boldsymbol{u}_0 + a_0^2 \rho_0 \nabla \cdot \hat{\boldsymbol{u}} = 0 \tag{3.7}$$

$$\begin{aligned} &\rho_0 \left[\frac{\partial \hat{\boldsymbol{u}}}{\partial t} + \nabla \left(\boldsymbol{u}_0 \cdot \hat{\boldsymbol{u}} \right) - \hat{\boldsymbol{u}} \times \left(\nabla \times \boldsymbol{u}_0 \right) \right] \\ &\quad + \frac{\hat{p}}{a_0^2} \left[\frac{\partial \boldsymbol{u}_0}{\partial t} + \frac{1}{2} \nabla \left(\boldsymbol{u}_0 \cdot \boldsymbol{u}_0 \right) - \boldsymbol{u}_0 \times \left(\nabla \times \boldsymbol{u}_0 \right) \right] + \nabla \hat{p} = 0 \end{aligned} \tag{3.8}$$

Using the velocity potential, the equations can be rewritten as,

$$\frac{\partial \hat{p}}{\partial t} + a_0^2 \nabla\varphi \cdot \nabla \rho_0 + \boldsymbol{u}_0 \cdot \nabla \hat{p} + \hat{p} \nabla \cdot \boldsymbol{u}_0 + a_0^2 \rho_0 \nabla \cdot \nabla\varphi = 0 \tag{3.9}$$

$$\begin{aligned} &\rho_0 \left[\frac{\partial \nabla\varphi}{\partial t} + \nabla \left(\boldsymbol{u}_0 \cdot \nabla\varphi \right) - \nabla\varphi \times \left(\nabla \times \boldsymbol{u}_0 \right) \right] \\ &\quad + \frac{\hat{p}}{a_0^2} \left[\frac{\partial \boldsymbol{u}_0}{\partial t} + \frac{1}{2} \nabla \left(\boldsymbol{u}_0 \cdot \boldsymbol{u}_0 \right) - \boldsymbol{u}_0 \times \left(\nabla \times \boldsymbol{u}_0 \right) \right] + \nabla \hat{p} = 0 \end{aligned} \tag{3.10}$$

and, when combined together, yield

$$\begin{aligned} &\rho_0 \left[\frac{\partial \nabla\varphi}{\partial t} + \nabla \left(\boldsymbol{u}_0 \cdot \nabla\varphi \right) - \nabla\varphi \times \left(\nabla \times \boldsymbol{u}_0 \right) \right] \\ &\quad + \frac{\hat{p}}{a_0^2} \left[\frac{\partial \boldsymbol{u}_0}{\partial t} + \frac{1}{2} \nabla \left(\boldsymbol{u}_0 \cdot \boldsymbol{u}_0 \right) - \boldsymbol{u}_0 \times \left(\nabla \times \boldsymbol{u}_0 \right) \right] \\ &\quad + \nabla \hat{p} - \frac{\partial \hat{p}}{\partial t} - a_0^2 \nabla\varphi \cdot \nabla \rho_0 - \boldsymbol{u}_0 \cdot \nabla \hat{p} - \hat{p} \nabla \cdot \boldsymbol{u}_0 - a_0^2 \rho_0 \nabla \cdot \nabla\varphi = 0 \end{aligned} \tag{3.11}$$

which may be further reduced to the Convected Wave Equation form,

$$\frac{\partial}{\partial t}\left[\rho_0 a_0^{-2}\left(\dot{\varphi}+\boldsymbol{u}_0\cdot\nabla\varphi\right)\right]+\nabla\left(\rho_0 a_0^{-2}\dot{\varphi}\boldsymbol{u}_0\right)-\nabla\cdot\left(\rho_0\nabla\varphi\right)=0 \tag{3.12}$$

Next, noting the periodic motion of resonant acoustic modes, the phase and frequency relationship is, at this point, often defined through the normal mode assumption, $\varphi = \varphi_0 e^{-i\omega t}$ [24, 55, 70, 90, 92–94], where φ_0 represents the time-independent mode shape. Then, after applying the normal mode, Eq. (3.12) is setup as a quadratic eigenvalue problem [95] that can be easily solved through order-reduction methods. The velocity potential is then recovered, from which the velocity, pressure, density, and temperature may be determined and written as

$$\begin{cases} \hat{\boldsymbol{u}}=\nabla\varphi; \quad \hat{p}=-\rho_0\left(\partial\varphi/\partial t+\boldsymbol{u}_0\cdot\nabla\varphi\right) \quad \hat{\rho}=\hat{p}/a_0^2; \\ \hat{s}=c_pT/T_0-RP/P_0; \quad \hat{T}=\left(\hat{p}-R\hat{\rho}T_0\right)/(R\rho_0) \end{cases} \tag{3.13}$$

The complex mode shapes of the flow variables can be cast in one of two ways. Using a generic variable, q, as an example, the first method [93] entails expressing the variable as

$$\begin{aligned} \hat{q}\left(\boldsymbol{r},t\right)=q(\boldsymbol{r})e^{-i\omega t} &= \left[q_m^r(\boldsymbol{r})+iq_m^i(\boldsymbol{r})\right]e^{-i\omega t} \\ &= \left[q_m^r(\boldsymbol{r})+iq_m^i(\boldsymbol{r})\right]\Big[\cos(\omega t)-i\sin(\omega t)\Big] \end{aligned} \tag{3.14}$$

where the real part is then taken as shown below.

$$\hat{p}\left(\boldsymbol{r},t\right)=q_m^r(\boldsymbol{r})\cos(\omega t)+q_m^i(\boldsymbol{r})\sin(\omega t) \tag{3.15}$$

This approach has the advantage of easily revealing the spatial phase relationship that might arise in situations where irregular geometries and mean flow effects are accounted for computationally in the conservation equations. Furthermore, the calculation of the various stability integrals discussed in Chapter 5 requires these spatial components to be separated as part of the respective integrand formulations.

The second method more easily predicts the relationship between the phase and relative amplitude of the complex mode shapes,

$$\hat{p}\left(\boldsymbol{r},t\right)=R_m\cos\left(t-\beta\right) \tag{3.16}$$

which can be equated to Eq. (3.15) by the phase and amplitude equations below.

$$\begin{cases} R_m=\sqrt{q_m^{r2}+q_m^{i2}} \\ \beta=\tan^{-1}\left(\dfrac{q_m^i}{q_m^r}\right) \end{cases} \tag{3.17}$$

Here, the total wave modulus, or time-independent amplitude, can be recovered in a single parameter. This method also eliminates the need to depict the spatial relationship in more than one plot. Regardless of the method chosen, both produce characteristics about the resonant modes that simple Helmholtz-type solutions fail to capture.

Chapter 4

Vortical Field Formulation

In light of the irrotational character of the acoustic field, a mechanism must exist to provide the flow with the ability to satisfy the no-slip conditions along the physical wall boundaries. This role has been traditionally filled by a vorticity-generating boundary layer [73], whose velocity offsets the acoustic velocity along the physical walls, where the total velocity must vanish. However, when accounting for mean flow effects, the vorticity generated along the walls can be convected throughout the chamber, thus contributing significantly to the overall stability margin of the chamber through flow effects such as vortex shedding [93].

Generally, the vortical field is solved through computational means [69,74,79], given the difficulty of solving the coupled partial differential equations that define the field. While this approach, validated by experiment [75], is generally applicable to a wide range of combustion chamber geometries, some researchers have sought to recover fundamental solutions for various simplified geometries. This approach, as performed by Majdalani [48,50,96], Flandro [63,97], Majdalani and Flandro [51], and others, has been instrumental in illuminating the underlying physical principles that govern the entire vortical field, especially along the physical boundaries in both solid and liquid rocket engines.

As with the acoustic field, the vortical field can be derived from the unsteady conservation relations, as given by Eqs. (2.8)-(2.11). Recalling that Helmholtz decomposition requires that a divergence-free field be a component of the total vector field, the incompressibility condition may be secured, hence resulting in the vortical continuity,

$$\nabla \cdot \tilde{\boldsymbol{u}} = 0 \tag{4.1}$$

and momentum equations,

$$\frac{\partial \tilde{\boldsymbol{u}}}{\partial t} + \nabla\left(\boldsymbol{u}_0 \cdot \tilde{\boldsymbol{u}}\right) - \tilde{\boldsymbol{u}} \times \left(\nabla \times \boldsymbol{u}_0\right) - \boldsymbol{u}_0 \times \left(\nabla \times \tilde{\boldsymbol{u}}\right) + \rho_0^{-1}\nabla\tilde{p}_1 = -\frac{\mu}{\rho_0}\left(\nabla \times \nabla \times \tilde{\boldsymbol{u}}\right) \tag{4.2}$$

These equations are required to close the system notwithstanding vortical entropy and temperature, which are assumed to be negligible as a consequence of the vortical pressure being much smaller than the dominating acoustic pressure [87]. While this formulation works well in many cases, it can sometimes be beneficial to include the vortical density in the calculations to account for high speed flows. At the outset, the equations for continuity and momentum become

$$\frac{D\tilde{\rho}}{Dt} = \frac{\partial\tilde{\rho}}{\partial t} + \tilde{\boldsymbol{u}} \cdot \nabla\rho_0 + \boldsymbol{u}_0 \cdot \nabla\tilde{\rho} + \tilde{\rho}\nabla \cdot \boldsymbol{u}_0 = 0 \tag{4.3}$$

and

$$\begin{aligned} \rho_0 & \left[\frac{\partial \tilde{\boldsymbol{u}}}{\partial t} + \nabla\left(\boldsymbol{u}_0 \cdot \tilde{\boldsymbol{u}}\right) - \tilde{\boldsymbol{u}} \times \left(\nabla \times \boldsymbol{u}_0\right) - \boldsymbol{u}_0 \times \left(\nabla \times \tilde{\boldsymbol{u}}\right)\right] \\ & + \tilde{\rho}\left[\frac{\partial \boldsymbol{u}_0}{\partial t} + \frac{1}{2}\nabla\left(\boldsymbol{u}_0 \cdot \boldsymbol{u}_0\right) - \boldsymbol{u}_0 \times \left(\nabla \times \boldsymbol{u}_0\right)\right] + \nabla\tilde{p} = -\mu\left[\nabla \times \left(\nabla \times \tilde{\boldsymbol{u}}\right)\right] \end{aligned} \tag{4.4}$$

where Eq. (4.3) can be reduced to

$$\frac{\partial\tilde{\rho}}{\partial t} + \boldsymbol{u}_0 \cdot \nabla\tilde{\rho} = 0 \tag{4.5}$$

if the flow is to be treated as incompressible.

In a similar manner to the acoustic field methodology, the normal mode assumption is made, and the coupled vortical equations are then discretized and solved for pressure and velocity. The vortical velocity is of prime importance, as it has to satisfy the no-slip condition at the physical walls, i.e.,

$$\tilde{\boldsymbol{u}}(\boldsymbol{r}_{\text{wall}}, t) = -\hat{\boldsymbol{u}}(\boldsymbol{r}_{\text{wall}}, t) \tag{4.6}$$

Chapter 5

Energy Formulation

5.1 Kirchoff's Law

The final step in the process of analyzing vorticoacoustic stability is to quantify the energy being transferred into and out of the unsteady field through various mechanisms, such as viscosity, heat transfer, and nozzle losses [98]. The groundwork for this process was laid out by Gustav Kirchhoff [99], who found that the unsteady energy contributions from all sources and sinks in a given flow, minus the work done on that flow, could be equated to the time rate of change of the flow's oscillatory energy according to

$$\frac{\partial E}{\partial t} = D - \nabla \cdot W \tag{5.1}$$

As confirmed by Fischbach and Majdalani [61] and Jacob [10], only at the second order expansion of the energy equation can the relationship between the fluctuating field variables be found, as the zeroth and first order expansions both reduce to zero. As a side note, the third order expansion is required to capture the nonlinear effects, though that is not necessary given that the present analysis is focused on linear energy transfer only.

Taking Eq. (5.1) at the second order expansion,

$$\frac{\partial E_2}{\partial t} = D_2 - \nabla \cdot W_2 \tag{5.2}$$

where,

$$E_2 = \frac{p_1^2}{2\rho_0 a_0^2} + \rho_1 \boldsymbol{u}_0 \cdot \boldsymbol{u}_1 + \frac{1}{2}\rho_0 \boldsymbol{u}_1^2 + \frac{\rho_0 T_0 s_1^2}{2c_p} \tag{5.3}$$

$$D_2 = -\rho_0 \boldsymbol{u}_0 \cdot (\boldsymbol{u}_1 \times \boldsymbol{\Omega}_1) - \rho_1 \boldsymbol{u}_1 \cdot (\boldsymbol{u}_0 \times \boldsymbol{\Omega}_0) - \rho_0 T_1 \boldsymbol{u}_0 \cdot \nabla s_1 \\ - \rho_0 s_1 \boldsymbol{u}_1 \cdot \nabla T_0 - \rho_1 s_1 \boldsymbol{u}_0 \cdot \nabla T_0 + m_1 \psi_1 + T_1 Q_1 \tag{5.4}$$

$$W_2 = \boldsymbol{u}_1 p_1 + \rho_0 \boldsymbol{u}_1 (\boldsymbol{u}_0 \cdot \boldsymbol{u}_1) + \frac{\boldsymbol{u}_0 p_1 \rho_1}{\rho_0} + \rho_1 \boldsymbol{u}_0 (\boldsymbol{u}_0 \cdot \boldsymbol{u}_1) \tag{5.5}$$

reveal the full, linear total change of oscillatory energy in the system. As shown in Chapter 3, the field variables can be written as,

$$\begin{aligned} p_1 &= R_m(t) \left(p^r \cos \omega t + p^i \sin \omega t\right) \\ \rho_1 &= R_m(t) \left(\rho^r \cos \omega t + \rho^i \sin \omega t\right) \\ \boldsymbol{u}_1 &= R_m(t) \left(\boldsymbol{u}^r \cos \omega t + \boldsymbol{u}^i \sin \omega t\right) \\ \boldsymbol{\Omega}_1 &= R_m(t) \left(\boldsymbol{\Omega}^r \cos \omega t + \boldsymbol{\Omega}^i \sin \omega t\right) \end{aligned} \tag{5.6}$$

which are then plugged into Eqs. (5.3), (5.4), and (5.5). The next step requires a time average over the period of the long time interval, which removes short time considerations altogether. Together with an integration over the entire system's volume, Eqs. (5.3), (5.4), and (5.5) become the final version of the source and sink term,

$$\iiint_V \langle D_2 \rangle \, dV = R_m^2 \iiint_V \Bigg\{ -\frac{1}{2}\rho_0 \boldsymbol{u}_0 \cdot \left[(\boldsymbol{u}^r \times \boldsymbol{\Omega}^r) + \left(\boldsymbol{u}^i \times \boldsymbol{\Omega}^i\right)\right] \\ - \frac{1}{2}\left[\rho^r \boldsymbol{u}^r + \rho^i \boldsymbol{u}^i\right] \cdot (\boldsymbol{u}_0 \times \boldsymbol{\Omega}_0) \Bigg\} dV \tag{5.7}$$

the work term,

$$\iiint_V \langle \nabla \cdot W_2 \rangle \, dV = R_m^2 \iiint_V \Bigg\{ \nabla \cdot \ \Bigg\{ \left(\frac{1}{2}\boldsymbol{u}^r p^r + \frac{1}{2}\boldsymbol{u}^i p^i\right) \\ + \rho_0 \left[\frac{1}{2}\boldsymbol{u}^r (\boldsymbol{u}_0 \cdot \boldsymbol{u}^r) + \frac{1}{2}\boldsymbol{u}^i \left(\boldsymbol{u}_0 \cdot \boldsymbol{u}^i\right)\right] \\ + \frac{\boldsymbol{u}_0}{\rho_0}\left(\frac{1}{2}p^r \rho^r + \frac{1}{2}p^i \rho^i\right) + \boldsymbol{u}_0 \left[\boldsymbol{u}_0 \cdot \left(\frac{1}{2}\rho^r \boldsymbol{u}^r + \frac{1}{2}\rho^i \boldsymbol{u}^i\right)\right] \Bigg\} \Bigg\} dV \tag{5.8}$$

and the unsteady energy transfer term,

$$\begin{aligned}\iiint\limits_V \left\langle \frac{dE_2}{dt} \right\rangle dV = \iiint\limits_V \Bigg\{ \frac{1}{2} \Bigg[\frac{1}{2\rho_0 a_0^2} \left(p^{r2} + p^{i2} \right) + \frac{\rho_0 T_0}{2c_p} \left(s^{r2} + s^{i2} \right) \\ + \boldsymbol{u}_0 \cdot \left[\rho^r \boldsymbol{u}^r + \rho^i \boldsymbol{u}^i \right] + \frac{\rho_0}{2} \left(\boldsymbol{u}^{r2} + \boldsymbol{u}^{i2} \right) \Bigg] \Bigg\} dV R_m \frac{\partial R_m^2}{\partial t}\end{aligned} \tag{5.9}$$

where,

$$\begin{aligned}E_m^2 = \iiint\limits_V \Bigg\{ \frac{1}{2} \Bigg[\frac{1}{2\rho_0 a_0^2} \left(p^{r2} + p^{i2} \right) + \frac{\rho_0 T_0}{2c_p} \left(s^{r2} + s^{i2} \right) \\ + \boldsymbol{u}_0 \cdot \left[\rho^r \boldsymbol{u}^r + \rho^i \boldsymbol{u}^i \right] + \frac{\rho_0}{2} \left(\boldsymbol{u}^{r2} + \boldsymbol{u}^{i2} \right) \Bigg] \Bigg\} dV\end{aligned} \tag{5.10}$$

is the energy density of the system of mode m. It should be noted that although the amplitude term R_m appears in the previous equations, it does not represent the physical, limit cycle amplitude, as it does not take into account the nonlinear terms of the third order energy equation expansion, and thus, should be ignored in drawing physical conclusions about the unsteady field [86, 100].

5.2 Linear Growth Rate Equation

The growth of energy in the unsteady field is of primary concern in a linear stability analysis. The present approach to analyzing the energy transfer rate into the each of the modes has been well established in previous works [101, 102] and recently utilized in time-accurate CFD computations [93]. To begin, the exponential growth of each mode's wave amplitude can be seen by take the time average over one period of the expanded form of Eq. (5.2), integrating over the computational domain, and recast in the following form,

$$\frac{\partial R_m}{\partial t} = \alpha'_m R_m; \qquad R_m(t) = e^{\alpha'_m t} \tag{5.11}$$

where $R_m(t)$ defines the amplitude of mode m. As discussed in Subsection 2.2, the present stability analysis does not include the nonlinear growth effects that would lead the resonant waves to a limit cycle amplitude, nor does it highlight the energy cascade into the higher harmonics that would be expected in a physical scenario [10,103,104]. Instead, Eq. (5.11) implies that the wave amplitude can grow exponentially without bound. However, since the present linear stability analysis focuses only on the α'_m term, the unphysical amplitude R_m is rendered irrelevant.

From Eq. (5.11), the linear growth rate term, α'_m, can be seen. This term controls how quickly the wave amplitude grows and is of prime importance in a linear stability analysis, since it also facilitates the transfer of energy between the mean flow and the unsteady field. To generalize this growth rate term, it is normalized by the respective modal energy density using

$$\alpha_m = \frac{\alpha'_m}{2E_m^2} \tag{5.12}$$

where α_m is the normalized rate of energy transfer for mode m, and α'_m is defined as the combined terms from Eqs. (5.4) and (5.5),

$$\begin{aligned}\alpha'_m = \iiint\limits_V \Bigg\langle & -\nabla\cdot\left[\boldsymbol{u}_m p_m + \frac{\boldsymbol{u}_0}{\rho_0} p_m \rho_m + \rho_0 \boldsymbol{u}_m \left(\boldsymbol{u}_0 \cdot \boldsymbol{u}_m\right) + \rho_m \boldsymbol{u}_0 \left(\boldsymbol{u}_0 \cdot \boldsymbol{u}_m\right)\right] \\ & - \rho_0 T_m \boldsymbol{u}_0 \cdot \nabla s_m - \rho_0 s_m \boldsymbol{u}_m \cdot \nabla T_0 - \rho_m s_m \boldsymbol{u}_0 \cdot \nabla T_0 \\ & + m_m \psi_m + T_m Q_m - \rho_0 \boldsymbol{u}_0 \cdot \left(\boldsymbol{u}_m \times \boldsymbol{\Omega}_m\right) - \rho_m \boldsymbol{u}_m \cdot \left(\boldsymbol{u}_0 \times \boldsymbol{\Omega}_0\right) \Bigg\rangle dV\end{aligned} \tag{5.13}$$

5.3 Energy Transfer Mechanisms

All energy sources and sinks are represented in the term α_m. The sign of this term signifies either a positive or negative transfer of unsteady energy. Physically speaking, nonlinear effects would eventually limit the wave amplitude growth when α_m is positive, though here, the acoustic field can only be assumed to have some temporal instability. In a similar manner, a negative value of α_m will lead to the decay of the wave amplitude, thus ensuring system stability. Though the linear analysis approach removes the ability to recover the true amplitude, quantifying linear energy transfer in this way allows specific flow phenomena to be connected to the driving and damping mechanisms of the unsteady field, allowing for the identification of the influence of geometric features on the mean flow and ultimately the emergence of acoustic waves that lead to instabilities.

To begin, the first two mechanisms to be explored are spawned from vorticity-induced contributions that emerge from Eq. (5.7). They are commonly referred to as flow turning and vortex shedding.

5.3.1 Flow Turning

Flow turning is defined in terms of the steady flow vorticity, namely,

$$\alpha_{\text{Flow Turning}} = \frac{1}{2E_m^2} \iiint\limits_V \langle -\rho_m \boldsymbol{u}_m \cdot (\boldsymbol{u}_0 \times \boldsymbol{\Omega}_0) \rangle \mathrm{d}V \tag{5.14}$$

where the angled brackets denote the fact that the integrand is time averaged over one period of oscillation. The well-known Lamb vector, $\boldsymbol{u} \times \boldsymbol{\Omega}$, appears here. It is most commonly associated with vortex generation, turbulence, sound generation, and general rotational flows [105]. Though there is much debate concerning the role of flow turning as a contributor to unsteady energy transfer [97], previous studies have shown that, overall, flow turning tends to allow minimal energy transfer between the steady and unsteady fields which increases with the steady flow vorticity magnitude, assuming non-Beltramian flow [106]. In terms of whether flow turning drives or damps the unsteady field, it is a worthwhile note that though former studies have typically assumed flow turning to be a damping mechanism [63, 97, 107], work by Flandro and Majdalani [107], Flandro, Fischbach, and Majdalani [103], Batterson [87], and Jacob and Batterson [93] have reported instances where flow turning acts to drive the unsteady field, albeit with a relatively negligible contribution.

5.3.2 Vortex Shedding

Vortex shedding is defined in terms of the unsteady flow vorticity, which is the result of mean flow shear layer and acoustic mode interaction, as shown below.

$$\alpha_{\text{Vortex Shedding}} = \frac{1}{2E_m^2} \iiint\limits_V \langle -\rho_0 \boldsymbol{u}_0 \cdot (\boldsymbol{u}_m \times \boldsymbol{\Omega}_m) \rangle \mathrm{d}V \tag{5.15}$$

Due to the fact that the unsteady vorticity typically dominates steady vorticity [108], vortex shedding tends to have significant contributions to the unsteady energy transfer. As shown in the foundational work of Lighthill's acoustic analogy and eighth power law [109, 110], it is understood that a higher injection velocity, and thus a stronger mean flow shear layer, will produce a louder acoustic radiation field. This observation is commonly seen in musical instruments where resonating waves are generated strictly as the result of vorticity [111]. Besides, although the trend of energy growth is typically assumed, it is possible in some instances for vortex shedding to act as a damping mechanism when the steady velocity and unsteady Lamb vector correlate positively, thus leading to a net negative value upon integration.

5.3.3 Surface Work

Surface work is defined as the unsteady energy transfer into or out of the system, which can be computed over the complete system volume by evaluating the divergence of all pertinent variables,

$$\begin{aligned}\alpha_{\text{Surface Work}} = \frac{1}{2E_m^2} \iiint\limits_V \Big\langle & - \nabla \cdot \Big[\boldsymbol{u}_m p_m + \frac{\boldsymbol{u}_0}{\rho_0} p_m \rho_m \\ & + \rho_0 \boldsymbol{u}_m \left(\boldsymbol{u}_0 \cdot \boldsymbol{u}_m \right) + \rho_m \boldsymbol{u}_0 \left(\boldsymbol{u}_0 \cdot \boldsymbol{u}_m \right) \Big] \Big\rangle \mathrm{d}V \end{aligned} \tag{5.16}$$

or by analyzing the surface flux normal to the domain boundary, as outlined by the divergence theorem,

$$\begin{aligned}\alpha_{\text{Surface Work}} = \frac{1}{2E_m^2} \iint\limits_S \bigg\langle - \boldsymbol{n} \cdot \bigg[& \boldsymbol{u}_m p_m + \frac{\boldsymbol{u}_0}{\rho_0} p_m \rho_m \\ & + \rho_0 \boldsymbol{u}_m \left(\boldsymbol{u}_0 \cdot \boldsymbol{u}_m \right) + \rho_m \boldsymbol{u}_0 \left(\boldsymbol{u}_0 \cdot \boldsymbol{u}_m \right) \bigg] \bigg\rangle \mathrm{d}S \end{aligned} \tag{5.17}$$

Leveraging the divergence theorem can be beneficial when considering transport effects in the flow. One such effect is known as injection or pressure coupling, which deals with the mass injection rate into the domain and its synchronization with the resonant acoustic wave. A second transport effect is that of nozzle damping, which accounts for energy being convected out of the system. Here, unsteady energy leaves the domain at the outflow boundary either due to partial acoustic wave reflection or mean flow convection. As would be expected, there is a positive correlation between the injection velocity and the energy loss at the exit boundary, generally due to the increased expulsion rate of the vorticity wave.

5.3.4 Viscous Effects

Here, the unsteady energy transfer is related to steady and unsteady velocity diffusion and dilatation of the flow field, with vorticity strength being the largest factor in determining the importance of the stability term,

$$\alpha_{\text{Viscous}} = \frac{1}{2E_m^2} \iiint\limits_V \langle \boldsymbol{m}_m \boldsymbol{\psi}_m \rangle \mathrm{d}V \tag{5.18}$$

where viscous effects are defined in terms of the unsteady momentum, m_m,

$$\boldsymbol{m}_m = \rho_0 \boldsymbol{u}_m + \rho_m \boldsymbol{u}_0 \tag{5.19}$$

and viscous stress vectors, $\boldsymbol{\psi_m}$,

$$\begin{aligned}\boldsymbol{\psi_m} &= \frac{1}{\rho_0}\left[-\mu\nabla\times(\nabla\times\boldsymbol{u}_m)+\left(\zeta+\frac{4}{3}\mu\right)\nabla(\nabla\cdot\boldsymbol{u}_m)\right] \\ &- \frac{\rho_m}{\rho_0^2}\left[-\mu\nabla\times(\nabla\times\boldsymbol{u}_0)+\left(\zeta+\frac{4}{3}\mu\right)\nabla(\nabla\cdot\boldsymbol{u}_0)\right]\end{aligned} \tag{5.20}$$

reveal the interaction of the mean flow velocity and viscous-related energy transfer.

Though as with the other stability terms, intuition would assume viscosity means a net loss of unsteady energy, in some cases [112], viscosity can act as a driver of the unsteady field when the conditions are favorable. A further analysis of Eq. (5.20) shows the diffusion and dilatation terms of the steady and unsteady field. On one side, dilatational terms only affect the acoustic wave, as they are solely concerned with the divergence of velocity due to compressibility. On the other side, the diffusive terms deal with the incompressible, rotational vorticity wave only. Ultimately, the system's vorticity field will decide whether dilatational terms or viscous diffusion dominate this stability term.

5.3.5 Entropy Generation

Heat-related effects, coming from the term $\langle T_1 Q_1\rangle$ in Eq. (5.13), are generally important to consider for reacting flow stability analyses. When expanded, the heat-related terms, where ϕ is the dissipation function, can be written as the following equation.

$$\langle T_1 Q_1\rangle = \left\langle \frac{T_1\mathcal{H}_1}{T_0} - \frac{\mathcal{H}_0 T_1^2}{T_0^2} + \kappa\left(\frac{T_1\nabla^2 T_1}{T_0} - \frac{\nabla^2 T_0 T_1^2}{T_0^2}\right) + \frac{T_1\phi_1}{T_0} - \frac{\phi_0 T_1^2}{T_0^2}\right\rangle \tag{5.21}$$

From Eq. (5.21), a few additional stability terms are determined, the first of which to be discussed is entropy generation,

$$\alpha_{\text{Entropy}} = \frac{1}{2E_m^2}\iiint\limits_V \langle -\rho_0 T_1\boldsymbol{u}_0\cdot\nabla s_1 - \rho_0 s_1\boldsymbol{u}_1\cdot\nabla T_0 - \rho_1 s_1\boldsymbol{u}_0\cdot\nabla T_0\rangle dV \tag{5.22}$$

Entropy generation plays an important role in the stability considerations of many types of reacting or even cold, compressible flows. It should be noted that, in non-reacting, incompressible flows where resonant acoustic modes are prevalent, entropy is often assumed to be negligible. Generally speaking, however, this should be avoided for reacting or compressible flows. In those cases, entropy generation can occur via combustion [80] and fluid friction, where mean flow compressibility can contribute to unsteady entropy generation at acoustic resonance [54]. Another consideration vorticity generation can lead to is entropy production for non-acoustic, hydrodynamic modes.

5.3.6 Heat Transfer

Heat transfer is closely tied to the unsteady temperature gradient, which physically speaking, captures only the heat diffusion throughout the system, not the phase relationships between heat release and temperature,

$$\alpha_{\text{Heat Transfer}} = \frac{1}{2E_m^2} \iiint\limits_V \left\langle \kappa \left(\frac{T_1 \nabla^2 T_1}{T_0} - \frac{\nabla^2 T_0 T_1^2}{T_0^2} \right) \right\rangle dV \tag{5.23}$$

As a side note, the conduction coefficient κ is treated as a constant, though there is some debate as to that assumption's validity for reacting flows [93].

5.3.7 Heat Release

Within the heat release stability term, the phase relationship between heat release and temperature are captured,

$$\alpha_{\text{Heat Release}} = \frac{1}{2E_m^2} \iiint\limits_V \left\langle \frac{T_1 \mathcal{H}_1}{T_0} - \frac{\mathcal{H}_0 T_1^2}{T_0^2} \right\rangle dV \tag{5.24}$$

This relationship, dependent on combustion chemistry and mean flow properties, is vital to determining how the unsteady energy transfer mechanism either damps or drives the system.

Maximal driving due to T_1 is achieved when T_1 and H_1 are in phase with each other. On the other end of the spectrum, if they are completely out of phase, T_1 will result in maximal damping. Lastly, at 90 degrees out of phase, the contribution of T_1 is effectively neutralized.

5.3.8 Dissipation

The effect of unsteady heat generation due to fluid friction is accounted for in the dissipation stability term.

$$\alpha_{\text{Dissipation}} = \frac{1}{2E_m^2} \iiint\limits_V \left\langle \frac{T_1 \phi_1}{T_0} - \frac{\phi_0 T_1^2}{T_0^2} \right\rangle dV \tag{5.25}$$

Though similar in form to Eq. (5.24), the dissipation functions deal only with the velocity of the flow field, not the combustion process.

Chapter 6

Computational Methodology

Though insightful to the underlying physics of the vorticoacoustic field in simplified mean flows and geometries, closed-form solutions are effectively unobtainable for most real systems. While problematic from a mathematical standpoint, the vorticoacoustic field formulation is itself broadly suited to any type of geometry and mean flow. As we extend former vorticoacoustic analyses to real systems with arbitrary geometry, a computational approach will be developed here.

6.1 Finite Difference Method

A simple, yet effective numerical technique known as the "finite difference method" uses the change in function value and distance between adjacent grid points to approximate derivatives at those grid points. This technique dates back to 1928, when it was originally developed as a way to tackle various physics problems, particularly the wave equation, as well as a discretized application of Dirichlet's principle [113]. However, it was not until the 1950s and the dawn of the computer age that the finite differencing method entered the realm of practicality for engineering applications. Work performed by Clough [114], Turner et al. [115], and many others cemented the importance of the finite difference method, as the aerospace and civil engineering industries in particular quickly found the technique useful for problems in fields such as aeroelasticity and structural dynamics [115].

6.2 Lagrange Interpolation

Before expounding upon the finite differencing method, it is first necessary to understand interpolation, which is the process of choosing some type of continuous function that can be curve-fitted to pass through a set of given points x_i, $i = 0, 1, 2, ...N$. Throughout history, many different forms of the continuous function, called the interpolant, have been proposed. These include formulations like the Newton, Lagrange, or Bernstein polynomials, each having its own strengths and weaknesses. Regardless of which polynomial interpolant is selected, the unisolvence theorem allows for only one unique minimal order polynomial solution that will interpolate through the desired data points. For this study, the Lagrangian form of the interpolation polynomial will be selected to derive the finite differencing equations.

The history of Lagrangian interpolation effectively began in 1779, when the English mathematician Edward Waring [116] took Isaac Newton's general interpolation formula,

$$\begin{aligned} f\left(x\right) &= f\left(x_0\right) + \left(x - x_0\right) f\left(x_0, x_1\right) \\ &\quad + \left(x - x_0\right)\left(x - x_1\right) f\left(x_0, x_1, x_2\right) \\ &\quad + \left(x - x_0\right)\left(x - x_1\right)\left(x - x_2\right) f\left(x_0, x_1, x_2, x_3\right) + \cdots \end{aligned} \tag{6.1}$$

and rewrote it as

$$\begin{aligned} f\left(x\right) = f\left(x_0\right) &\frac{\left(x - x_1\right)\left(x - x_2\right)\left(x - x_3\right)\cdots}{\left(x_0 - x_1\right)\left(x_0 - x_2\right)\left(x_0 - x_3\right)\cdots} \\ + f\left(x_1\right) &\frac{\left(x - x_0\right)\left(x - x_2\right)\left(x - x_3\right)\cdots}{\left(x_1 - x_0\right)\left(x_1 - x_2\right)\left(x_1 - x_3\right)\cdots} \\ + f\left(x_2\right) &\frac{\left(x - x_0\right)\left(x - x_1\right)\left(x - x_3\right)\cdots}{\left(x_2 - x_0\right)\left(x_2 - x_1\right)\left(x_2 - x_3\right)\cdots} \end{aligned} \tag{6.2}$$

which, unlike Newton's approach, negated the need for divided differences. However, as fate would have it, this interpolation scheme has historically been named for the Italian mathematician and astronomer Joseph-Louis Lagrange, who unknowingly published the same formulation sixteen years after Waring [117].

In its modern, generalized form, the Lagrange interpolation technique can be written as

$$f(x) \approx L(x) = \sum_{i=1}^{N} f(x_i) l_i(x) \tag{6.3}$$

where the Lagrange basis polynomial, $l_i(x)$, is

$$l_i(x) = \prod_{\substack{m=1 \\ m \neq i}}^{N} \frac{x - x_m}{x_i - x_m} = \frac{x - x_1}{x_i - x_1} \cdots \frac{x - x_{i-1}}{x_i - x_{i-1}} \frac{x - x_{i+1}}{x_i - x_{i+1}} \cdots \frac{x - x_N}{x_i - x_N} \tag{6.4}$$

and $f(x_i)$ is the function value at grid point x_i. Thus, some function $f(x)$, and its derivatives, can be approximated by finding the Lagrangian interpolating polynomial $L(x)$ through N discrete grid points x_i, $i = 0, 1, 2, ...N$.

6.3 Grid Spacing

For one-dimensional finite differencing applications, the most straightforward approach to gridding a solution domain is to define structured grid points that are equally spaced apart from their respective adjacent grid points. However, this approach is generally an ill-conditioned setup, especially for polynomial interpolants of high order. As it applies to the Lagrangian case, this can lead to a well-documented problem known as the Runge Phenomenon [118], as shown in Figure 6.1. An effective way to overcome all these issues is to migrate from uniform to irregular spacing using either a Chebyshev, Legendre, or Gaussian discretization scheme, which, tied with the more computationally efficient barycentric modification, brings the Lagrangian formulation into the realm of practical applications [119].

For two-dimensional finite differencing, a few additional considerations emerge. First, a compromise between computational time and grid resolution must be made with equally spaced gridding. This has particular application to fluid dynamics where, for example, computational time may be reduced by coarsely gridding the mean flow region, but at the potential expense of missing certain subgrid boundary layer features. Furthermore, square grids, no matter how spaced, often fail to accurately capture geometric structures of practical interest, since any boundary curvature will result in a jagged grid at those locations. The remedy for this comes through a technique known as curvilinear gridding. This gridding scheme builds off the approach of the rectangular, irregular gridding scheme, except

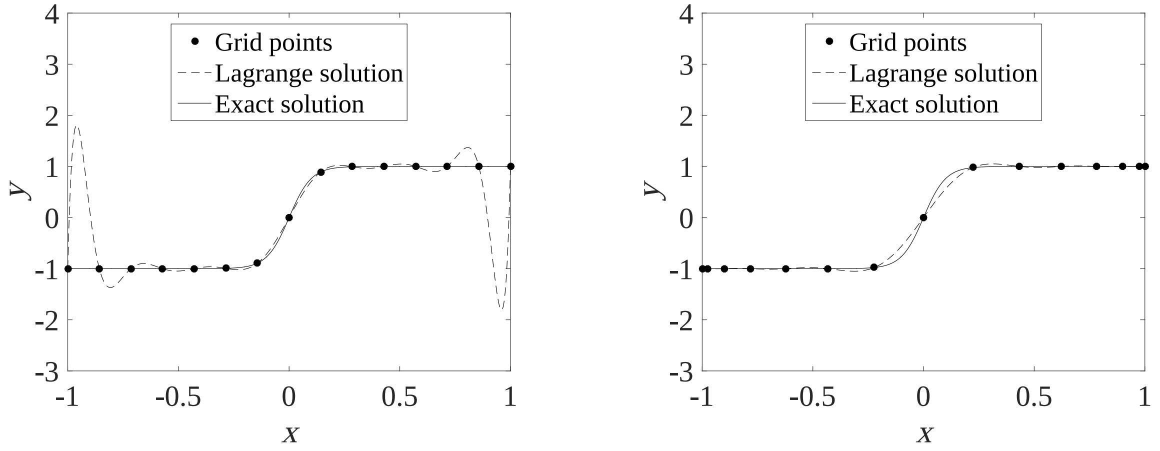

(a) Equally-spaced grid point distribution.

(b) Chebyshev grid point distribution.

Figure 6.1: The Runge phenomenon of Lagrangian interpolation using $y = \tanh{(10x)}$.

in this case, the gridded domain is comprised of quadrilaterals instead of rectangles. For further detail, including the derivation of the first and second derivative approximations, see Appendix B.

6.4 First Derivatives

Sections 6.4 and 6.5 will cover the finite differencing equations used for uniform gridding. However, only the first derivative approximation for regular and irregular central differencing will be derived in its entirety here. For the complete derivations of all pertinent regular, irregular, and curvilinear finite differencing equations, see Appendices A and B.

6.4.1 Central Differencing

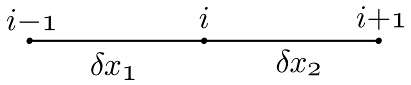

Figure 6.2: First derivative central differencing diagram setup

Starting with the example grid shown in Figure 6.2, the approximation can be found for the derivative at grid point x_i. To achieve this, Eq. (6.3) must be differentiated, which means that actually only Eq. (6.4) is differentiated, since f_i is the function value at grid point x_i, not a function in itself. Central differencing for a grid point x_i requires a three-point Lagrange polynomial to achieve $O\left(\delta x^2\right)$ accuracy. First, the three Lagrange basis polynomials are written as

$$l_{i-1} = \frac{\left(x - x_i\right)\left(x - x_{i+1}\right)}{\left(x_{i-1} - x_i\right)\left(x_{i-1} - x_{i+1}\right)} = \frac{x^2 - x\left(x_{i+1} + x_i\right) + x_i x_{i+1}}{\delta x_1\left(\delta x_2 + \delta x_1\right)} \tag{6.5}$$

$$l_i = \frac{\left(x - x_{i-1}\right)\left(x - x_{i+1}\right)}{\left(x_i - x_{i-1}\right)\left(x_i - x_{i+1}\right)} = \frac{x^2 - x\left(x_{i+1} + x_{i-1}\right) + x_{i+1} x_{i-1}}{\delta x_2 \delta x_1} \tag{6.6}$$

$$l_{i+1} = \frac{\left(x - x_{i-1}\right)\left(x - x_i\right)}{\left(x_{i+1} - x_{i-1}\right)\left(x_{i+1} - x_{i-1}\right)} = \frac{x^2 - x\left(x_i + x_{i-1}\right) + x_i x_{i-1}}{\delta x_2\left(\delta x_2 + \delta x_1\right)} \tag{6.7}$$

where δx_1 and δx_1 are defined as the following.

$$\delta x_1 = x_i - x_{i-1} \tag{6.8}$$

$$\delta x_2 = x_{i+1} - x_i \tag{6.9}$$

Derivatives of the basis polynomials are then taken as the following.

$$l'_{i-1} = \frac{2x - \left(x_{i+1} - x_i\right)}{\delta x_1\left(\delta x_2 + \delta x_1\right)} \tag{6.10}$$

$$l'_i = -\frac{2x - \left(x_{i+1} - x_{i-1}\right)}{\delta x_1 \delta x_2} \tag{6.11}$$

$$l'_{i+1} = \frac{2x - \left(x_i - x_{i-1}\right)}{\delta x_2\left(\delta x_2 + \delta x_1\right)} \tag{6.12}$$

Then, the derivatives of the basis polynomials are evaluated at grid point x_i.

$$a_i = l'_{i-1}\left(x_i\right) = \frac{2x_i - \left(x_{i+1} - x_i\right)}{\delta x_1\left(\delta x_2 + \delta x_1\right)} = -\frac{\delta x_2}{\delta x_1\left(\delta x_2 + \delta x_1\right)} \tag{6.13}$$

$$b_i = l'_i\left(x_i\right) = -\frac{2x_i - \left(x_{i+1} - x_{i-1}\right)}{\delta x_1 \delta x_2} = \frac{\delta x_2 - \delta x_1}{\delta x_1 \delta x_2} \tag{6.14}$$

$$c_i = l'_{i+1}\left(x_i\right) = \frac{2x_i - \left(x_i - x_{i-1}\right)}{\delta x_2\left(\delta x_2 + \delta x_1\right)} = \frac{\delta x_1}{\delta x_2\left(\delta x_2 + \delta x_1\right)} \tag{6.15}$$

Lastly, using Eqs. (6.13), (6.14), and (6.15), the Lagrangian form of the derivative interpolation polynomial is shown to be the following equation

$$\frac{\mathrm{d}f_i}{\mathrm{d}x} \approx L'\left(x_i\right) = a_i f\left(x_{i-1}\right) + b_i f\left(x_i\right) + c_i f\left(x_{i+1}\right) \tag{6.16}$$

where, when $\delta x_1 = \delta x_2$, it can be written in a simplified form for uniform gridding.

$$\frac{\mathrm{d}f_i}{\mathrm{d}x} = \frac{f_{i+1} - f_{i-1}}{x_{i+1} - x_{i-1}} + O\left(\delta x^2\right) \tag{6.17}$$

6.4.2 Forward Differencing

Forward and backward differencing equations are needed primarily for the reason that, at grid boundaries, there is no point on the other side of the boundary point to use in the Lagrangian interpolation polynomial. Furthermore, for application in many types of flows, forward differencing schemes are necessary for numerical stability when accounting for flow convection [120].

To find the derivative at grid point x_i for uniform grid spacing, a straightforward, first order accurate differencing scheme can be written as

$$\frac{\mathrm{d}f_i}{\mathrm{d}x} = \frac{f_{i+1} - f_i}{x_{i+1} - x_i} + O\left(\delta x\right) \tag{6.18}$$

However, using this first order accurate approach in conjunction with a second order accurate scheme will result in a jagged numerical approximation at the connecting grid point. By including an additional grid point in the forward differencing scheme, a second order accurate formulation can be found. For second order accurate, uniform gridding schemes, the Lagrangian polynomial reduces to the following equation.

$$\frac{\mathrm{d}f_i}{\mathrm{d}x} = \frac{-f_{i+2} + 4f_{i+1} - 3f_i}{2\delta x} + O\left(\delta x^2\right) \tag{6.19}$$

6.4.3 Backward Differencing

In a similar manner, the first derivative, backward differencing scheme is developed about grid point x_N, which, for second order accurate, uniform gridding schemes, reduces to

$$\frac{\mathrm{d}f_i}{\mathrm{d}x} = \frac{3f_i - 4f_{i-1} + f_{i-2}}{2\delta x} + O\left(\delta x^2\right) \tag{6.20}$$

and for the simplified first order accurate, uniform gridding case, becomes

$$\frac{\mathrm{d}f_i}{\mathrm{d}x} = \frac{f_i - f_{i-1}}{x_i - x_{i-1}} + O\left(\delta x\right) \tag{6.21}$$

6.5 Second Derivatives

The second derivative finite differencing formulation follows the same path as the first derivatives, with a slight exception. The forward and backward differencing schemes must be taken from a four point Lagrangian polynomial, since only using three points to interpolate reduces the accuracy to first order.

6.5.1 Central Differencing

The central differencing scheme does not suffer from this problem. Thus, taking the derivatives of Eqs. (6.10), (6.11), and (6.12) once more results in

$$a_i = l''_{i-1}\left(x\right) = \frac{2}{\delta x_1\left(\delta x_1 + \delta x_2\right)} \tag{6.22}$$

$$b_i = l''_i\left(x\right) = -\frac{2}{\delta x_1 \delta x_2} \tag{6.23}$$

$$c_i = l''_{i+1}(x) = \frac{2}{\delta x_2 (\delta x_1 + \delta x_2)} \tag{6.24}$$

which concludes in the following Lagrangian polynomial for irregular grid spacing

$$f''(x) \approx a_i f(x_{i-1}) + b_i f(x_i) + c_i f(x_{i+1}) \tag{6.25}$$

and

$$\frac{\mathrm{d}^2 f_i}{\mathrm{d}x^2} \approx \frac{f_{i+1} - 2f_i + f_{i-1}}{dx^2} \tag{6.26}$$

when using uniform grid spacing.

6.5.2 Forward Differencing

The four point Lagrangian polynomial for forward differencing in uniform gridding is written as

$$\frac{\mathrm{d}^2 f_i}{\mathrm{d}x^2} = \frac{-f_{i+3} + 4f_{i+2} - 5f_{i+1} + 2f_i}{\delta x^2} + O\left(\delta x^2\right) \tag{6.27}$$

6.5.3 Backward Differencing

Similarly, the four point Lagrangian polynomial for backward differencing in uniform gridding about grid point x_i is written as

$$\frac{\mathrm{d}^2 f_i}{\mathrm{d}x^2} = \frac{2f_{i+3} - 5f_{i+2} + 4f_{i+1} - f_i}{\delta x^2} + O\left(\delta x^2\right) \tag{6.28}$$

6.6 Computational Example

To give a brief, straightforward example of how the finite differencing process is implemented in actual code, the equation

$$y'(x) + y(x) = 0, \quad y(0) = 5 \tag{6.29}$$

with the exact solution of

$$y(x) = 5e^{-x} \tag{6.30}$$

will be presently solved using the aforementioned numerical techniques. First, several quantities about the grid are defined and described below.

```
n = 6; % Number of gridpoints
BC = 5; % Initial condition
x0 = 0; % Left grid point
xn = 4; % Right grid point
```

The grid itself and the differences between grid points are then defined and calculated.

```
grid = linspace(x0,xn,n);
dx = zeros(1,n-2); % Initialize vector of distances between grid points
dx(1,1) = 0; % Placeholder to make length(dx) = length(grid)
for i = 1:n-1 % Calculates distances between grid points
dx(1,i+1) = grid(i+1) - grid(i);
end
```

Then, the derivative operator $\frac{\mathrm{d}}{\mathrm{d}x}$ is setup in a function file. This second order accurate scheme uses forward differencing for the leftmost grid point, backward differencing for the final grid point, and central differencing for the rest of the grid points.

```
function d_dx = d_dx(n,dx)
% Creates a matrix of zeros for d_dx
d_dx = zeros(n,n);

% Puts in the 1/(2dx) & -1/(2dx) values into the zeros matrix
for i = 1:n-2
d_dx(i+1,i+2) = 1/(2*dx(i+1));
d_dx(i+1,i) = -1/(2*dx(i+1));
end

% Puts in the beginning and end rows
d_dx(1,:) = [-1/dx(2) 1/dx(2) zeros(1,n-2)];
d_dx(n,:) = [zeros(1,n-2) -1/dx(2) 1/dx(2)];
end
```

For this example, the resulting matrix will be of the following form.

$$\frac{d}{dx} = \begin{bmatrix} -\delta x^{-1} & \delta x^{-1} & 0 & 0 & 0 & 0 \\ -2\delta x^{-1} & 0 & 2\delta x^{-1} & 0 & 0 & 0 \\ 0 & -2\delta x^{-1} & 0 & 2\delta x^{-1} & 0 & 0 \\ 0 & 0 & -2\delta x^{-1} & 0 & 2\delta x^{-1} & 0 \\ 0 & 0 & 0 & -2\delta x^{-1} & 0 & 2\delta x^{-1} \\ 0 & 0 & 0 & 0 & -\delta x^{-1} & \delta x^{-1} \end{bmatrix} \tag{6.31}$$

Now that the setup is complete, Eq. (6.29) will now be modified slightly to the following form,

$$\left(\frac{\mathrm{d}}{\mathrm{d}x} + I\right) y = 0 \tag{6.32}$$

such that it can be cast as a system of equations in the familiar matrix form of

$$Ax = b \tag{6.33}$$

Thus, the complete matrix setup will look like

$$\underbrace{\begin{bmatrix} -\delta x^{-1} & \delta x^{-1} & 0 & 0 & 0 & 0 \\ -2\delta x^{-1} & 0 & 2\delta x^{-1} & 0 & 0 & 0 \\ 0 & -2\delta x^{-1} & 0 & 2\delta x^{-1} & 0 & 0 \\ 0 & 0 & -2\delta x^{-1} & 0 & 2\delta x^{-1} & 0 \\ 0 & 0 & 0 & -2\delta x^{-1} & 0 & 2\delta x^{-1} \\ 0 & 0 & 0 & 0 & -\delta x^{-1} & \delta x^{-1} \end{bmatrix}}_{A} \underbrace{\begin{bmatrix} f_1 \\ f_2 \\ f_3 \\ f_4 \\ f_5 \\ f_6 \end{bmatrix}}_{x} = \underbrace{\begin{bmatrix} f'_1 \\ f'_2 \\ f'_3 \\ f'_4 \\ f'_5 \\ f'_6 \end{bmatrix}}_{b} \tag{6.34}$$

where the solution vector x may be deduced through matrix inversion, namely,

$$x = A^{-1}b \tag{6.35}$$

```
I = eye(n); % Create identity matrix
A = d_dx(n,dx) + I; % Create the A matrix
B = zeros(n,1); % Create the B vector

% Apply the boundary condition
B(1,1) = BC; % To the B vector
A(1,:) = I(1,:); % and the A matrix

% Calculate the solution values
X = A\B;
```

The results of the computation are shown in Figure 6.3. Even only using six grid points, the numerical solution matches the exact solution fairly well. Increasing the number of grid points to a much higher number will reduce the numerical error to a negligible quantity. The

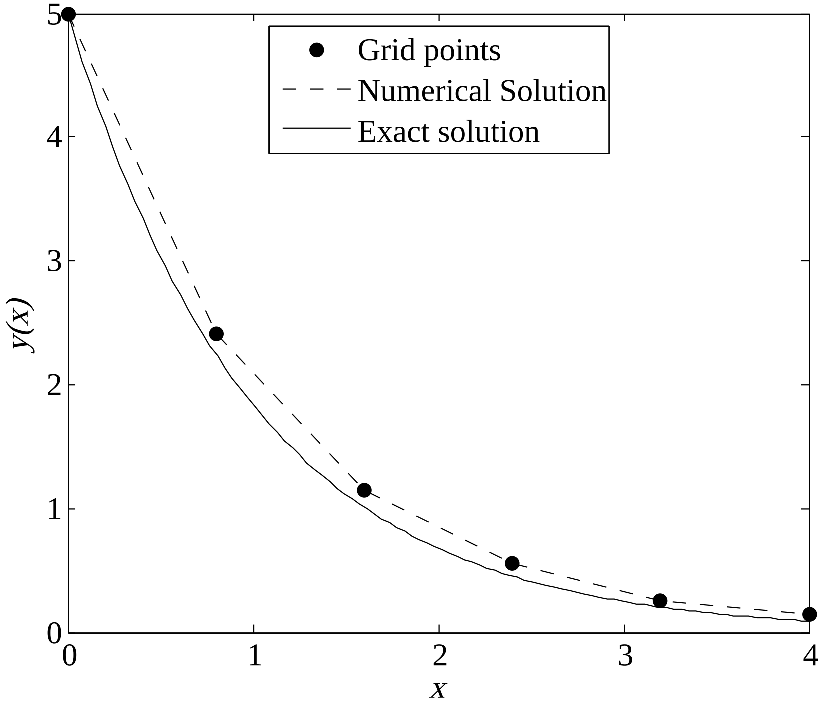

Figure 6.3: Comparison of the numerical versus the exact solution of Eq. (6.29).

same general process shown in this chapter will be used in calculating the acoustic, vortical, and energy fields in the bidirectional vortex engine in Chapter 7.

Chapter 7

Bidirectional Vortex Engine Analysis

7.1 Analysis Process

Before the discussion of the stability analysis of the bidirectional vortex engine can begin, it is important to understand how the overall analysis process operates. This process will be explained in the context of an experimental engine being tested for stability, followed by potential redesign as a result of the stability study. This loop continues until the stability margins have reached a satisfactory level as set by a design engineer.

As shown in Figure 7.1, the iteration process begins with a model developed in a computer-aided design software package. From there, a computational fluid dynamics analysis is performed to determine mean flow properties based on the geometry and inlet conditions of the rocket engine. In this particular study, CFD data is produced from ANSYS Fluent. First, the computational domain is gridded with an 853,339 element hybrid mesh, composed of primarily unstructured blocks, while the middle portion of the chamber is gridded with a structured hexahedral block. The fuel and oxidizer inlets have pure methane and oxygen

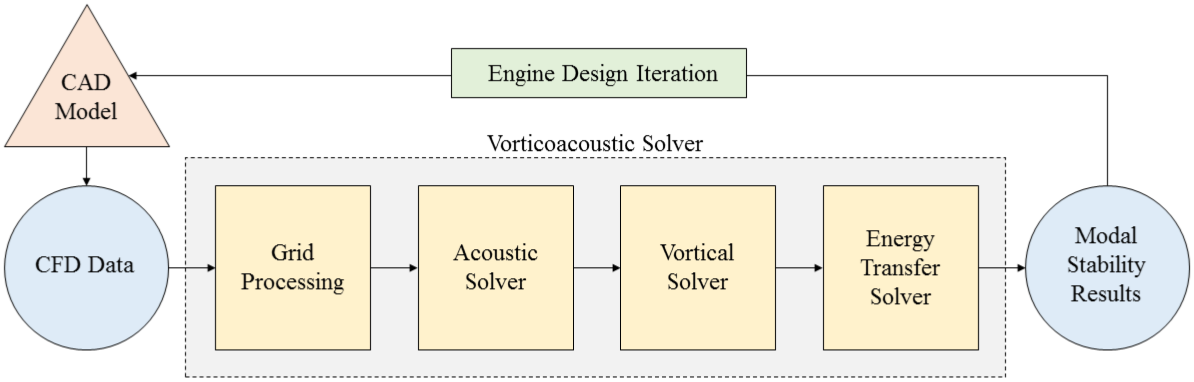

Figure 7.1: Stability analysis flowchart.

flowing at 0.75 kg/s and 2 kg/s, pressure set to 1000 psi and 900 psi, and temperature set to 277.778 K and 127.78 K, respectively. Then, to solve for the mean flow variables, a first order upwind discretization scheme is used for all variables except for pressure, which remains with the standard method of discretization. Furthermore, the density and thermal conductivity values are determined from the ideal gas law and an ideal mixing law. Lastly, using the energy equation, the realizable $k - \epsilon$ turbulence model, and the species transport equations for the methane-air reaction, the mesh is initialized and run to convergence using a pressure-based solver implementing the SIMPLE scheme in ANYSYS Fluent.

From the mean flow results, with sample values listed in Table 7.1, the vorticoacoustic analysis then starts by first taking a center, axisymmetric slice from the hybrid grid and changing it to the structured grid shown in Figure 7.2, by means of a Winslow two-dimensional, implicit, finite difference heat equation solver [121]. The mean flow variables are then interpolated onto the structured grid from the unstructured grid. This structured grid and solution variable set form the basic input for the acoustic and vortical solvers. Next, the focus of the grid processing section moves to determining the boundary grid points and

Name	Sample Value
Streamwise velocity	220 [m/s]
Normal velocity	0.06 [m/s]
Azimuthal velocity	10 [m/s]
Density	2.10 [kg/m^3]
Temperature	2633 [K]
Speed of sound	1082 [m/s]
Specific heat ratio	1.14
Viscosity	$1.72 \cdot 10^{-5}$ [kg/(s $\cdot$ m)]
Specific gas constant	389 [J/kg $\cdot$ K]

Table 7.1: Variables imported from the computational fluid dynamics solver and a sample value (taken at the centerline at $x = 0.085$ m).

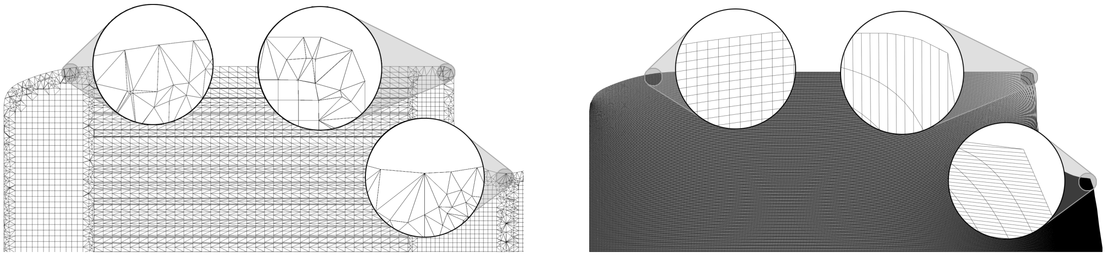

(a) Unstructured grid from CFD.
(b) Structured grid from heat solver.

Figure 7.2: Comparison of the unstructured versus structured grids.

grid spacing, calculating grid normal unit vectors for use in later boundary conditions, and calculating the volume of the entire domain from the axisymmetric slice.

The acoustic solver follows next, by casting the convected acoustic wave equation as a quadratic eigenvalue problem [95]. The eigenvalues of this computational step correspond to the frequencies of the desired modes in the analysis, which then are used in the vortical and energy calculations in the following sections. In a similar manner, the eigenvectors represent the acoustic velocity potential, φ, and the flow variables are calculated as shown in Eq. (3.13). Plotting the results across the domain enables us to visualize the spatial, time-independent mode shape of the flow variables. Usually, those results show that the acoustic field is traditionally driven largely by the chamber geometry. However, including the mean flow effects can drastically change the acoustic frequencies, generally causing them to be lower than the Helmholtz resonator solution for that chamber.

Then, the vortical solver unveils the unsteady vorticity structures in the domain, specifically for the variables of velocity and pressure. The vortical field equations are discretized and set up as a system of equations, with boundary conditions for the velocity along the physical walls made equal to the opposite of the acoustic velocity. It should be noted that, in some cases, an upwinding scheme may be more effective than a typical central differencing scheme when solving the vortical field. Upwinding, which essentially means using a forward differencing scheme across the majority of the computational domain instead of just for a boundary, can be necessary in some cases to avoid a buildup of numerical flux at grid points when considering high-speed flows.

Lastly, the calculation of the stability margins for each mode are handled by the energy transfer solver. The associated flow variables for each of the energy transfer mechanisms are gathered, and integrated over the volume of the chamber. To make the energy transfer results comparable between different modes, the resulting stability margins are then normalized by the energy in that mode. The stability margins from each contribution, such as flow turning or vortex shedding, are finally summed for a given mode. The result is a stability margin for that specific mode that encapsulates all the different pathways that energy can flow into or out of the unsteady field. By plotting the integrands of each pathway's volume integral, a connection can be made between the characteristics of the engine and the physical mechanisms that contribute to combustion instability for that particular design. Alterations are then made by the design engineer to the CAD model of the engine and the entire stability analysis process is repeated. Once the stability margins are within an acceptable range, the design iteration loop is finished and the engine can continue to the next stage of development.

7.2 The Bidirectional Vortex Engine

As a demonstration of the vorticoacoustic stability analysis process, a study of the stability of the bidirectional vortex engine, shown in Figures 7.3 and 7.4, will be performed. A heightened interest in vortex-driven combustion systems can be dated to the World War II era when flow separation efficiency in cyclonic dedusters was sought after [122]. The bidirectional vortex concept also found applications in various industrial combustors, furnaces, and cyclonic separators. This flow setup, as it directly relates to rocketry, provides several enhancements that make it a viable approach to creating futuristic, stable propulsion systems. In contrast to conventional propulsion systems, the bidirectional vortex engine's unique layout allows for a number of features such as increased wall cooling, potentially improved stability margins, and reduced engine weight. Flow characteristics such as the swirl velocity, core vortex thickness, and tangential injection velocity must be accounted for when

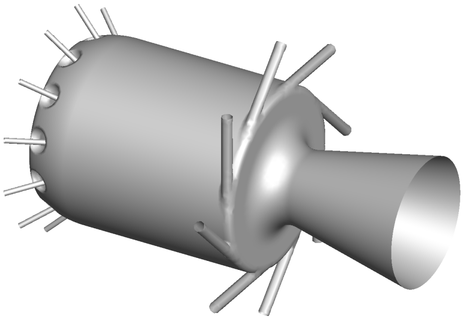

Figure 7.3: The bidirectional vortex engine.

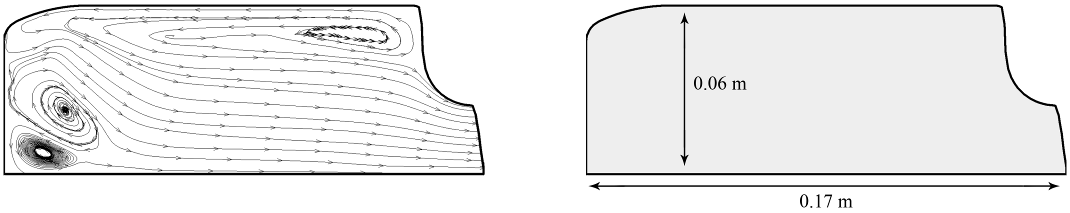

(a) Axisymmetric stream trace plot

(b) Dimensions of the domain

Figure 7.4: Bidirectional vortex engine setup.

considering the departure of the acoustic and vortical fields from traditional Helmholtz and cold flow solutions.

7.3 Mean Flow

For the the engine used in the present analysis, the mean flow was developed in a commercially-available computational fluid dynamics solver for a methane/LOX fuel and oxidizer combination. Important features reveal themselves in the stream trace plot shown in Figure 7.4a, particularly along the headwall region. Here, two large vortex cells emerge, which contribute to modal locking for the acoustic modes, as shown in the next section. A vortex cell immediately adjacent to the oxidizer inlet also acts, in a similar manner, to impede the global motion of the acoustic waves.

However, the primary feature of the bidirectional vortex engine can be most easily seen in Figure 7.5 in the stark gradient of the temperature profile crossing over from the outer, cooler vortex to the hot, reacting inner vortex. This gradient, while important in keeping the

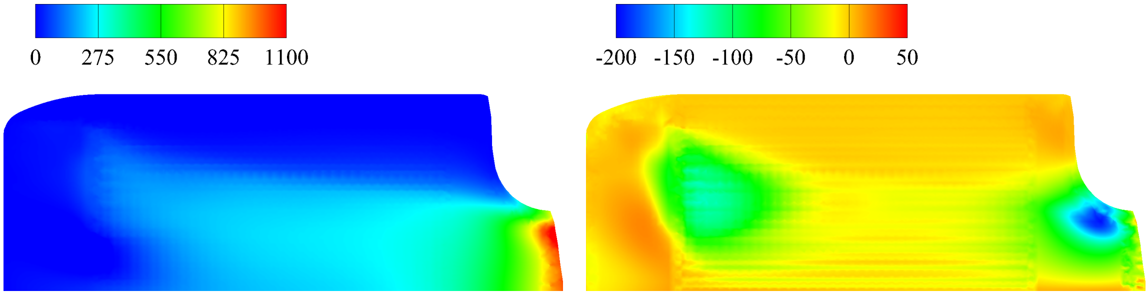

(a) Streamwise velocity [m/s]. (b) Normal velocity [m/s].

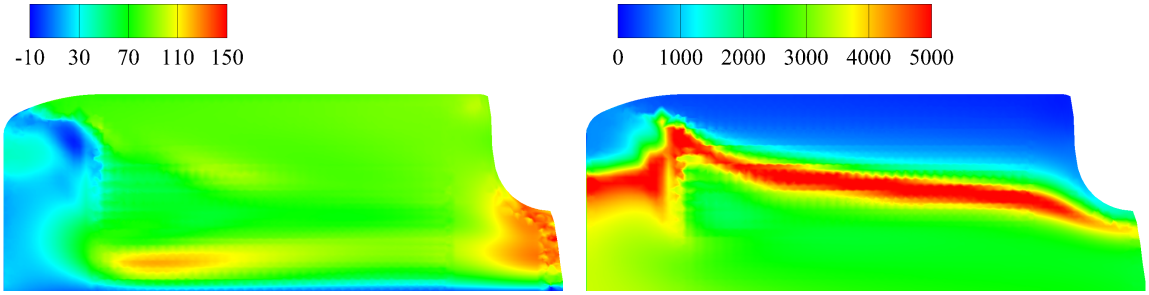

(c) Azimuthal velocity [m/s]. (d) Temperature [K].

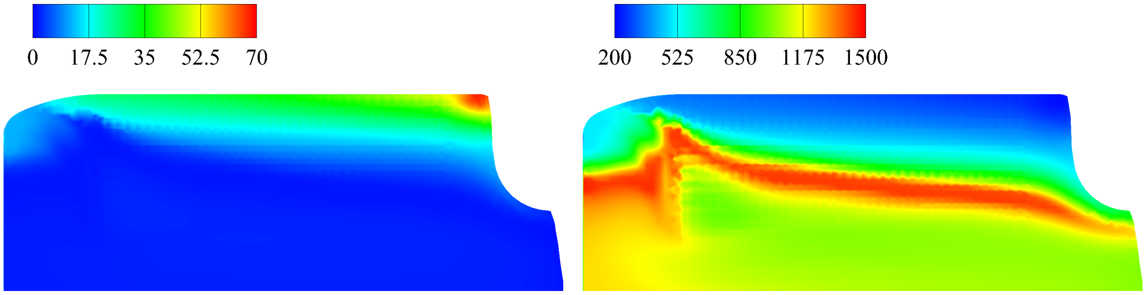

(e) Density [kg/m^3]. (f) Speed of sound [m/s].

Figure 7.5: Combusting flow mean values.

engine walls cool during combustion, also serves as an impediment to acoustic wave motion across the entire domain.

7.4 Acoustic Field

The domain of the chamber's acoustic field, and thus the vortical and energy fields as well, is defined as the region in the engine from the headwall to the sonic line at the throat, since any acoustic waves in the throat will be effectively reflected at that point. However, acoustic modes can be further restricted even within that domain. A distinguishing feature of the bidirectional vortex engine is acoustic mode locking. This phenomena occurs due to the sharp change in temperature across the shear region in the middle of the domain in reacting flow. As expected, however, the cold flow results, as shown in Figure 7.6, do not exhibit this feature as the overall speed of sound is relatively constant. The cold flow solution differs from the Helmholtz solution by including the effects of the mean flow, but not including combustion's significant effects. Here, the acoustic pressure for the first tangential mode of 892 Hz can essentially be confined only by chamber geometry. Due to the roles that the irregular geometry and mean flow play in determining the 1T waveform, the pressure and velocity are not 90 degrees out of phase, as in a Helmholtz solution. Instead, the wave exhibits a type of sloshing behavior that is revealed in the spatial relationship depicted in the phase diagram of Figure 7.6b. However, the cold flow solution bears remarkable similarity to the Helmholtz solution, in that the magnitude is largest toward the sidewall and smallest near the centerline. Though this similarity is present, it should be noted that the Helmholtz resonator frequency for this mode is 1696 Hz, a stark difference from the cold flow solution frequency. This result is due in large part to the influence of the mean flow [54, 112], and more specifically in this case, the restriction of the acoustic flow by the bidirectional vortex structure.

When including the influential effects of combustion, the resulting thermodynamic characteristics of the bidirectional vortex engine prove troublesome in determining which modes

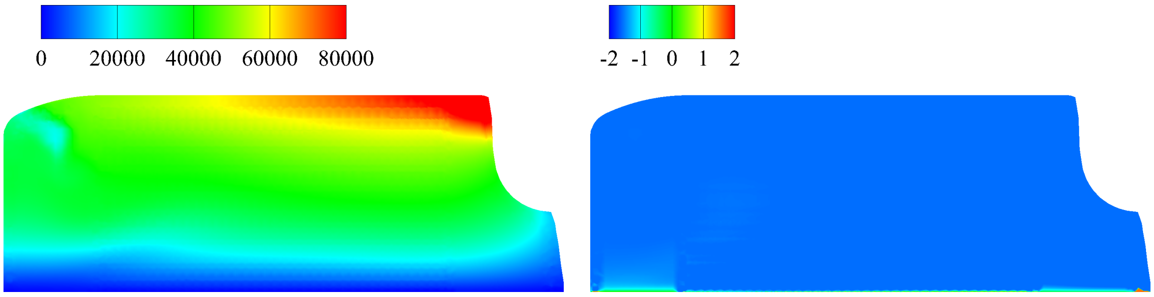

(a) Pressure magnitude [Pa].

(b) Pressure phase [rad].

Figure 7.6: Pressure profile for the 1T mode with non-reacting flow.

Mode	Helmholtz Resonator Frequency [Hz]	Convected Wave Frequency [Hz]	Reacting Frequency [Hz]
1T	1696	892	1243
2T	2786	1404	2445
3T	3816	1824	3581
1L	1156	1092	1321
2L	2205	2164	2532
3L	2880	2514	3645

Table 7.2: Frequencies predicted for the first three pure tangential and longitudinal modes.

are most dominant in the flow. As evidenced when analyzing the mean flow, the speed of sound goes through a drastic change across the shear region. This creates semi-isolated pockets in which acoustic waves oscillate based on the local thermodynamic layout, rather than the overall chamber geometry. Here, the frequencies are generally higher than their cold flow counterpart, largely because of the increased speed of sound, which is directly affected by the higher chamber temperature due to the reacting flow. Table 7.2 outlines the predicted frequencies for the first three pure tangential and longitudinal modes, affirming the general trend of frequency decrease from the Helmholtz solution, then an increase when considering reacting flow.

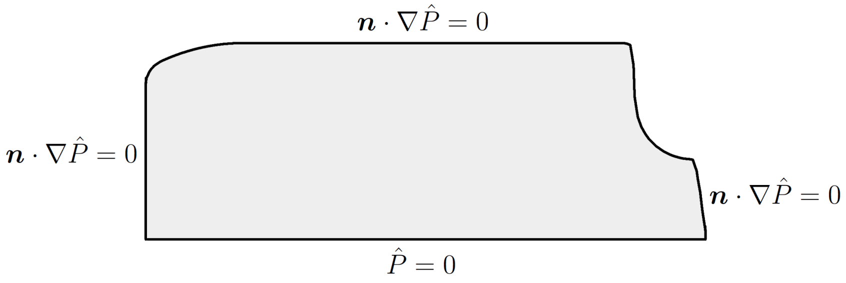

Figure 7.7: Acoustic boundary conditions for the 1T mode.

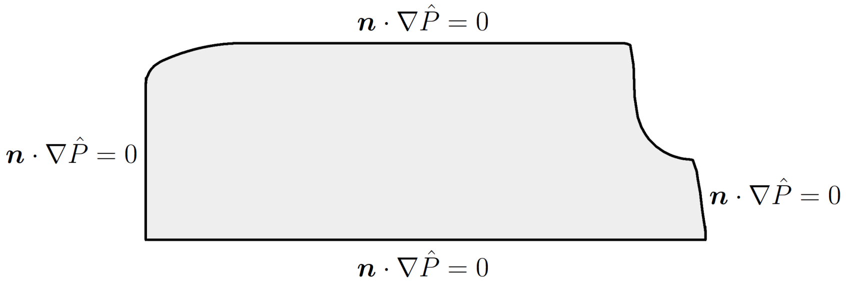

Figure 7.8: Acoustic boundary conditions for the 2-3T and 1-3L modes.

	Head wall	Outer wall	Nozzle	Centerline
1T	$\boldsymbol{n} \cdot \nabla \hat{P} = 0$	$\boldsymbol{n} \cdot \nabla \hat{P} = 0$	$\boldsymbol{n} \cdot \nabla \hat{P} = 0$	$\hat{P} = 0$
2T, 3T, 1-3L	$\boldsymbol{n} \cdot \nabla \hat{P} = 0$	$\boldsymbol{n} \cdot \nabla \hat{P} = 0$	$\boldsymbol{n} \cdot \nabla \hat{P} = 0$	$\boldsymbol{n} \cdot \nabla \hat{P} = 0$

Table 7.3: Acoustic boundary conditions for the bidirectional vortex engine.

In support of the frequencies shown, Figures 7.9-7.12 show the related mode shapes for the 1T and 1L modes, while the higher modes listed can be found in Appendix D, shown specifically in Figures D.1-D.8. The boundary conditions used to solve for these mode shapes are listed in Table 7.3 and shown in Figures 7.7 and 7.8, where $\boldsymbol{n}$ is the unit vector normal to its respective surface. The change in the centerline boundary condition for the 1T mode is due to the Bessel solution being non-zero at the centerline, allowing for cross-flow. Perhaps the most noticeable feature of the acoustic profile in both the 1T and 1L modes is the modal locking in the region immediately surrounding the fuel and oxidizer inlets, visible in Figures 7.9 and 7.10. This is effectively caused by the isolating properties of a strong density and temperature gradient surrounding the inlets, which causes most of the acoustic oscillations to remain in those areas. A parallel can be drawn to a traditional method of oscillation reduction through the use of baffles. Effectively localizing oscillations by placing physical obstacles perpendicular to the flow, baffles seek to prevent global oscillations in the chamber, though some small level of acoustic motion still lingers. Moreover, baffles are usually spaced apart at even intervals, causing trapped oscillations to still occur at similar frequencies.

Nevertheless, there is very little communication between the regions, much like the trapped oscillations noted around the oxidizer and fuel inlets in the bidirectional vortex engine.

A less prominent feature is the sharp dividing line of the shear region in the middle. As expected, this is evident in the acoustic temperature profile visible in Figure 7.12, and thus the density and pressure profiles as well, which all scale together with the speed of sound. This result follows from the observation that the mean flow temperature profile, and to a lesser extent the mean flow density profile, define the acoustic temperature. However, the most prominent variable in the overall acoustic analysis is the pressure, which is sharply divided by the inner shear region between the two main vortices of the flow.

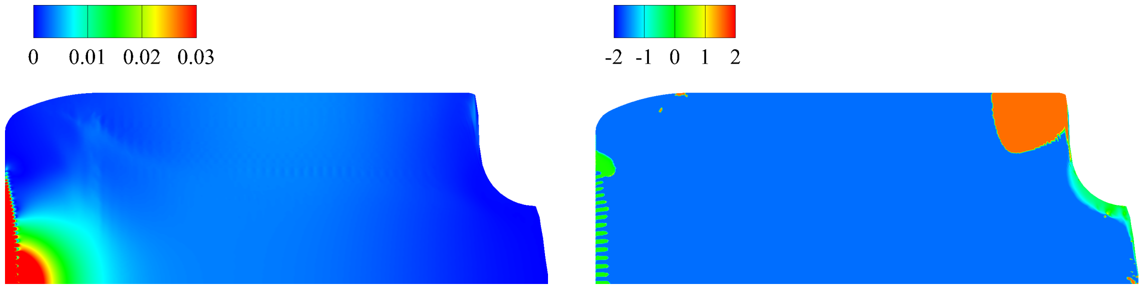

(a) Streamwise velocity magnitude [m/s]. (b) Streamwise velocity phase [rad].

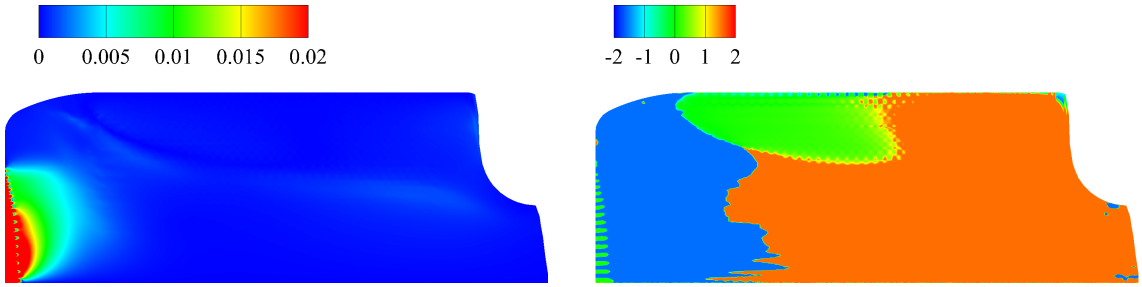

(c) Normal velocity magnitude [m/s]. (d) Normal velocity phase [rad].

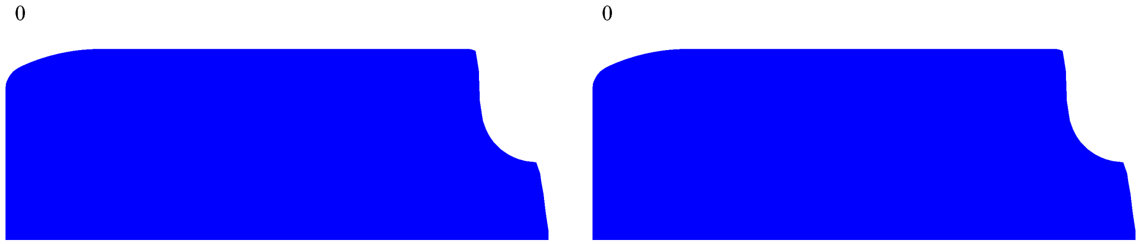

(e) Azimuthal velocity magnitude [m/s]. (f) Azimuthal velocity phase [rad].

Figure 7.9: Acoustic velocities for the 1L mode with reacting flow.

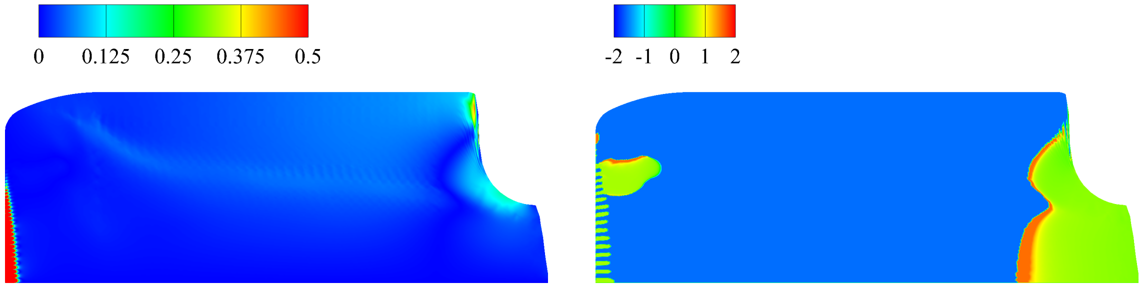

(a) Streamwise velocity magnitude [m/s]. (b) Streamwise velocity phase [rad].

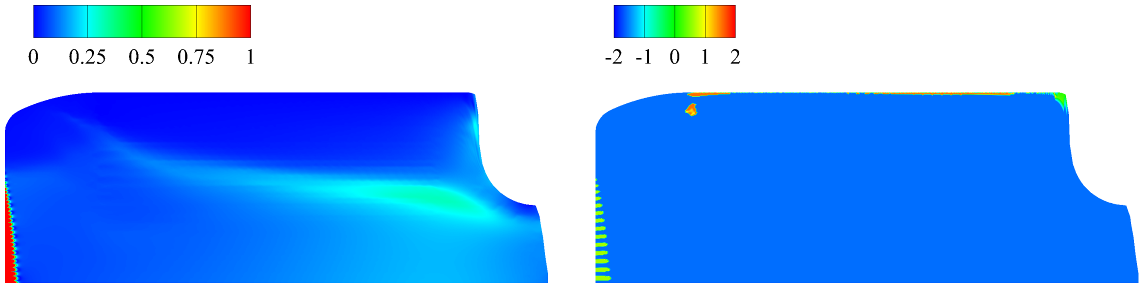

(c) Normal velocity magnitude [m/s]. (d) Normal velocity phase [rad].

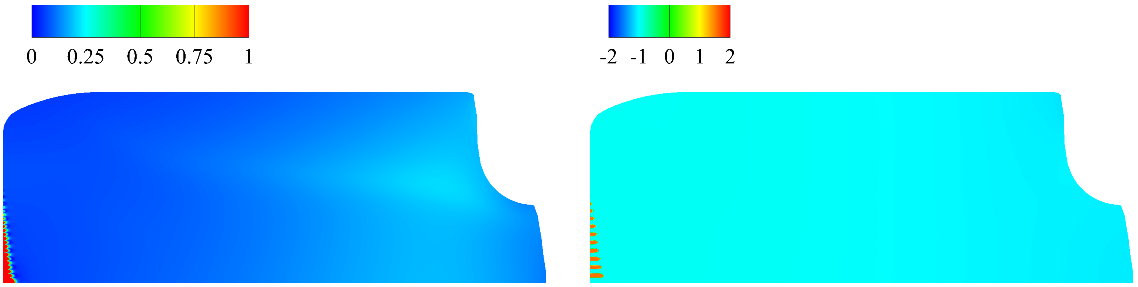

(e) Azimuthal velocity magnitude [m/s]. (f) Azimuthal velocity phase [rad].

Figure 7.10: Acoustic velocities for the 1T mode with reacting flow.

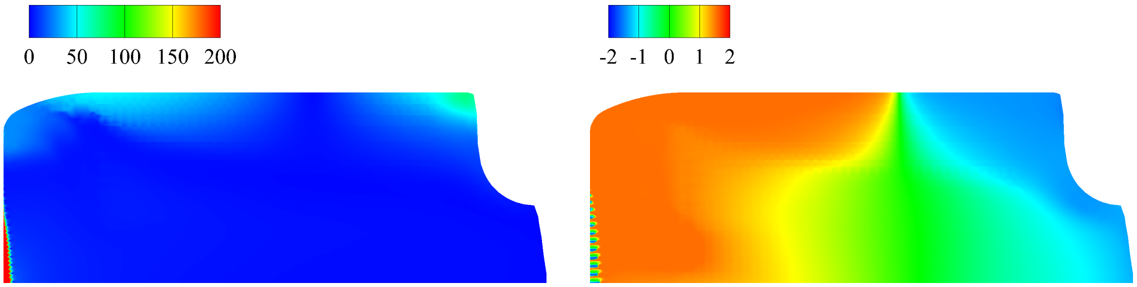

(a) Pressure magnitude [Pa].

(b) Pressure phase [rad].

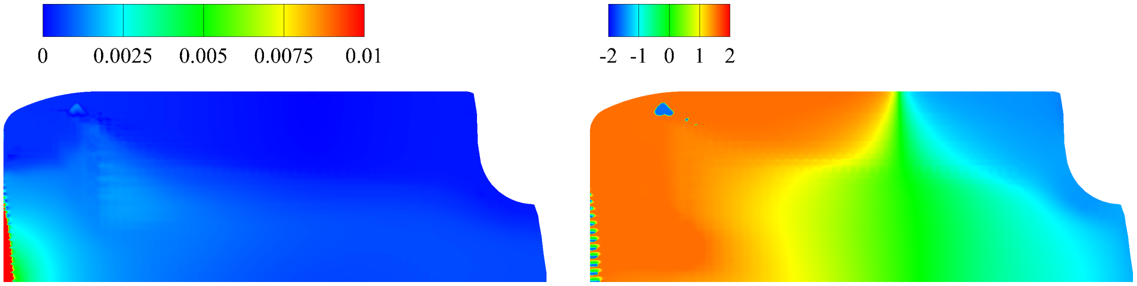

(c) Temperature magnitude [K].

(d) Temperature phase [rad].

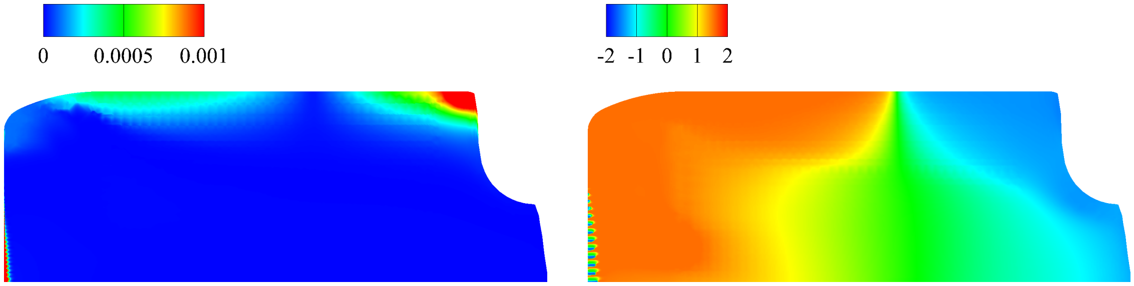

(e) Density magnitude [kg/m^3].

(f) Density phase [rad].

Figure 7.11: Acoustic pressure, density, and temperature profiles for the 1L mode with reacting flow.

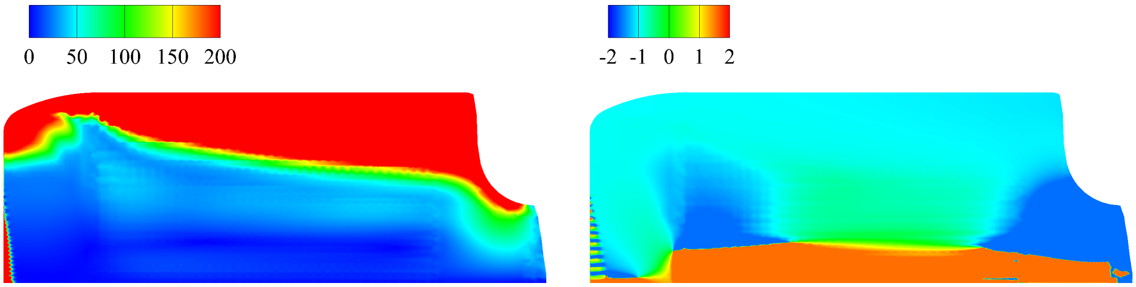

(a) Pressure magnitude [Pa]. (b) Pressure phase [rad].

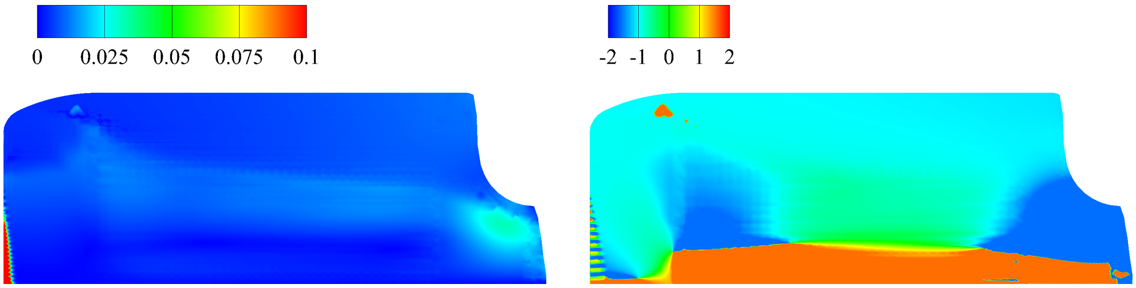

(c) Temperature magnitude [K]. (d) Temperature phase [rad].

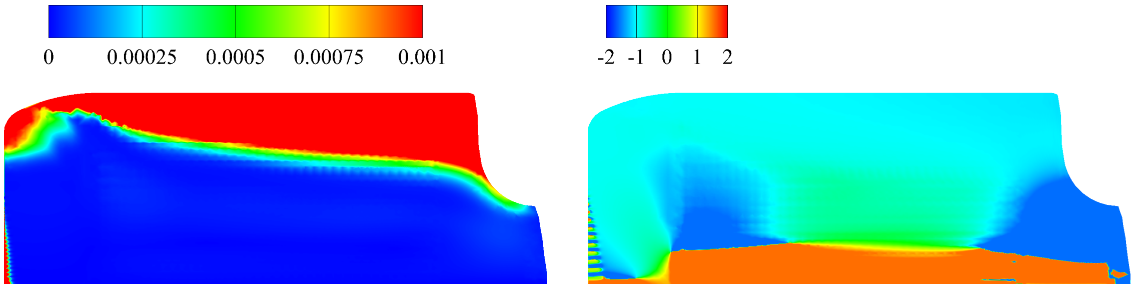

(e) Density magnitude [kg/m^3]. (f) Density phase [rad].

Figure 7.12: Acoustic pressure, density, and temperature profiles for the 1T mode with reacting flow.

7.5 Vortical Field

The second component of a vorticoacoustic analysis is the dissection of the vortical field and its subsequent role in system stability. While vorticity traditionally is assumed to be only a boundary layer correction for the irrotational acoustic flow, some engine designs, such as the one presently considered, cause vorticity to play a key role in stability. Not only does the evident rotational nature of the flow lend itself to generating strong vortical motion along the shear layer between the main vortices, but only by including the mean flow can wall-generated vorticity then be convected into the flow.

	Head wall	Outer wall	Nozzle	Centerline
Pressure	$\boldsymbol{n}\cdot\nabla\tilde{P}=0$	$\boldsymbol{n}\cdot\nabla\tilde{P}=0$	$\boldsymbol{n}\cdot\nabla\tilde{P}=0$	$\boldsymbol{n}\cdot\nabla\tilde{P}=0$
Velocity	$\tilde{\boldsymbol{u}}=-\hat{\boldsymbol{u}}$	$\tilde{\boldsymbol{u}}=-\hat{\boldsymbol{u}}$	$\partial^2\tilde{\boldsymbol{u}}/\partial s^2=0$	$\partial\tilde{\boldsymbol{u}}/\partial y=0$

Table 7.4: Vortical boundary conditions for the bidirectional vortex engine

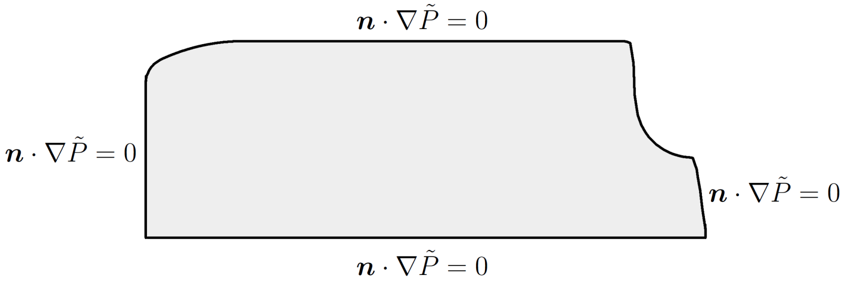

Figure 7.13: Vortical boundary conditions for the continuity equation.

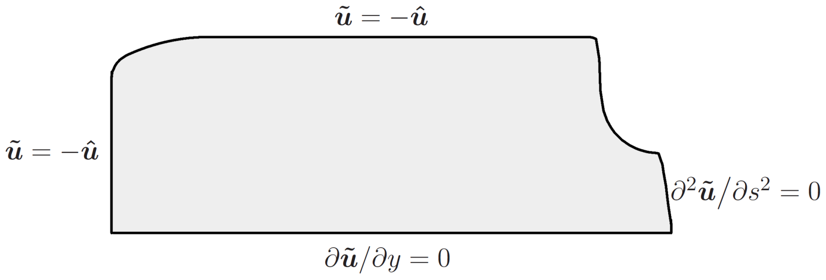

Figure 7.14: Vortical boundary conditions for the momentum equation.

Notwithstanding the complex nature of the vortical field in this engine, as shown by the 1T and 1L vortical velocities in Figures 7.15 and 7.16, and the vortical velocities of the higher modes shown in Appendix D through Figures D.9-D.12, the computational approach shows its strength in capturing vortex cells that would prove to be a fairly difficult task for analytical approaches. Solved using the boundary conditions listed in Table 7.4 and shown in Figures 7.13 and 7.14, both the 1T and 1L modes exhibit vorticity generation in the several smaller vortices near the fuel and oxidizer inlets, creating discrete vortex cells which play a minor role in unsteady energy contributions as will be shown in the following section. However, the general flow for vorticity generation begins with the shear layer, dissipating somewhat as it leaves the chamber and also approaches the centerline. This suggests that secondary vortex formation is driven largely by flow not relegated to the tangential direction.

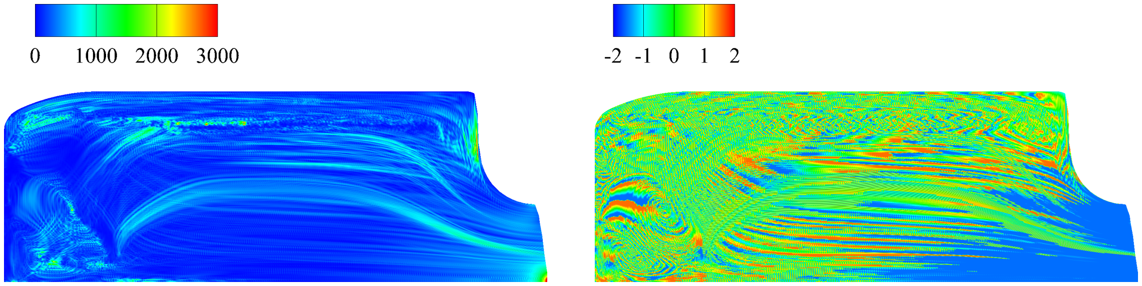

(a) Streamwise velocity magnitude [m/s]. (b) Streamwise velocity phase [rad].

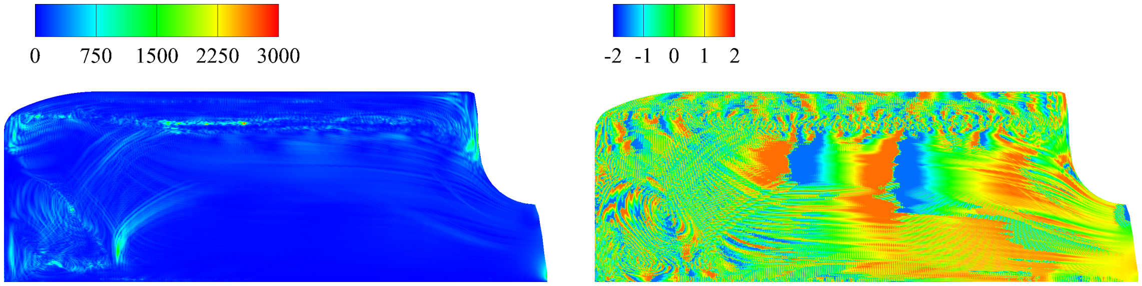

(c) Normal velocity magnitude [m/s]. (d) Normal velocity phase [rad].

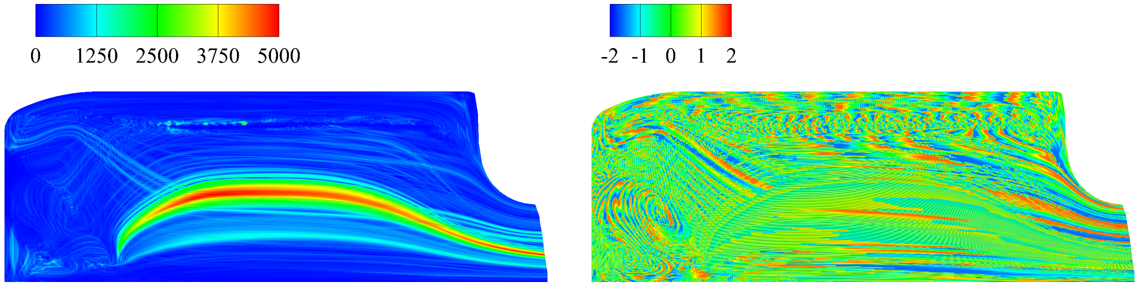

(e) Azimuthal velocity magnitude [m/s]. (f) Azimuthal velocity phase [rad].

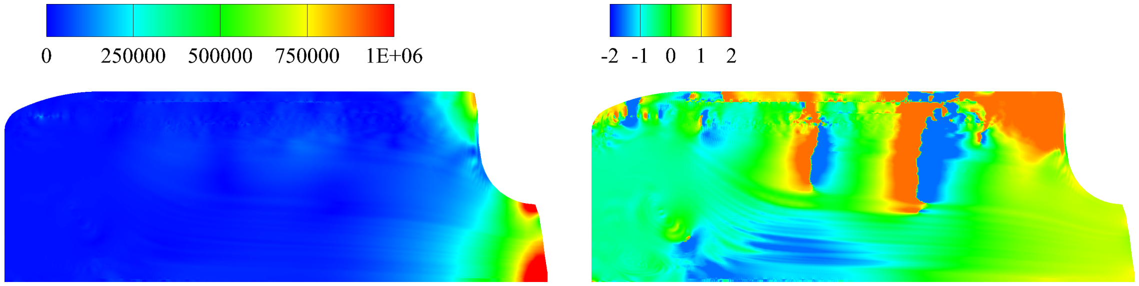

(g) Pressure magnitude [Pa]. (h) Pressure phase [rad].

Figure 7.15: Vortical velocities and pressure for the 1L mode.

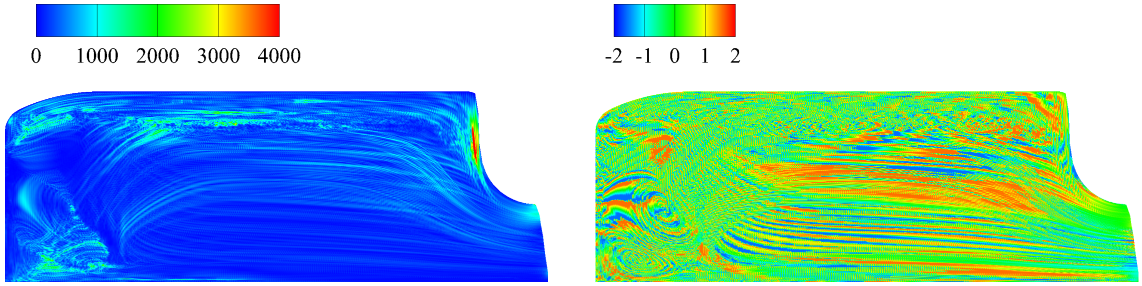

(a) Streamwise velocity magnitude [m/s].

(b) Streamwise velocity phase [rad].

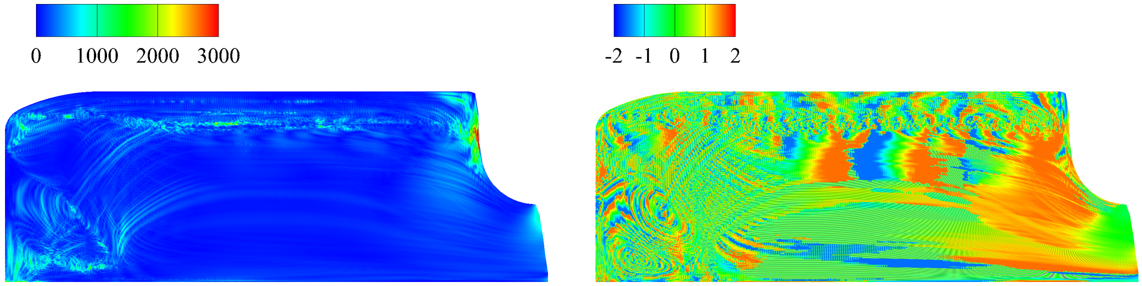

(c) Normal velocity magnitude [m/s].

(d) Normal velocity phase [rad].

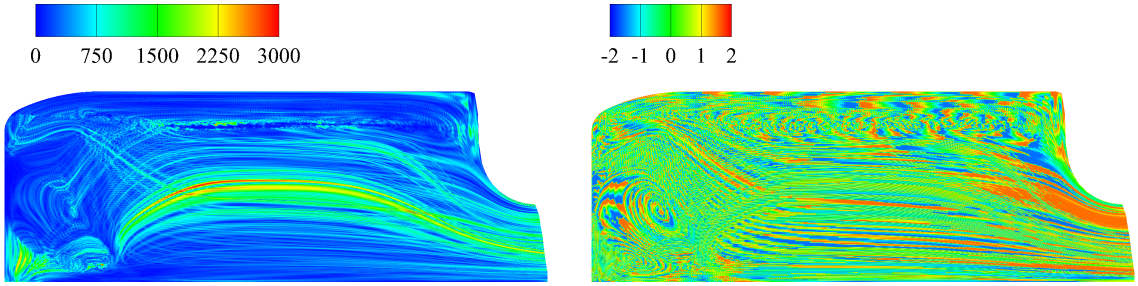

(e) Azimuthal velocity magnitude [m/s].

(f) Azimuthal velocity phase [rad].

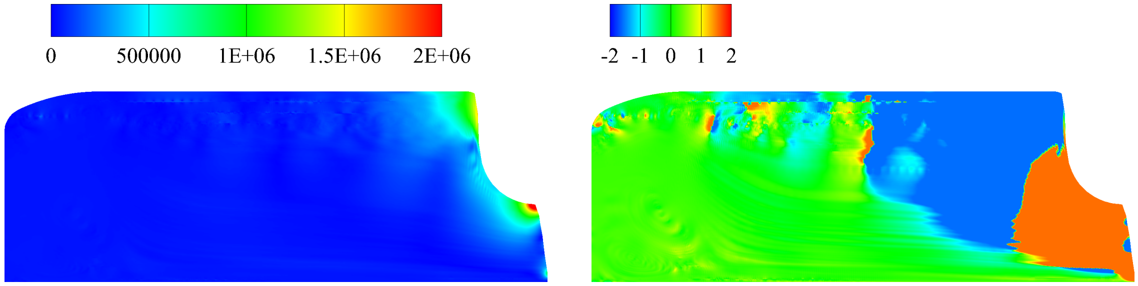

(g) Pressure magnitude [Pa].

(h) Pressure phase [rad].

Figure 7.16: Vortical velocities and pressure for the 1T mode.

7.6 Energy Integrands

Lastly, the vorticoacoustic stability analysis concludes with a quantified look at the unsteady energy transfer in the system through a variety of mechanisms dealing with flow work, vorticity, and combustion. These mechanisms, as defined in Chapter 5, all play some role in the driving or damping of the unsteady field. Breaking up the energy transfer sources in this manner not only provides a quantifiable modal stability report, but also reveals the connection between system design and its role in creating a stable or unstable environment.

Because this is a vorticoacoustic, not thermoacoustic analysis, the heat and entropy terms are not included presently. Nevertheless, some noteworthy flow features reveal themselves as a result of the bidirectional mean flow. The 1L mode results, as shown in Figure 7.17 reveal the most significant contributions to the unsteady field to be located along the shear layer, as well as an area around the fuel inlets. This is particularly noticeable with the vortex shedding and viscosity source terms, where viscosity and related effects would be expected to dominate. On the other hand, dissipation and surface work terms are directly proportional to velocity, and as such, are evident in the inner main vortex, with growth toward the exit plane. The 1T mode energy terms shown in Figure 7.18 are similar in nature to those in the 1L mode, with one primary exception along the wall tangent to the oxidizer inlets. Here, the terms that involve velocity have a second area of activity that contributes to the energy transferred to the unsteady field. Similar features can be seen in the higher modes through Figures D.13-D.16 shown in Appendix D.

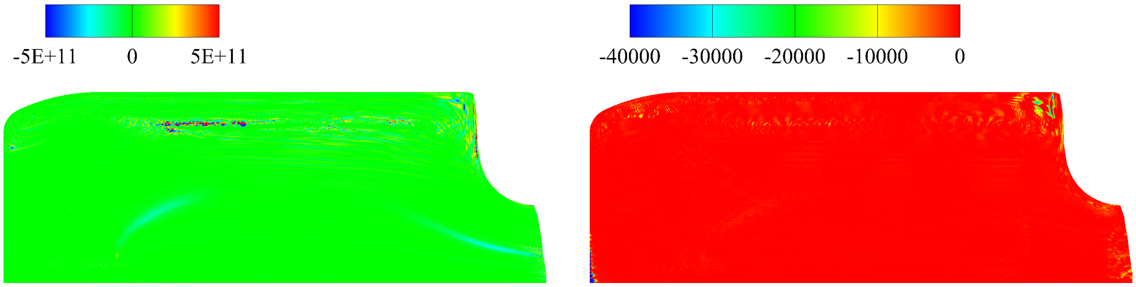

(a) 1L Vortex shedding [W/m^3]. (b) 1L Flow turning [W/m^3].

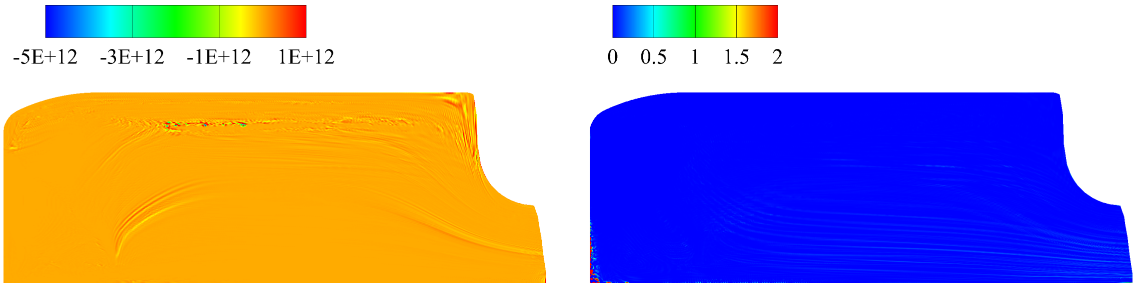

(c) 1L Surface work [W/m^3]. (d) 1L Dissipation [W/m^3].

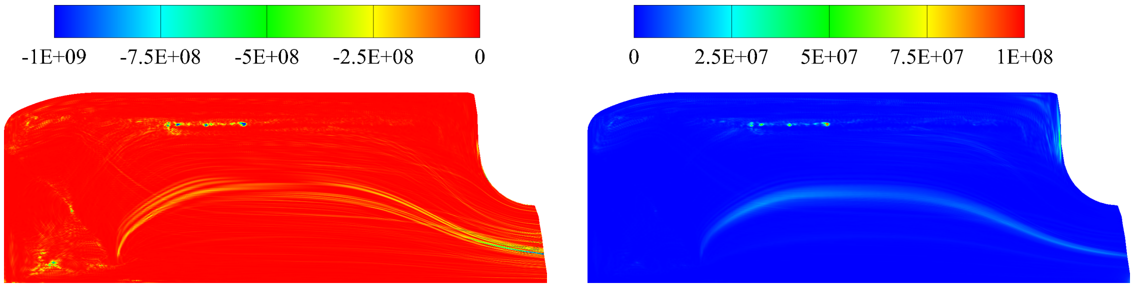

(e) 1L Viscous effects [W/m^3]. (f) 1L E_m^2 [J/m^3].

Figure 7.17: Energy integrands for the 1L mode.

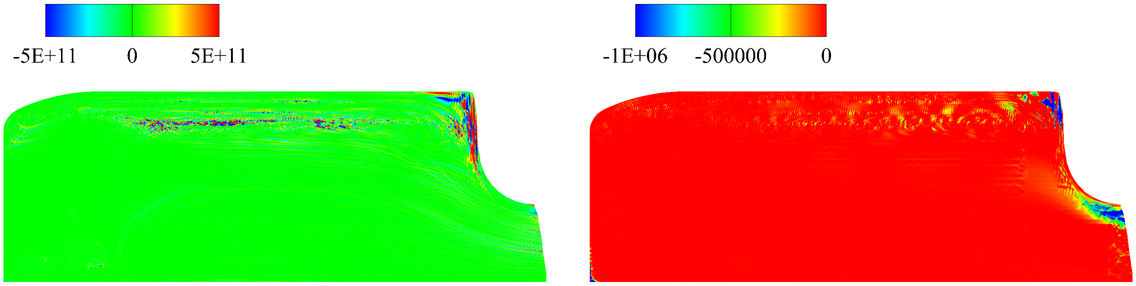

(a) 1T Vortex shedding [W/m^3].

(b) 1T Flow turning [W/m^3].

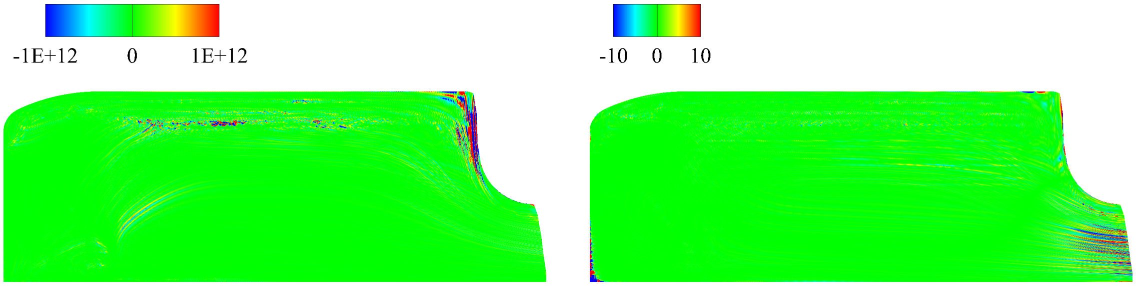

(c) 1T Surface work [W/m^3].

(d) 1T Dissipation [W/m^3].

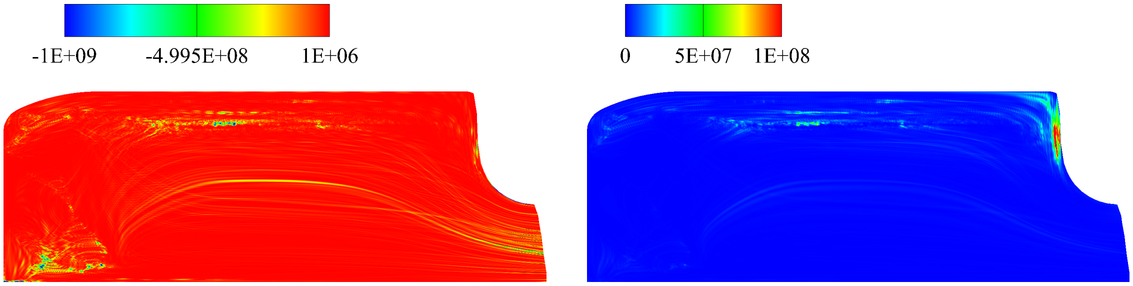

(e) 1T Viscous effects [W/m^3].

(f) 1T E_m^2 [J/m^3].

Figure 7.18: Energy integrands for the 1T mode.

7.7 Stability Analysis

Figures 7.19 and 7.20 visually reveal the stability trends, quantified in Table 7.5, of the five mechanisms primarily responsible for unsteady energy transfer in the bidiretional vortex engine. As could be expected for this type of engine, the vortex shedding mechanism plays the largest role in determining modal stability. While vortex shedding can act as a damper or driver of instability, traditional liquid rocket engines tend to have unstable tangential modes. That is also the case with the bidirectional vortex engine primarily due to vortex shedding. This activity can be seen in Figure 7.20a, where the shear layer between the axial, bidirectional vortices generates large amounts of vorticity. A secondary contributor to the stability margins of the tangential modes is the surface work mechanism. Though, generally, surface work is thought to be a negative term due to a variety of factors, which represents energy leaving the control volume, this term also takes into account energy entering the domain, potentially causing this term to be positive. The other stability terms are effectively negligible in the stability margins because of how they are defined. That is, with the flow turning mechanism, the steady vorticity term tends to be dominated by the unsteady vorticity term found in the vortex shedding mechanism. The viscous effects and dissipation terms likewise have terms dealing with viscosity and fluid friction heat generation, both of which are negligibly small terms for this system.

Moving to the pure longitudinal modes, a few similarities between the stability margins of the tangential and longitudinal modes can immediately be identified. The viscous effects, flow turning, and dissipation terms remain small for similar reasons as before, while vortex shedding and surface work continue to be the defining mechanisms in determining longitudinal stability. The primary difference is that the first three modes are stable, unlike the tangential modes, of which the first two are unstable. The integrand plots reveal that, while there is some activity again in the shear region of the driving vortices, some additional areas play a role as well, particularly a structure in the center vortex and the recirculation region near the headwall injectors.

Mode	Vortex Shedding	Flow Turning	Surface Work	Dissipation	Viscous Effects	E_m^2	Mode Total
1T	1631	$-8 \cdot 10^{-5}$	-358	$-6 \cdot 10^{-10}$	-5	3510	1269
2T	318	$-1 \cdot 10^{-3}$	60	$-2 \cdot 10^{-9}$	-6	8219	372
3T	-71	$-8 \cdot 10^{-3}$	26	$-9 \cdot 10^{-10}$	-7	514608	-53
1L	-517	$3 \cdot 10^{-5}$	-23	$-3 \cdot 10^{-9}$	-6	2000	-545
2L	-148	$2 \cdot 10^{-5}$	-26	$-4 \cdot 10^{-10}$	-6	9602	-180
3L	-735	$9 \cdot 10^{-7}$	249	$-8 \cdot 10^{-11}$	-6	1413455	-493

Table 7.5: Stability results for the first three pure tangential and longitudinal modes [1/s].

Drawing from literature and experience from combustion instability studies with axially-driven, liquid rocket engines, the vorticoacoustic analysis prediction that the longitudinal modes will be stable, while the first tangential mode will be the most unstable, is well within the realm of a reasonable conclusion of the stability of the bidirectional vortex engine. While this is the conclusion of the present study, the iterative process shown in Figure 7.1 would lead a design engineer to then take these stability results and determine whether they fall within acceptable margins for the engine to move along in the design process. If the results show the engine to be unacceptably unstable, the engine mean flow and geometry would then be modified to, perhaps in this particular case, reduce unsteady vorticity and increase nozzle damping as a means of reducing the surface work mechanism's contribution to instability.

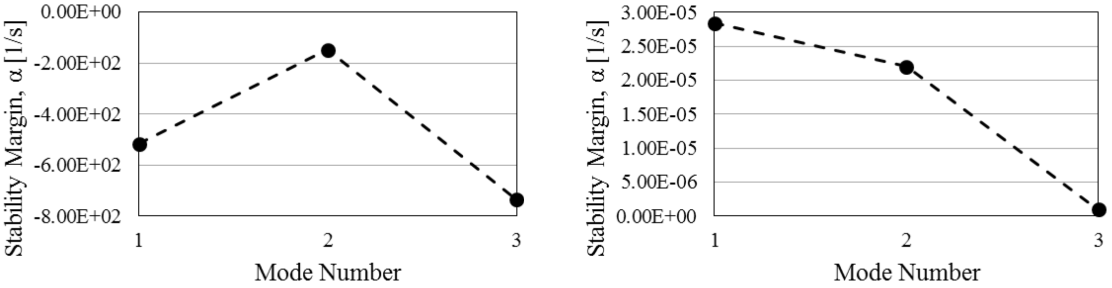

(a) Vortex shedding.

(b) Flow turning.

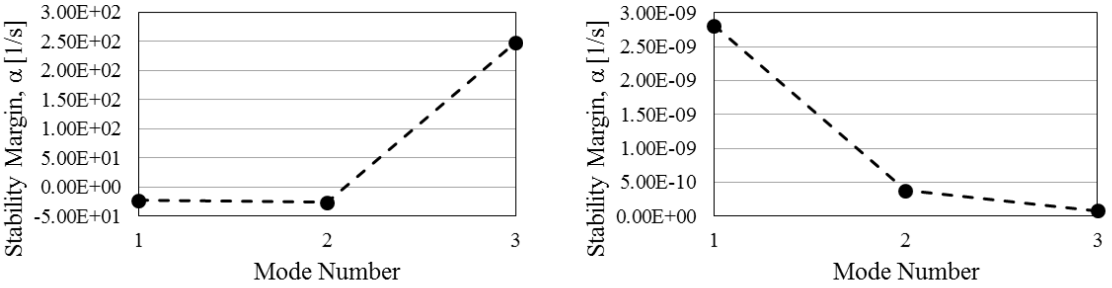

(c) Surface work.

(d) Dissipation.

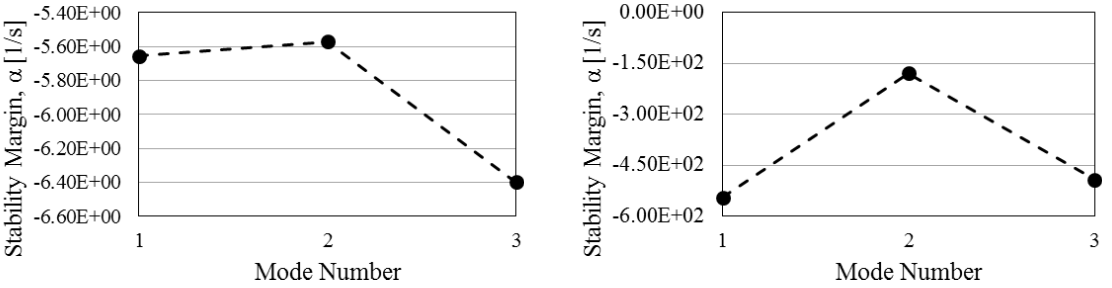

(e) Viscous Effects.

(f) Total modal stability margins.

Figure 7.19: Stability results for the first three pure longitudinal modes.

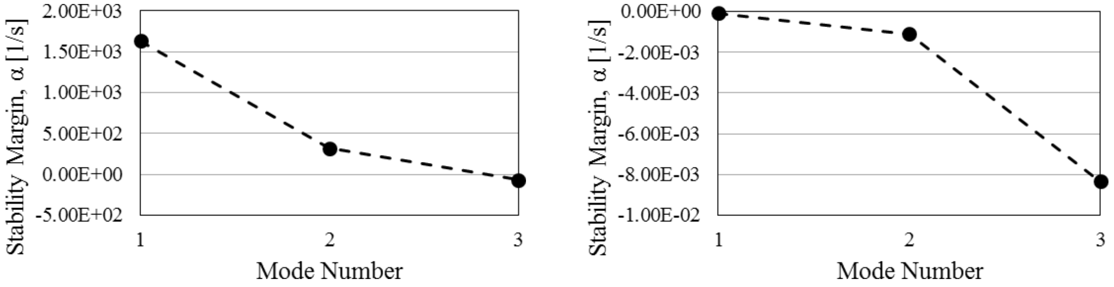

(a) Vortex shedding. (b) Flow turning.

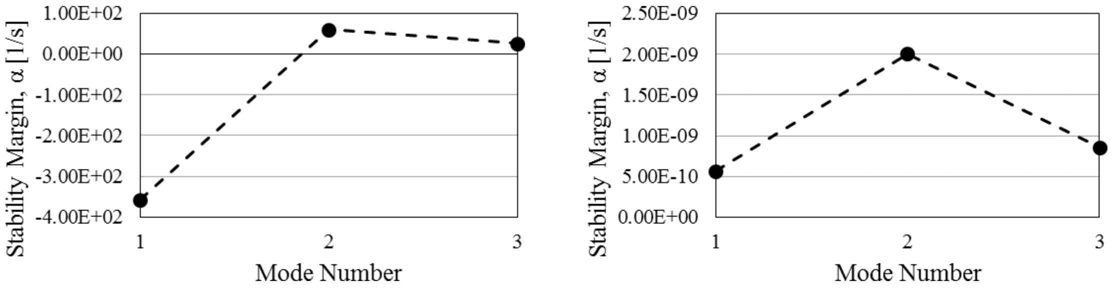

(c) Surface work. (d) Dissipation.

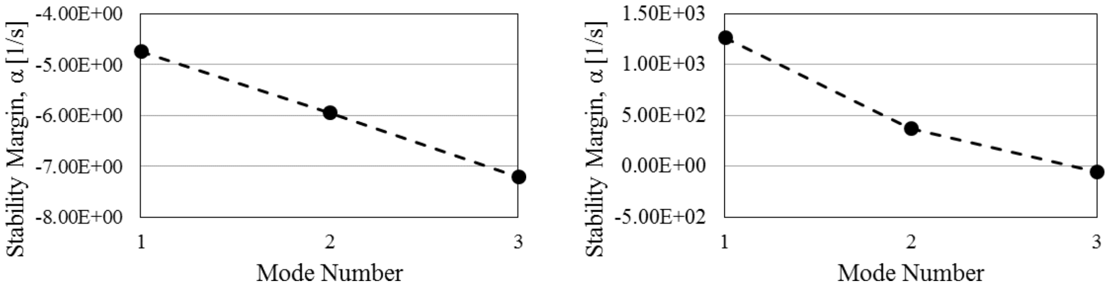

(e) Viscous Effects. (f) Total modal stability margins.

Figure 7.20: Stability results for the first three pure tangential modes.

Chapter 8

Conclusion

Combustion instability mitigation remains one of the most daunting tasks in the process of combustion-based propulsion system design. If left unchecked, instability issues can cause a wide berth of problems from merely reduced performance to total system destruction. Predictive analytical methods are effective in revealing the underlying physics, but fall short in fully uncovering unsteady energy transfer in reacting flows confined by irregular geometries. Experimental approaches likewise suffer from the inability to easily recover the individual modal contributions of the longitudinal and tangential waves. Furthermore, given the complex thermodynamic profile of modern engines, such as the bidirectional vortex engine in the present study, the departure from traditionally-understood acoustics gives rise to an entirely new set of problems. This is largely due to the steep temperature gradients that act as a semi-reflective boundary, which can have the effect of isolating acoustic waves while shifting cold flow frequencies substantially.

In conjunction with the acoustic field, the vortical field plays a significant role in instability. With mean flow effects considered, vorticity generated as an acoustic wave boundary layer correction can be convected into the flow. In some cases, distinct vortex cells emerge, shed at the acoustic frequency, and have a non-negligible impact on unsteady energy transfer. However, given that the vortical energy can be convected out the nozzle unlike acoustic energy, vorticity can be a strong damping factor while also being a contributor to driving the acoustic field.

Lastly, though the bidirectional vortex engine has a unique flow pattern as compared to a traditional, axially-driven liquid rocket engine, the two engines have notable similarities in that the 1T mode, operating at 1243 Hz, is the most unstable, while the longitudinal modes are of little concern in terms of stability. However, this thought-provoking result must be taken in light of the fact that this is a linear stability analysis, and as such, does not account for the true limit-cycle amplitude of any given mode. Thus, though it may be true that the 1T mode will grow most rapidly, the limit-cycle amplitude might be well within acceptable design tolerances for the engine, and this particular design of the engine will not have to be iterated upon at this developmental stage.

This outcome highlights some of the issues with the formulation of the vorticoacoustic solver used in the present study. The first assumption is that the flow can be accurately modeled as being axisymmetric. Future studies might reveal that the three-dimensional nature of real flows renders the axisymmetric assumption unacceptably inaccurate when considering system stability. This limitation is, more broadly, tied strongly to the CFD input used in the analysis, which has a whole host of separate issues that may prove to be starkly different from experimental instability results. Secondly, this entire study is built upon the linearization assumption of separating the flow into steady and unsteady components with one-way coupling, where only the mean flow affects the unsteady flow, and not the other way around. This assumption may not always prove capable of accounting for non-linear, impulse-based instability sources, or waves that produce oscillations with amplitudes in significant fractions, or even multiples, of the mean flow. In those cases, the linearization assumption could potentially break down. Thus, the ultimate computational combustion instability solver would be one that fully incorporates two-way coupling of a reacting, three dimensional flow, with all nonlinear and energy transfer mechanisms accounted for, by removing all assumptions about entropy and other variables being in any way negligible.

Nevertheless, much can be gleaned from a linear combustion instability study. Physical mechanisms that dominate the unsteady energy transfer can be identified and potentially corrected. Individual modal stability margins can also be determined so that the design engineer would know how to pick structural resonant modes and understand more about how to create an environment in the combustion system that works against instability growth.

Regardless of the approach used to determine combustion instability issues, it should be noted that only a small portion of the total chemical energy in the system is needed to trigger instability and that oscillation attenuation in the combustion chamber is difficult to achieve. This ultimately means that as new combustion-based propulsion systems continue to be developed, combustion instability issues must be anticipated from the earliest stages of engine design and considered to be part of the total developmental cost of pushing forward into the future of rocketry.

Bibliography

[1] Price, E. W. and Flandro, G. A., "Combustion Instability in Solid Propellant Rockets," Tech. Rep. 89-0460, Air Force Office of Scientific Research, 1989.

[2] Reardon, F. H., "Guidelines for Combustion Stability Specifications and Verification Procedures for Liquid Propellant Rocket Engines," Tech. Rep. 247, Chemical Propulsion Information Agency, 1973.

[3] Culick, F. E. C., "Combustion Instabilities in Liquid-Fuelled Propulsion Systems - an Overview," *AGARD Conference Proceedings*, Vol. 450, NATO, 1988, pp. 1–73.

[4] Huzel, D. K. and Huang, D. H., *Modern Engineering for Design of Liquid-Propellant Rocket Engines*, Vol. 147 of *Progress in Astronautics and Aeronautics*, American Institute of Aeronautics and Astronautics, 1992.

[5] Harrje, D. T. and Reardon, F. H., "Liquid Propellant Rocket Combustion Instability," Tech. Rep. SP-194, NASA, 1972.

[6] Scala, S., Grey, J., and Crocco, L., "Transverse Wave and Entropy Wave Combustion Instability in Liquid Propellant Rockets," Tech. Rep. 380, Princeton University, 1957.

[7] Reardon, F., Crocco, L., and Harrje, D. T., "An Investigation of Transverse Mode Combustion Instability in Liquid Propellant Rocket Motors," Tech. Rep. 550, Princeton University, 1961.

[8] Sirignano, W. A. and Pavel, P. P., "Two-Dimensional Model for Liquid-Rocket Transverse Combustion Instability," *AIAA Journal*, Vol. 51, No. 12, 2013, pp. 2919–2934.

[9] Blomshield, F., "Lessons Learned in Solid Rocket Combustion Instability," *43rd AIAA/ASME/SAE/ASEE Joint Propulsion Conference & Exhibit*, AIAA, 2007.

[10] Jacob, E. J., *A Study of Nonlinear Combustion Instability*, Ph.d. thesis, University of Tennessee, 2009.

[11] Powell, E., *Nonlinear Combustion Instability in Liquid Propellant Rocket Engines*, Ph.D. thesis, Georgia Institute of Technology, 1970.

[12] Higgins, B., "On the Sound Produced by a Current of Hydrogen Gas Passing Through a Tube," *Journal of Natural Philosophy, Chemistry, and the Arts*, Vol. 1, 1802, pp. 129–131.

[13] Le Conte, J., "On the Influence of Musical Sounds of the Flame of a Jet of Coal-Gas," *Philosophical Magazine*, Vol. 15, No. 99, 1858, pp. 235–239.

[14] Rijke, P. L., "Notice of a New Method of Causing a Vibration of the Air Contained in a Tube Open at Both Ends," *Philosophical Magazine and Journal of Science*, Vol. 17, No. 116, 1859, pp. 419–422.

[15] Basok, B. and Gotsulenko, V., "Self-Oscillations in a Rijke Tube with Receiver Positioning at Its Entrance," *Thermophysics and Aeromechanics*, Vol. 21, No. 4, 2014.

[16] Richardson, E. G., "The Theory of the Singing Flame," *Proceedings of the Physical Society of London*, Vol. 35, No. 1, 1922, pp. 47–54.

[17] Faraday, M., "On the Sounds Produced by Flame in Tubes," *The Journal of Science and the Arts*, Vol. 5, 1818, pp. 274–281.

[18] Soundhauss, C., "Ueber die Chemische Harmonika," *Annalen der Physik*, Vol. 185, No. 3, 1860, pp. 426–469.

[19] Zoch, I., "Einiges zur Kenntniss der Chemischen Harmonica," *Annalen der Physik*, Vol. 203, No. 4, 1866, pp. 580–593.

[20] Terquem, A., "Ueber die Chemische Harmonika," *Annalen der Physik*, Vol. 210, No. 7, 1868, pp. 468–472.

[21] Rayleigh, J. W. S., *The Theory of Sound*, Vol. 1, Macmillan and Co., London, 1877.

[22] Rayleigh, J. W. S., "The Explanation of Certain Acoustical Phenomena," *Nature*, Vol. 18, 1878, pp. 319–321.

[23] Rayleigh, J. W. S., "On the Stability, or Instability, of Certain Fluid Motions," *Proceedings of the London Mathematical Society*, Vol. 11, No. 1, 1880, pp. 57–70.

[24] Culick, F. E. C. and Yang, V., *Instability Phenomenology and Case Studies: Overview of Combustion Instabilities in Liquid-Propellant Rocket Engines*, Vol. 169 of *Progress in Astronautics and Aeronautics*, book section 1, American Institute of Aeronautics and Astronautics, Washington, District of Columbia, 1995, pp. 3–37.

[25] Crocco, L., "Aspects of Combustion Stability in Liquid Propellant Rocket Motors Part I: Fundunamentals. Low Frequency Instability with Monopropellants," *Journal of the American Rocket Society*, Vol. 21, No. 6, 1951, pp. 163–178.

[26] Hart, R. W. and McClure, F. T., "Combustion Instability: Acoustic Interaction with a Burning Propellant Surface," *The Journal of Chemical Physics*, Vol. 30, No. 6, 1959, pp. 1501–1514.

[27] Hart, R. W. and McClure, F. T., "Theory of Acoustic Instability in Solid-Propellant Rocket Combustion," *Tenth Symposium (International) on Combustion*, Vol. 10, No. 1, 1965, pp. 1047–1066.

[28] Hart, R. W. and Cantrell, R. H., "Amplification and Attenuation of Sound by Burning Propellants," *AIAA Journal*, Vol. 1, No. 2, 1963, pp. 398–404.

[29] Cantrell, R. H. and Hart, R. W., "Interaction Between Sound and Flow in Acoustic Cavities: Mass, Momentum, and Energy Considerations," *Journal of the Acoustical Society of America*, Vol. 36, No. 4, 1964, pp. 697–706.

[30] Culick, F. E. C., "Stability of High Frequency Pressure Oscillations in Rocket Combustion Chambers," *AIAA Journal*, Vol. 1, No. 5, 1963, pp. 1097–1104.

[31] Culick, F. E. C., "Acoustic Oscillations in Solid Propellant Rocket Chambers," *Acta Astronautica*, Vol. 12, No. 2, 1966, pp. 113–126.

[32] Oefelein, J. C. and Yang, V., "Comprehensive Review of Liquid-Propellant Combustion Instabilities in F-1 Engines," *Journal of Propulsion and Power*, Vol. 9, No. 5, 1993, pp. 657–677.

[33] Fisher, S. C. and Rahman, S. A., *Remembering the Giants: Apollo Rocket Propulsion Development*, Vol. 45 of *Monograph in Aerospace History*, NASA, John C. Stennis Space Center, 2009.

[34] Ellison, L. R. and Moser, M. D., "Combustion Instability Analysis and the Effects of Drop Size on Acoustic Driving Rocket Flow," *52nd JANNAF Joint Propulsion Meeting*, 2004.

[35] McCranie, J., "F-1 Rocket Engine at KSC," 2010, https://upload.wikimedia.org/wikipedia/commons/1/1d/F-1_rocket_engine_at_KSC.jpg, Accessed Online January 4, 2016.

[36] Hutchinson, L., "F-1 Engine Injector Plate," 2013, http://cdni.wired.co.uk/620x413/d_f/f1-.jpg, Accessed Online January 4, 2016.

[37] Priem, R. J. and Guentert, D. C., "Combustion Instability Limits Determined by a Nonlinear Theory and a One-Dimensional Model," Tech. Rep. D-1409, NASA, 1962.

[38] Povinelli, L. A., "One-Dimensional Nonlinear Model for Determining Combustion Instability in Solid Propellant Rocket Motors," Tech. Rep. TN D-3410, NASA, 1966.

[39] Brownlee, W. G. and Marble, F. E., "An Experimental Investigation of Unstable Combustion in Solid Propellant Rocket Motors," *AIAA Progress in Astronautics and Rocketry: Solid Propellant Rocket Research*, Vol. 1, 1960, pp. 455–494.

[40] Temkin, S., "Nonlinear Gas Oscillations in a Resonant Tube," *Physics of Fluids*, Vol. 11, No. 5, 1968, pp. 960–963.

[41] Chester, W., "Resonant Oscillations in Closed Tubes," *Journal of Fluid Mechanics*, Vol. 18, No. 1, 1964, pp. 44–64.

[42] Crocco, L., Harrje, D. T., and Reardon, F. H., "Transverse Combustion Instability in Liquid Propellant Rocket Motors," *Journal of the American Rocket Society*, Vol. 32, No. 3, 1962, pp. 366–373.

[43] Reardon, F. H., Crocco, L., and Harrje, D. T., "Velocity Effects in Transverse Mode Liquid Propellant Rocket Combustion Instability," *AIAA Journal*, Vol. 2, No. 9, 1964, pp. 1631–1641.

[44] Krieg, Jr., H. C., *Tangential Mode of Combustion Instability*, Vol. 6 of *Progress in Astronautics and Rocketry*, book section Part 2, American Institute of Aeronautics and Astronautics, New York, 1962, pp. 339–366.

[45] Heidmann, M. F., "Performance Study of Rotating Gas Jet Generator for Strong Traveling Transverse Acoustic Modes," Tech. Rep. D-4380, NASA, 1968.

[46] Flandro, G. A., "Vortex Driving Mechanisms in Oscillatory Rocket Flows," *Journal of Propulsion and Power*, Vol. 2, No. 3, 1986, pp. 206–214.

[47] Jensen, F. R., "Space Shuttle Response to Acoustic Combustion Instability in the Solid Rocket Boosters," Tech. Rep. 76-62, Hercules Incorporated, Bacchus Works, 1976.

[48] Majdalani, J., "The Oscillatory Channel Flow with Arbitrary Wall Injection," *Journal of Applied Mathematics and Physics (ZAMP)*, Vol. 52, No. 1, 2001, pp. 33–61.

[49] Majdalani, J., "Vortical and Acoustical Mode Coupling Inside a Two-Dimensional Cavity with Transpiring Walls," *Journal of the Acoustical Society of America*, Vol. 106, No. 1, 1999, pp. 46–56.

[50] Majdalani, J., "Multiple Asymptotic Solutions for Axially Travelling Waves in Porous Channels," *Journal of Fluid Mechanics*, Vol. 636, No. 1, 2009, pp. 59–89, NSF.

[51] Majdalani, J. and Flandro, G. A., "The Oscillatory Pipe Flow with Arbitrary Wall Injection," *Proceedings of the Royal Society A: Mathematical, Physical and Engineering Sciences*, Vol. 458, 2002, pp. 1621–1651.

[52] Majdalani, J. and Roh, T. S., "The Oscillatory Channel Flow with Large Wall Injection," *Proceedings of the Royal Society of London, Series A*, Vol. 456, No. 1999, 2000, pp. 1625–1657.

[53] Akiki, M., Batterson, J. W., and Majdalani, J., "Biglobal Stability of Compressible Flowfields. Part 1: Planar Formulation," 2013.

[54] Akiki, M., Batterson, J. W., and Majdalani, J., "Biglobal Stability of Compressible Flowfields. Part 2: Application to Solid Rocket Motors," *49th AIAA/ASME/SAE/ASEE Joint Propulsion Conference*, 2013.

[55] Batterson, J. and Majdalani, J., "Biglobal Instability of the Bidirectional Vortex. Part 1: Formulation," *47th AIAA/ASME/SAE/ASEE Joint Propulsion Conference and Exhibit*, AIAA, 2011.

[56] Batterson, J. and Majdalani, J., "Biglobal Instability of the Bidirectional Vortex. Part 2: Complex Lamellar and Beltramian Motions," *47th AIAA/ASME/SAE/ASEE Joint Propulsion Conference and Exhibit*, AIAA Paper 2011-5649, 2011.

[57] Elliott, T. S. and Majdalani, J., "Two-Phase Flow Stability of Cylindrically-Shaped Hybrid and Solid Rockets with Particle Entrainment," *50th AIAA/ASME/SAE/ASEE Joint Propulsion Conference and Conference*, AIAA Paper 2014-3611, Cleveland, OH, July 2014.

[58] Elliott, T. S. and Majdalani, J., "Hydrodynamic Stability Analysis of Particle-Laden Solid Rocket Motors," *Journal of Physics: Conference Series*, Vol. 548/1/012064, Tullahoma, TN, July 2014, p. 012064, XXII International Conference on Spectral Line Shapes (ICSLS 2014).

[59] Elliott, T. S. and Majdalani, J., "Effect of Outflow Boundary Conditions on the Stability of Cylindrically-Shaped Hybrid Rockets," *51st AIAA/ASME/SAE/ASEE Joint Propulsion Conference and Exhibit*, AIAA Paper 2015-3744, Orlando, FL, July 2015.

[60] Fischbach, S. R., Majdalani, J., and Flandro, G. A., "Acoustic Instability of the Slab Rocket Motor," *Journal of Propulsion and Power*, Vol. 23, No. 1, 2007, pp. 146–157.

[61] Fischbach, S. R., Flandro, G. A., and Majdalani, J., "Acoustic Streaming in Simplified Liquid Rocket Engines with Transverse Mode Oscillations," *Physics of Fluids*, Vol. 22, No. 6, 2010, pp. 063602–21.

[62] Fischbach, S. R. and Majdalani, J., "Volume-to-Surface Reduction of Vorticoacoustic Stability Integrals," *Journal of Sound and Vibration*, Vol. 321, No. 3-5, April 2009, pp. 1007–1025, NSF.

[63] Flandro, G. A., "Effects of Vorticity on Rocket Combustion Stability," *Journal of Propulsion and Power*, Vol. 11, No. 4, 1995, pp. 607–625.

[64] Haddad, C. T. and Majdalani, J., "Transverse Waves in Simulated Liquid Rocket Engines," *AIAA Journal*, Vol. 51, No. 3, 2013, pp. 591–605.

[65] Haddad, C. T. and Majdalani, J., "Sidewall Boundary Layer of Transverse Waves in Simulated Liquid Rocket Engines," *AIAA Journal*, Vol. 51, No. 8, 2013, pp. 1820–1827.

[66] Casalis, G., Avalon, G., and Pineau, J. P., "Spatial Instability of Planar Channel Flow with Fluid Injection Through Porous Walls," *Physics of Fluids*, Vol. 10, No. 10, 1998, pp. 2558–2568.

[67] Griffond, J., Casalis, G., and Pineau, J. P., "Spatial Instability of Flow in a Semiinfinite Cylinder with Fluid Injection through Its Porous Walls," *European Journal of Mechanics - B/Fluids*, Vol. 19, No. 1, 2000, pp. 69–87.

[68] Griffond, J. and Casalis, G., "On the Nonparallel Stability of the Injection Induced Two-Dimensional Taylor Flow," *Physics of Fluids*, Vol. 13, No. 6, June 2001, pp. 1635–1644.

[69] Chedevergne, F., Casalis, G., and Majdalani, J., “Direct Numerical Simulation and Biglobal Stability Investigations of the Gaseous Motion in Solid Rocket Motors,” *Journal of Fluid Mechanics*, Vol. 706, 2012, pp. 190–218.

[70] Chedevergne, F., Casalis, G., and Fraille, T., “Biglobal Linear Stability Analysis of the Flow Induced by Wall Injection,” *Physics of Fluids*, Vol. 18, No. 1, 2006, pp. 014103–14.

[71] Boyer, G., Casalis, G., and Estivalzes, J. L., “Stability and Sensitivity Analysis in a Simplified Solid Rocket Motor Flow,” *Journal of Fluid Mechanics*, Vol. 722, 2013, pp. 618–644.

[72] Boyer, G., Casalis, G., and Estivalezes, J. L., “Stability Analysis and Numerical Simulation of Simplified Solid Rocket Motors,” *Physics of Fluids*, Vol. 25, No. 8, 2013, pp. 084109–084109.

[73] Morse, P. M. and Ingard, K. U., *Theoretical Acoustics*, Princeton University Press, Princeton, New Jersey, 1968.

[74] Wasistho, B., Balachandar, S., and Moser, R. D., “Compressible Wall-Injection Flows in Laminar, Transitional, and Turbulent Regimes: Numerical Prediction,” *Journal of Spacecraft and Rockets*, Vol. 41, No. 6, 2004, pp. 915–924.

[75] Brown, R. S., Blackner, A. M., Willoughby, P. G., and Dunlap, R., “Coupling Between Acoustic Velocity Oscillations and Solid Propellant Combustion,” *Journal of Propulsion and Power*, Vol. 2, No. 5, 1986, pp. 428–437.

[76] Harvazinski, M. E., Anderson, W. E., and Merkle, C. L., “Analysis of Self-Excited Combustion Instabilities Using Two- and Three-Dimensional Simulations,” *Journal of Propulsion and Power*, Vol. 29, No. 2, 2013, pp. 396–409.

[77] Chu, B. T. and Kovsznay, L. S. G., “Non-Linear Interactions in a Viscous Heat-Conducting Compressible Gas,” *Journal of Fluid Mechanics*, Vol. 3, No. 5, 1958, pp. 494–514.

[78] Majdalani, J., *Improved Flowfield Models in Rocket Motors and the Stokes Layer with Sidewall Injection*, Ph.D. thesis, University of Utah, 1995.

[79] de Bruin, I., Wasistho, B., Geurts, B. J., Kuerten, J., and Zandbergen, P., “Simulation of Subsonic Spatially Developing Turbulent Shear Flows,” *Sixteenth International Conference on Numerical Methods in Fluid Dynamics*, Vol. 515, 1998, pp. 147–152.

[80] Jacob, E. J., Flandro, G. A., and Rice, T., “The Effect of Unsteady Entropy on Combustion Instability,” *48th AIAA/ASME/SAE/ASEE Joint Propulsion Conference & Exhibit*, American Institute of Aeronautics and Astronautics, 2012.

[81] Jacob, E. J. and Batterson, J. W., “The Generalized Rayleigh Criterion and Other Entropic Contributions to Combustion Instability,” *49th AIAA/ASME/SAE/ASEE Joint Propulsion Conference*, American Institute of Aeronautics and Astronautics, 2013.

[82] Tam, C. K. W., *Computational Aeroacoustics: Methods and Applications*, AIAA Short Course, American Institute of Aeronautics and Astronautics, Hilton Head, SC, 2003.

[83] Yoon, J., "Prediction of Longitudinal Combustion Instability in a Solid-Propellant Rocket Motor," *Journal of Mechanical Science and Technology*, Vol. 8, No. 2, 1994, pp. 206–213.

[84] Culick, F. E. C., "Non-Linear Growth and Limiting Amplitude of Acoustic Oscillations in Combustion Chambers," *Combustion Science and Technology*, Vol. 3, No. 1, 1971, pp. 1–16.

[85] Wicker, J. M., Greene, W. D., Kim, S. I., and Yang, V., "Triggering of Longitudinal Combustion Instabilities in Rocket Motors: Nonlinear Combustion Response," *Journal of Propulsion and Power*, Vol. 12, No. 6, 1996, pp. 1148–1158.

[86] Jacob, E. J., Flandro, G. A., Gloyer, P. W., and French, J. C., "Nonlinear Liquid Rocket Combustion Instability Behavior Using UCDS™Process," *46th AIAA/ASME/SAE/ASEE Joint Propulsion Conference and Exhibit*, AIAA, 2010.

[87] Batterson, J., "On the Formulation and Numeric Solution of Vortico-Acoustic Fields," *51st AIAA Aerospace Sciences Meeting Including the New Horizons and Aerospace Exposition*, 2013.

[88] Campos, L. M. B. C., "On 36 Forms of the Acoustic Wave Equation in Potential Flows and Inhomogeneous Media," *Applied Mechanics Reviews*, Vol. 60, No. 4, 2007, pp. 149–171.

[89] Campos, L. M. B. C., "On 24 Forms of the Acoustic Wave Equation in Vortical Flows and Dissipative Media," *Applied Mechanics Reviews*, Vol. 60, No. 6, 2007, pp. 291–315.

[90] Sigman, R. K. and Zinn, B. T., "A Finite Element Approach For Predicting Nozzle Admittances," *Journal of Sound and Vibration*, Vol. 88, No. 1, 1983, pp. 117–131.

[91] French, J. C., "Nozzle Acoustic Dynamics and Stability Modeling," *Journal of Propulsion and Power*, Vol. 27, No. 6, 2011, pp. 1266–1275.

[92] Theofilis, V., "Advances in Global Linear Instability Analysis on Nonparallel and Three-Dimensional Flows," *Progress in Aerospace Sciences*, Vol. 39, No. 4, 2003, pp. 249–315.

[93] Jacob, E. J. and Batterson, J. W., "Determining Sources of Unsteady Energy Transfer in Time-Accurate Computational Fluid Dynamics," *Journal of Propulsion and Power*, Vol. 31, No. 1, 2015, pp. 332–341.

[94] Casalis, G. and Vuillot, F., "Motor Flow Instabilities - Part 2. Intrinsic Linear Stability of the Flow Induced by Wall Injection," Tech. rep., ONERA, 2002.

[95] Tissuer, F. and Meerbergen, K., "The Quadratic Eigenvalue Problem," *SIAM Review*, Vol. 43, No. 2, 2001, pp. 235–286.

[96] Majdalani, J., "Asymptotic Formulation for an Acoustically Driven Field Inside a Rectangular Cavity With a Well-Defined Convective Mean Flow Motion," *Journal of Sound and Vibration*, Vol. 223, No. 1, 1999, pp. 73–95.

[97] Flandro, G. A., "On Flow Turning," *31st AIAA/ASME/SAE/ASEE Joint Propulsion Conference*, American Institute of Aeronautics and Astronautics, 1995.

[98] Janardan, B. A., *Damping of Axial Instabilites by Solid Propellant Rocket Exhaust Nozzles*, Ph.D. thesis, Georgia Institute of Technology, 1973.

[99] Kirchhoff, G., *Vorlesungen ber Mathematische Physik: Mechanik*, B. G. Teubner, Leibzig, 1877.

[100] Jacob, E. J., Flandro, G. A., and Gloyer, P. W., "Nonlinear Energy Transfer Applied to Data Analysis in Combustion Instability," *47th AIAA/ASME/SAE/ASEE Joint Propulsion Conference and Exhibit*, American Institute of Aeronautics and Astronautics, 2011.

[101] Chu, B. T., "On the Energy Transfer to Small Disturbances in Fluid Flow (Part I)," *Acta Mechanica*, Vol. 1, No. 3, 1965, pp. 215–234.

[102] Myers, M. K., "Transport of Energy by Disturbances in Arbitrary Steady Flows," *Journal of Fluid Mechanics*, Vol. 226, 1991, pp. 383–400.

[103] Flandro, G. A., Fischbach, S. R., and Majdalani, J., "Nonlinear Rocket Motor Stability Prediction: Limit Amplitude, Triggering, and Mean Pressure Shift," *Physics of Fluids*, Vol. 19, No. 9, 2007, pp. 094101–16.

[104] Flandro, G. A., "On the Oscillatory Behavior of Liquid Propellant Rockets," *International Journal of Energetic Materials and Chemical Propulsion*, Vol. 7, No. 4, 2008, pp. 315–358.

[105] Hamman, C. W., Klewicki, J. C., and Kirby, R. M., "On the Lamb Vector Divergence in Navier-Stokes Flows," *Journal of Fluid Mechanics*, Vol. 610, 2008, pp. 261–284.

[106] Wu, J. Z., Ma, H. Y., and Zhou, M. D., *Vorticity and Vortex Dynamics*, Springer, New York, 2006.

[107] Flandro, G. A. and Majdalani, J., "Aeroacoustic Instability in Rockets," *AIAA Journal*, Vol. 41, No. 3, 2003, pp. 485–497.

[108] Zhao, Q., Staab, P. L., Kassoy, D. R., and Kirkköprü, K., "Acoustically Generated Vorticity in an Internal Flow," *Journal of Fluid Mechanics*, Vol. 413, 2000, pp. 247–285.

[109] Lighthill, M. J., "On Sound Generated Aerodynamically. I. General Theory," *Proceedings of the Royal Society A: Mathematical, Physical and Engineering Sciences*, Vol. 211, No. 1107, 1952, pp. 564–587.

[110] Lighthill, M. J., "On Sound Generated Aerodynamically. II. Turbulence as a Source of Sound," *Proceedings of the Royal Society A: Mathematical, Physical and Engineering Sciences*, Vol. 222, No. 1148, 1954, pp. 1–32.

[111] Helmholtz, H. L. F., *On the Sensations of Tone as a Physiological Basis for the Theory of Music*, Longmans, Green, and Co., 1st ed., 1863.

[112] Kovacic, P., Batterson, J. W., and Majdalani, J., "Transverse Vortico-Acoustic Waves in the Presence of Strong Mean Flow Shear Layers," *51st AIAA/SAE/ASEE Joint Propulsion Conference*, 2015.

[113] Thomée, V., "From Finite Differences to Finite Elements: A Short History of Numerical Analysis of Partial Differential Equations," *Journal of Computational and Applied Mathematics*, Vol. 128, No. 1, 2001, pp. 1–54.

[114] Clough, R. W., "The Finite Element Method in Plane Stress Analysis," *Proceedings of the Second American Society of Civil Engineers Conference on Electronic Computation*, Vol. 8, 1960, pp. 345–378.

[115] Turner, M. J., Clough, R. W., Martin, H. C., and Topp, L. J., "Stiffness and Deflection Analysis of Complex Structures," *Journal of the Aeronautical Sciences*, Vol. 23, No. 9, 1956, pp. 805–823.

[116] Waring, E., "Problems Concerning Interpolations," *Philosophical Transactions of the Royal Society of London*, Vol. 69, 1779, pp. 59–67.

[117] Meijering, E., "A Chronology of Interpolation: From Ancient Astronomy to Modern Signal and Image Processing," *Proceedings of the IEEE*, Vol. 90, No. 3, 2002, pp. 319–342.

[118] Epperson, J. F., "On the Runge Example," *American Mathematical Monthly*, Vol. 94, No. 4, 1987, pp. 329–341.

[119] Berrut, J. P. and Trefethen, L. N., "Barycentric Lagrange Interpolation," *SIAM Review*, Vol. 46, No. 3, 2004, pp. 501–517.

[120] Patankar, S., *Numerical Heat Transfer and Fluid Flow*, Computational Methods in Mechanics and Thermal Sciences, Hemisphere Publishing Corporation, 1980.

[121] Farrashkhalvat, M. and Miles, J. P., *Basic Structured Grid Generation*, Butterworth-Heinemann, Burlington, MA, 2003.

[122] Rietema, K., "Performance of Design of Hydrocyclones - I: General Considerations," *Chemical Engineering Science*, Vol. 15, No. 3-4, 1961, pp. 298–302.

Appendices

Appendix A

Irregular Gridding Derivation

Though in many cases solving a finite differencing problem using a regularly-spaced grid may be adequate, there could be situations where having the ability to utilize an irregular grid would be more useful. For example, irregular gridding could be used to capture the fine details of a boundary layer region by densely gridding that area while simultaneously reducing computational time by sparsely gridding the regions away from the boundary layer region. In what follows, the derivation of ordered, non-uniform 1D grids will be explained in detail. As expounded upon in Chapter 6, this derivation is based on Lagrangian interpolation for equally-space 1D gridding. However, it is best to return to the Lagrangian interpolant to derive these equations, for while a secondary interpolation to find the centrally-located point x_i is possible, it is quite inefficient and will hinder the process of finding higher order difference methods as well.

A.1 First Derivatives

A.1.1 Central Difference

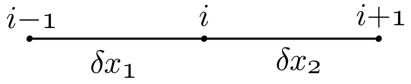

Figure A.1: First derivative central differencing diagram setup.

Figure A.1 shows the setup of the three gridpoints used in a central differencing algorithm, where

$$\delta x_1 = x_i - x_{i-1} \tag{A.1}$$

$$\delta x_2 = x_{i+1} - x_i \tag{A.2}$$

are defined for purposes of condensing the equations. To begin, the Lagrangian interpolation polynomial of the form is differentiated

$$f(x) \approx L(x) = \sum_{i=1}^{N} f(x_i)\, l_i(x) \tag{A.3}$$

where only $l_i - 1$, l_i, and $l_i + 1$ are differentiated, since f_i is simply the function value at x_i, not the function itself. Doing so results in an expression for the centrally-differenced derivative at grid point x_i,

$$f'(x_i) \approx a_i f(x_{i-1}) + b_i f(x_i) + c_i f(x_{i+1}) \tag{A.4}$$

Solving now for the coefficients a_i, b_i, and c_i, the three Lagrange basis polynomials, $l_i - 1$, l_i, and $l_i + 1$, are derived for their respective three grid points located about grid point x_i,

$$l_{i-1} = \frac{x - x_i}{x_{i-1} - x_{i+1}} \frac{x - x_{i+1}}{x_{i-1} - x_{i+1}} = \frac{x^2 - x(x_{i+1} + x_i) + x_i x_{i+1}}{\delta x_1 (\delta x_1 + \delta x_2)} \tag{A.5}$$

$$l_i = \frac{x - x_{i-1}}{x_i - x_{i-1}} \frac{x - x_{i+1}}{x_i - x_{i+1}} = -\frac{x^2 - x(x_{i+1} + x_{i-1}) + x_{i-1} x_{i+1}}{\delta x_1 \delta x_2} \tag{A.6}$$

$$l_{i+1} = \frac{x - x_{i-1}}{x_{i+1} - x_{i-1}} \frac{x - x_i}{x_{i+1} - x_i} = \frac{x^2 - x(x_i + x_{i-1}) + x_{i-1} x_i}{\delta x_2 (\delta x_1 + \delta x_2)} \tag{A.7}$$

Next, their derivatives are taken

$$l'_{i-1}(x) = \frac{2x - (x_{i+1} + x_i)}{\delta x_1 (\delta x_1 + \delta x_2)} \tag{A.8}$$

$$l'_i(x) = \frac{2x - (x_{i+1} + x_{i+1})}{\delta x_1 \delta x_2} \tag{A.9}$$

$$l'_{i+1}(x) = \frac{2x - (x_i + x_{i-1})}{\delta x_2 (\delta x_1 + \delta x_2)} \tag{A.10}$$

and then evaluated at x_i.

$$a_i = l'_{i-1}\left(x_i\right) = \frac{2x_i - \left(x_{i+1} + x_i\right)}{\delta x_1 \left(\delta x_1 + \delta x_2\right)} = \frac{\delta x_2}{\delta x_1 \left(\delta x_1 + \delta x_2\right)} \tag{A.11}$$

$$b_i = l'_i\left(x_i\right) = \frac{2x_i - \left(x_{i+1} + x_{i-1}\right)}{\delta x_1 \delta x_2} = \frac{\delta x_2 - \delta x_1}{\delta x_1 \delta x_2} \tag{A.12}$$

$$c_i = l'_{i+1}\left(x_i\right) = \frac{2x_i - \left(x_i + x_{i-1}\right)}{\delta x_2 \left(\delta x_1 + \delta x_2\right)} = \frac{\delta x_1}{\delta x_2 \left(\delta x_1 + \delta x_2\right)} \tag{A.13}$$

A.1.2 Forward Difference

The forward differencing formula is derived in a similar manner, as shown in Figure A.2, where

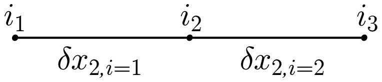

Figure A.2: First derivative forward differencing diagram setup.

$$\delta x_{2,i=1} = x_2 - x_1 \tag{A.14}$$

$$\delta x_{2,i=2} = x_3 - x_2 \tag{A.15}$$

and the expression for the derivative at x_1 is written as

$$f'\left(x_1\right) \approx a_1 f\left(x_1\right) + b_1 f\left(x_2\right) + c_1 f\left(x_3\right) \tag{A.16}$$

Solving now for the coefficients a_1, b_1, and c_1, the three Lagrange basis polynomials, l_1, l_2, and l_3, are derived for their respective three grid points located about grid point x_1.

$$l_1 = \frac{x - x_2}{x_1 - x_2}\frac{x - x_3}{x_1 - x_3} = \frac{x^2 - x\left(x_3 + x_2\right) + x_2 x_3}{\delta x_{2,i=1}\left(dx_{2,i=1} + dx_{2,i=2}\right)} \tag{A.17}$$

$$l_2 = \frac{x - x_1}{x_2 - x_1}\frac{x - x_3}{x_2 - x_3} = -\frac{x^2 - x\left(x_3 + x_1\right) + x_1 x_3}{\delta x_{2,i=1}\delta x_{2,i=2}} \tag{A.18}$$

$$l_3 = \frac{x - x_1}{x_3 - x_2}\frac{x - x_2}{x_3 - x_1} = \frac{x^2 - x\left(x_1 + x_2\right) + x_1 x_2}{\delta x_{2,i=2}\left(\delta x_{2,i=1} + \delta x_{2,i=2}\right)} \tag{A.19}$$

Next, their derivatives are taken

$$l_1'\left(x\right) = \frac{2x - \left(x_3 + x_2\right)}{\delta x_{2,i=1}\left(\delta x_{2,i=1} + \delta x_{2,i=2}\right)} \tag{A.20}$$

$$l_2'\left(x\right) = -\frac{2x - \left(x_3 + x_1\right)}{\delta x_{2,i=1}\delta x_{2,i=2}} \tag{A.21}$$

$$l_3'\left(x\right) = \frac{2x - \left(x_1 + x_2\right)}{\delta x_{2,i=2}\left(\delta x_{2,i=1} + \delta x_{2,i=2}\right)} \tag{A.22}$$

and then evaluated at x_1,

$$\begin{aligned} a_1 = l_1'\left(x_1\right) &= \frac{2x_1 - \left(x_3 + x_2\right)}{\delta x_{2,i=1}\left(\delta x_{2,i=1} + \delta x_{2,i=2}\right)} \\ &= -\frac{2\delta x_{2,i=1} + \delta x_{2,i=2}}{dx_{2,i=1}\left(\delta x_{2,i=1} + \delta x_{2,i=2}\right)} \end{aligned} \tag{A.23}$$

$$\begin{aligned} b_1 = l_2'\left(x_1\right) &= -\frac{2x_1 - \left(x_3 + x_1\right)}{\delta x_{2,i=1}\delta x_{2,i=2}} \\ &= \frac{\delta x_{2,i=1} + \delta x_{2,i=2}}{\delta x_{2,i=1}\delta x_{2,i=2}} \end{aligned} \tag{A.24}$$

$$\begin{aligned} c_1 = l_3'\left(x_1\right) &= \frac{2x_1 - \left(x_1 + x_2\right)}{\delta x_{2,i=2}\left(\delta x_{2,i=1} + \delta x_{2,i=2}\right)} \\ &= -\frac{\delta x_{2,i=1}}{\delta x_{2,i=2}\left(dx_{2,i=1} + \delta x_{2,i=2}\right)} \end{aligned} \tag{A.25}$$

A.1.3 Backward Difference

The backward difference formulation is likewise found as shown in Figure A.3, where

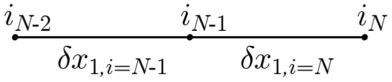

Figure A.3: First derivative backward differencing diagram setup.

$$\delta x_{1,i=N} = x_N - x_{N-1} \tag{A.26}$$

$$\delta x_{1,i=N-1} = x_{N-1} - x_{N-2} \tag{A.27}$$

and the expression for the derivative at x_N is written as

$$f'(x_N) = a_N f(x_{N-2}) + b_N f(x_{N-1}) + c_N f(x_N) \tag{A.28}$$

To solve for the coefficients a_N, b_N, and c_N, the three Lagrange basis polynomials, l_{N-2}, l_{N-1}, and l_N, are first derived for their respective three grid points located about grid point x_N.

$$\begin{aligned} l_{N-2} &= \frac{x - x_{N-1}}{x_{N-2} - x_{N-1}} \frac{x - x_N}{x_{N-2} - x_N} \\ &= \frac{x^2 - x\left(x_N + x_{N+1}\right) + x_N x_{N-1}}{\delta x_{1,i=N-1}\left(\delta x_{1,i=N-1} + \delta x_{1,i=N}\right)} \end{aligned} \tag{A.29}$$

$$\begin{aligned} l_{N-1} &= \frac{x - x_{N-2}}{x_{N-1} - x_{N-2}} \frac{x - x_N}{x_{N-1} - x_N} \\ &= -\frac{x^2 - x\left(x_{N-2} + x_N\right) + x_{N-2} x_N}{\delta x_{1,i=N-1} d x_{1,i=N}} \end{aligned} \tag{A.30}$$

$$\begin{aligned} l_N &= \frac{x - x_{N-2}}{x_N - x_{N-2}} \frac{x - x_{N-1}}{x_N - x_{N-1}} \\ &= \frac{x^2 - x\left(x_{N-2} + x_{N-1}\right) + x_{N-2} x_{N-1}}{\delta x_{1,i=N}\left(\delta x_{1,i=N} + \delta x_{1,i=N-1}\right)} \end{aligned} \tag{A.31}$$

Then, their derivatives are taken

$$l'_{N-2}(x) = \frac{2x - \left(x_N + x_{N-1}\right)}{\delta x_{1,i=N-1}\left(\delta x_{1,i=N-1} + \delta x_{1,i=N}\right)} \tag{A.32}$$

$$l'_{N-1}(x) = -\frac{2x - \left(x_{N-2} + x_N\right)}{\delta x_{1,i=N-1} \delta x_{1,i=N}} \tag{A.33}$$

$$l'_N(x) = \frac{2x - \left(x_{N-2} + x_{N-1}\right)}{\delta x_{1,i=N}\left(\delta x_{1,i=N} + \delta x_{1,i=N-1}\right)} \tag{A.34}$$

and evaluated at x_N.

$$\begin{aligned} a_N = l'_{N-2}\left(x_N\right) &= \frac{2x_N - \left(x_N + x_{N-1}\right)}{\delta x_{1,i=N-1}\left(\delta x_{1,i=N-1} + \delta x_{1,i=N}\right)} \\ &= \frac{\delta x_{1,i=N}}{\delta x_{1,i=N-1}\left(\delta x_{1,i=N-1} + \delta x_{1,i=N}\right)} \end{aligned} \tag{A.35}$$

$$\begin{aligned} b_N = l'_{N-1}\left(x_N\right) &= -\frac{2x_N - \left(x_{N-2} + x_N\right)}{\delta x_{1,i=N-1}\delta x_{1,i=N}} \\ &= -\frac{\delta x_{1,i=N} + \delta x_{1,i=N-1}}{\delta x_{1,i=N-1}\delta x_{1,i=N}} \end{aligned} \tag{A.36}$$

$$\begin{aligned} c_N = l'_{N}\left(x_N\right) &= \frac{2x_N - \left(x_{N-2} + x_{N-1}\right)}{\delta x_{1,i=N}\left(\delta x_{1,i=N} + \delta x_{1,i=N-1}\right)} \\ &= \frac{2\delta x_{1,i=N} + 2\delta x_{1,i=N-1}}{\delta x_{1,i=N}\left(\delta x_{1,i=N} + \delta x_{1,i=N-1}\right)} \end{aligned} \tag{A.37}$$

A.2 Second Derivatives

A.2.1 Central Difference

The approach used to procure the first derivative formulations also applies for the second derivatives. Beginning again with the central-differenced formulation, the expression for the derivative at x_N is written as

$$f''\left(x_i\right) \approx a_i f\left(x_{i-1}\right) + b_i f\left(x_i\right) + c_i f\left(x_{i+1}\right) \tag{A.38}$$

where the derivatives of Eqs. (A.11), (A.12), and (A.13) are given by

$$a_i = l''_{i-1}\left(x\right) = \frac{2}{\delta x_1\left(\delta x_1 + \delta x_2\right)} \tag{A.39}$$

$$b_i = l''_{i}\left(x\right) = -\frac{2}{\delta x_1 \delta x_2} \tag{A.40}$$

$$c_i = l''_{i+1}\left(x\right) = \frac{2}{\delta x_2\left(\delta x_1 + \delta x_2\right)} \tag{A.41}$$

A.2.2 Forward Difference

The forward differencing formula is derived in a similar fashion, with one exception. That is, a four point Lagrange polynomial will now be used instead of the previous three point Lagrange polynomials. This concept follows from noting that the outer and inner points receive equal weight, which will result in equivalent values for two adjacent points. In terms of accuracy, this means that using a three point Lagrange polynomial in this case would be only first order accurate. In keeping with the desire to maintain second order accuracy, the forward difference scheme is found using four grid points, as shown in Figure A.4, where

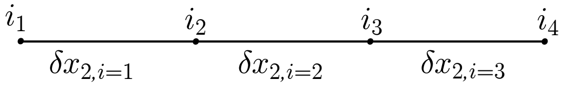

Figure A.4: Second derivative forward differencing diagram setup.

$$\delta x_{2,i=1} = x_2 - x_1 \tag{A.42}$$

$$\delta x_{2,i=2} = x_3 - x_2 \tag{A.43}$$

$$\delta x_{2,i=3} = x_4 - x_3 \tag{A.44}$$

and the expression for the derivative at x_1 is written as

$$f''\left(x_1\right) = a_1 f\left(x_1\right) + b_1 f\left(x_2\right) + c_1 f\left(x_3\right) + d_1 f\left(x_4\right) \tag{A.45}$$

To solve for the coefficients a_1, b_1, c_1, and d_1, the four Lagrange basis polynomials, l_1, l_2, l_3, and l_4, are first derived for their respective four grid points located about grid point x_1.

$$\begin{aligned} l_1 &= \frac{x - x_2}{x_1 - x_2} \frac{x - x_3}{x_1 - x_3} \frac{x - x_4}{x_1 - x_4} \\ &= -\frac{x^3 - x^2\left(x_2 + x_3 + x_4\right) + x\left(x_2 x_3 + x_2 x_4 + x_3 x_4\right) - x_2 x_3 x_4}{dx_{2,i=1}\left(dx_{2,i=1} + dx_{2,i=2}\right)\left(dx_{2,i=1} + dx_{2,i=2} + dx_{2,i=3}\right)} \end{aligned} \tag{A.46}$$

$$\begin{aligned} l_2 &= \frac{x-x_1}{x_2-x_1}\frac{x-x_3}{x_2-x_3}\frac{x-x_4}{x_2-x_4} \\ &= \frac{x^3-x^2\left(x_1+x_3+x_4\right)+x\left(x_1x_3+x_1x_4+x_3x_4\right)-x_1x_3x_4}{\delta x_{2,i=1}\delta x_{2,i=2}\left(\delta x_{2,i=2}+\delta x_{2,i=3}\right)} \end{aligned} \tag{A.47}$$

$$\begin{aligned} l_3 &= \frac{x-x_1}{x_3-x_1}\frac{x-x_2}{x_3-x_2}\frac{x-x_4}{x_3-x_4} \\ &= -\frac{x^3-x^2\left(x_1+x_2+x_4\right)+x\left(x_1x_2+x_1x_4+x_2x_4\right)-x_1x_2x_4}{\delta x_{2,i=2}\delta x_{2,i=3}\left(\delta x_{2,i=2}+\delta x_{2,i=1}\right)} \end{aligned} \tag{A.48}$$

$$\begin{aligned} l_4 &= \frac{x-x_1}{x_4-x_1}\frac{x-x_2}{x_4-x_2}\frac{x-x_3}{x_4-x_3} \\ &= \frac{x^3-x^2\left(x_1+x_2+x_3\right)+x\left(x_1x_2+x_1x_3+x_2x_3\right)-x_1x_2x_3}{\delta x_{2,i=3}\left(\delta x_{2,i=2}+\delta x_{2,i=3}\right)\left(\delta x_{2,i=1}+\delta x_{2,i=2}+\delta x_{2,i=3}\right)} \end{aligned} \tag{A.49}$$

Then, the first derivatives

$$l_1' = -\frac{3x^2-2x\left(x_2+x_3+x_4\right)+\left(x_2x_3+x_2x_4+x_3x_4\right)}{\delta x_{2,i=1}\left(\delta x_{2,i=1}+\delta x_{2,i=2}\right)\left(\delta x_{2,i=1}+\delta x_{2,i=2}+\delta x_{2,i=3}\right)} \tag{A.50}$$

$$l_2' = \frac{3x^2-2x\left(x_1+x_3+x_4\right)+\left(x_1x_3+x_1x_4+x_3x_4\right)}{\delta x_{2,i=1}\delta x_{2,i=2}\left(\delta x_{2,i=2}+\delta x_{2,i=3}\right)} \tag{A.51}$$

$$l_3' = -\frac{3x^2-2x\left(x_1+x_2+x_4\right)+\left(x_1x_2+x_1x_4+x_2x_4\right)}{\delta x_{2,i=2}\delta x_{2,i=3}\left(\delta x_{2,i=1}+\delta x_{2,i=2}\right)} \tag{A.52}$$

$$l_4' = \frac{3x^2-2x\left(x_1+x_2+x_3\right)+\left(x_1x_2+x_1x_3+x_2x_3\right)}{\delta x_{2,i=3}\left(\delta x_{2,i=2}+\delta x_{2,i=3}\right)\left(\delta x_{2,i=1}+\delta x_{2,i=2}+\delta x_{2,i=3}\right)} \tag{A.53}$$

and second derivatives are found:

$$l_1'' = -\frac{6x-2\left(x_2+x_3+x_4\right)}{\delta x_{2,i=1}\left(\delta x_{2,i=1}+\delta x_{2,i=2}\right)\left(\delta x_{2,i=1}+\delta x_{2,i=2}+\delta x_{2,i=3}\right)} \tag{A.54}$$

$$l_2'' = \frac{6x-2\left(x_1+x_3+x_4\right)}{\delta x_{2,i=1}\delta x_{2,i=2}\left(\delta x_{2,i=2}+\delta x_{2,i=3}\right)} \tag{A.55}$$

$$l_3'' = -\frac{6x-2\left(x_1+x_2+x_4\right)}{\delta x_{2,i=2}\delta x_{2,i=3}\left(\delta x_{2,i=1}+\delta x_{2,i=2}\right)} \tag{A.56}$$

$$l_4'' = \frac{6x-2\left(x_1+x_2+x_3\right)}{\delta x_{2,i=3}\left(\delta x_{2,i=2}+\delta x_{2,i=3}\right)\left(\delta x_{2,i=1}+\delta x_{2,i=2}+\delta x_{2,i=3}\right)} \tag{A.57}$$

Lastly, the Lagrange polynomials are evaluated at x_1 to give,

$$\begin{aligned} a_1 = l_1''(x_1) &= -\frac{6x_1 - 2(x_2 + x_3 + x_4)}{\delta x_{2,i=1}(\delta x_{2,i=1} + \delta x_{2,i=2})(\delta x_{2,i=1} + \delta x_{2,i=2} + \delta x_{2,i=3})} \\ &= -\frac{6\delta x_{2,i=1} + 4\delta x_{2,i=2} + 2\delta x_{2,i=3}}{\delta x_{2,i=1}(\delta x_{2,i=1} + \delta x_{2,i=2})(\delta x_{2,i=1} + \delta x_{2,i=2} + \delta x_{2,i=3})} \end{aligned} \tag{A.58}$$

$$\begin{aligned} b_1 = l_2''(x_1) &= \frac{6x_1 - 2(x_1 + x_3 + x_4)}{\delta x_{2,i=1}\delta x_{2,i=2}(\delta x_{2,i=2} + \delta x_{2,i=3})} \\ &= -\frac{4\delta x_{2,i=1} + 4\delta x_{2,i=2} + 2\delta x_{2,i=3}}{\delta x_{2,i=1}\delta x_{2,i=2}(\delta x_{2,i=2} + \delta x_{2,i=3})} \end{aligned} \tag{A.59}$$

$$\begin{aligned} c_1 = l_3''(x_1) &= -\frac{6x_1 - 2(x_1 + x_2 + x_4)}{\delta x_{2,i=2}\delta x_{2,i=3}(\delta x_{2,i=1} + \delta x_{2,i=2})} \\ &= -\frac{4\delta x_{2,i=1} + 2\delta x_{2,i=2} + 2\delta x_{2,i=3}}{\delta x_{2,i=2}\delta x_{2,i=3}(\delta x_{2,i=1} + \delta x_{2,i=2})} \end{aligned} \tag{A.60}$$

$$\begin{aligned} d_1 = l_4''(x_1) &= \frac{6x_1 - 2(x_1 + x_2 + x_3)}{\delta x_{2,i=3}(\delta x_{2,i=2} + \delta x_{2,i=3})(\delta x_{2,i=1} + \delta x_{2,i=2} + \delta x_{2,i=3})} \\ &= -\frac{4\delta x_{2,i=1} + 2\delta x_{2,i=2}}{\delta x_{2,i=1}(\delta x_{2,i=1} + \delta x_{2,i=2})(\delta x_{2,i=1} + \delta x_{2,i=2} + \delta x_{2,i=3})} \end{aligned} \tag{A.61}$$

A.2.3 Backward Difference

The backward difference formulation is determined in a similar fashion, as shown in Figure A.5,

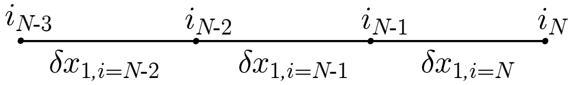

Figure A.5: Second derivative backward differencing diagram setup.

where

$$\delta x_{1,i=N} = x_N - x_{N-1} \tag{A.62}$$

$$\delta x_{1,i=N-1} = x_{N-1} - x_{N-2} \tag{A.63}$$

$$\delta x_{1,i=N-2} = x_{N-2} - x_{N-3} \tag{A.64}$$

define the spacing between the grid points.

$$f''_N\left(x_N\right) = a_N f\left(x_{N-3}\right) + b_N f\left(x_{N-2}\right) + c_N f\left(x_{N-1}\right) + d_N f\left(x_N\right) \tag{A.65}$$

To solve for the coefficients a_N, b_N, c_N, and d_N, the four Lagrange basis polynomials, l_{N-3}, l_{N-2}, l_{N-1}, and l_N, are first derived for their respective four grid points located about grid point x_1.

$$\begin{aligned} l_{N-3} &= \frac{x - x_{N-2}}{x_{N-3} - x_{N-2}} \frac{x - x_{N-1}}{x_{N-3} - x_{N-1}} \frac{x - x_N}{x_{N-3} - x_N} \\ &= \frac{\begin{array}{c} x^3 - x^2\left(x_N + x_{N-1} + x_{N-2}\right) \\ +x\left(x_N x_{N-1} + x_N x_{N-2} + x_{N-1} x_{N-2}\right) - x_N x_{N-1} x_{N-2} \end{array}}{\begin{array}{c} \delta x_{1,i=N-2}\left(\delta x_{1,i=N-1} + \delta x_{1,i=N-2}\right) \\ \cdot\left(\delta x_{1,i=N} + \delta x_{1,i=N-1} + \delta x_{1,i=N-2}\right) \end{array}} \end{aligned} \tag{A.66}$$

$$\begin{aligned} l_{N-2} &= \frac{x - x_{N-3}}{x_{N-2} - x_{N-3}} \frac{x - x_{N-1}}{x_{N-2} - x_{N-1}} \frac{x - x_N}{x_{N-2} - x_N} \\ &= \frac{\begin{array}{c} x^3 - x^2\left(x_N + x_{N-1} + x_{N-3}\right) \\ +x\left(x_N x_{N-1} + x_N x_{N-3} + x_{N-2} x_{N-3}\right) - x_N x_{N-1} x_{N-3} \end{array}}{\delta x_{1,i=N-1} \delta x_{1,i=N-2}\left(\delta x_{1,i=N-1} + \delta x_{1,i=N}\right)} \end{aligned} \tag{A.67}$$

$$\begin{aligned} l_{N-1} &= \frac{x - x_{N-3}}{x_{N-1} - x_{N-3}} \frac{x - x_{N-2}}{x_{N-1} - x_{N-2}} \frac{x - x_N}{x_{N-1} - x_N} \\ &= \frac{\begin{array}{c} x^3 - x^2\left(x_N + x_{N-2} + x_{N-3}\right) \\ +x\left(x_N x_{N-2} + x_N x_{N-3} + x_{N-2} x_{N-3}\right) - x_N x_{N-2} x_{N-3} \end{array}}{\delta x_{1,i=N} \delta x_{1,i=N-1}\left(\delta x_{1,i=N-1} + \delta x_{1,i=N-2}\right)} \end{aligned} \tag{A.68}$$

$$\begin{aligned} l_N &= \frac{x - x_{N-3}}{x_N - x_{N-3}} \frac{x - x_{N-2}}{x_N - x_{N-2}} \frac{x - x_{N-1}}{x_N - x_{N-1}} \\ &= \frac{\begin{array}{c} x^3 - x^2\left(x_{N-1} + x_{N-2} + x_{N-3}\right) \\ +x\left(x_{N-1} x_{N-2} + x_{N-1} x_{N-3} + x_{N-2} x_{N-3}\right) - x_{N-1} x_{N-2} x_{N-3} \end{array}}{\delta x_{1,i=N}\left(\delta x_{1,i=N} + \delta x_{1,i=N-1}\right)\left(\delta x_{1,i=N} + \delta x_{1,i=N-1} + \delta x_{1,i=N-2}\right)} \end{aligned} \tag{A.69}$$

Then, their derivatives are taken

$$l'_{N-3} = \frac{\begin{array}{c} 3x^2 - 2x\left(x_N + x_{N-1} + x_{N-2}\right) \\ +\left(x_N x_{N-1} + x_N x_{N-2} + x_{N-1} x_{N-2}\right) \end{array}}{\begin{array}{c} \delta x_{1,i=N-2}\left(\delta x_{1,i=N-1} + \delta x_{1,i=N-2}\right) \\ \cdot\left(\delta x_{1,i=N} + \delta x_{1,i=N-1} + \delta x_{1,i=N-2}\right) \end{array}} \tag{A.70}$$

$$l'_{N-2} = \frac{\begin{gathered}3x^2 - 2x\left(x_N + x_{N-1} + x_{N-3}\right) \\ + \left(x_N x_{N-1} + x_N x_{N-3} + x_{N-2} x_{N-3}\right)\end{gathered}}{\delta x_{1,i=N-1} \delta x_{1,i=N-2} \left(\delta x_{1,i=N-1} + \delta x_{1,i=N}\right)} \tag{A.71}$$

$$l'_{N-1} = \frac{\begin{gathered}3x^2 - 2x\left(x_N + x_{N-2} + x_{N-3}\right) \\ + \left(x_N x_{N-2} + x_N x_{N-3} + x_{N-2} x_{N-3}\right)\end{gathered}}{\delta x_{1,i=N} \delta x_{1,i=N-1} \left(\delta x_{1,i=N-1} + \delta x_{1,i=N-2}\right)} \tag{A.72}$$

$$l'_{N} = \frac{\begin{gathered}3x^2 - 2x\left(x_{N-1} + x_{N-2} + x_{N-3}\right) \\ + \left(x_{N-1} x_{N-2} + x_{N-1} x_{N-3} + x_{N-2} x_{N-3}\right)\end{gathered}}{\begin{gathered}\delta x_{1,i=N} \left(\delta x_{1,i=N} + \delta x_{1,i=N-1}\right) \\ \cdot \left(\delta x_{1,i=N} + \delta x_{1,i=N-1} + \delta x_{1,i=N-2}\right)\end{gathered}} \tag{A.73}$$

and taken again.

$$l''_{N-3} = -\frac{6x - 2\left(x_N + x_{N-1} + x_{N-2}\right)}{\begin{gathered}\delta x_{1,i=N-2} \left(\delta x_{1,i=N-1} + \delta x_{1,i=N-2}\right) \\ \cdot \left(\delta x_{1,i=N} + \delta x_{1,i=N-1} + \delta x_{1,i=N-2}\right)\end{gathered}} \tag{A.74}$$

$$l''_{N-2} = \frac{6x - 2\left(x_N + x_{N-1} + x_{N-3}\right)}{\delta x_{1,i=N-1} \delta x_{1,i=N-2} \left(\delta x_{1,i=N-1} + \delta x_{1,i=N}\right)} \tag{A.75}$$

$$l''_{N-1} = \frac{6x - 2\left(x_N + x_{N-2} + x_{N-3}\right)}{\delta x_{1,i=N} \delta x_{1,i=N-1} \left(\delta x_{1,i=N-1} + \delta x_{1,i=N-2}\right)} \tag{A.76}$$

$$l''_{N} = \frac{6x - 2\left(x_{N-1} + x_{N-2} + x_{N-3}\right)}{\begin{gathered}\delta x_{1,i=N} \left(\delta x_{1,i=N} + \delta x_{1,i=N-1}\right) \\ \cdot \left(\delta x_{1,i=N} + \delta x_{1,i=N-1} + \delta x_{1,i=N-2}\right)\end{gathered}} \tag{A.77}$$

Lastly, the Lagrange polynomials are evaluted at x_N.

$$\begin{aligned} a_N = l''_{N-3}\left(x_N\right) &= -\frac{6x_N - 2\left(x_N + x_{N-1} + x_{N-2}\right)}{\begin{gathered}\delta x_{1,i=N-2} \left(\delta x_{1,i=N-1} + \delta x_{1,i=N-2}\right) \\ \cdot \left(\delta x_{1,i=N} + \delta x_{1,i=N-1} + \delta x_{1,i=N-2}\right)\end{gathered}} \\ &= -\frac{4\delta x_{1,i=N} + 2\delta x_{1,i=N-1}}{\begin{gathered}\delta x_{1,i=N-2} \left(\delta x_{1,i=N-1} + \delta x_{1,i=N-2}\right) \\ \cdot \left(\delta x_{1,i=N} + \delta x_{1,i=N-1} + \delta x_{1,i=N-2}\right)\end{gathered}} \end{aligned} \tag{A.78}$$

$$\begin{aligned} b_N = l''_{N-2}\left(x_N\right) &= \frac{6x_N - 2\left(x_N + x_{N-1} + x_{N-3}\right)}{\delta x_{1,i=N-1} \delta x_{1,i=N-2} \left(\delta x_{1,i=N-1} + \delta x_{1,i=N}\right)} \\ &= \frac{4\delta x_{1,i=N} + 2\delta x_{1,i=N-1} + 2\delta x_{1,i=N-2}}{\delta x_{1,i=N-1} \delta x_{1,i=N-2} \left(\delta x_{1,i=N-1} + \delta x_{1,i=N}\right)} \end{aligned} \tag{A.79}$$

$$
\begin{aligned}
c_N = l''_{N-1}\left(x_N\right) &= -\frac{6x_N - \left(x_N + x_{N-2} + x_{N-3}\right)}{\delta x_{1,i=N}\delta x_{1,i=N-1}\left(\delta x_{1,i=N-1} + \delta x_{1,i=N-2}\right)} \\
&= -\frac{4\delta x_{1,i=N} + 4\delta x_{1,i=N-1} + 2\delta x_{1,i=N-2}}{\delta x_{1,i=N}\delta x_{1,i=N-1}\left(\delta x_{1,i=N-1} + \delta x_{1,i=N-2}\right)}
\end{aligned}
\tag{A.80}
$$

$$
\begin{aligned}
d_N = l''_{N}\left(x_N\right) &= \frac{6x_N - 2\left(x_{N-1} + x_{N-2} + x_{N-3}\right)}{\begin{array}{c}\delta x_{1,i=N}\left(\delta x_{1,i=N} + \delta x_{1,i=N-1}\right) \\ \cdot\left(\delta x_{1,i=N} + \delta x_{1,i=N-1} + \delta x_{1,i=N-2}\right)\end{array}} \\
&= \frac{6\delta x_{1,i=N} + 4\delta x_{1,i=N-1} + 2\delta x_{1,i=N-2}}{\begin{array}{c}\delta x_{1,i=N}\left(\delta x_{1,i=N} + \delta x_{1,i=N-1}\right) \\ \cdot\left(\delta x_{1,i=N} + \delta x_{1,i=N-1} + \delta x_{1,i=N-2}\right)\end{array}}
\end{aligned}
\tag{A.81}
$$

Appendix B

Curvilinear Gridding Derivation

In order to move beyond rectangular geometric meshing, a straightforward approach to deriving first and second derivative operator matrices in terms of the (x, y) components of an (x, y) coordinate system from curvilinear coordinates (r, s) is shown below. Figure B.1 shows the central concept of this derivation by looking at an example grid section set in curvilinear coordinates.

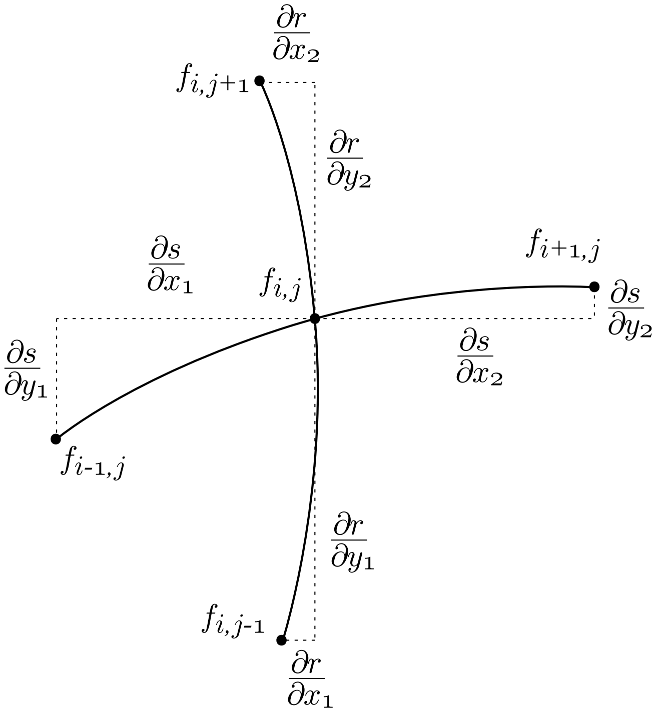

Figure B.1: Curvilinear diagram setup.

To begin, the distances between the curvilinear grid points are calculated, where ∂s is the distance between two adjacent grid points in the s-direction

$$\partial s = \sqrt{\partial s_x^2 + \partial s_y^2} \tag{B.1}$$

and ∂r is the distance between two adjacent grid points in the r-direction.

$$\partial r = \sqrt{\partial r_x^2 + \partial r_y^2} \tag{B.2}$$

The derivatives with respect to r and s are then expanded through the chain rule.

$$\frac{\partial f}{\partial s} = \frac{\partial f}{\partial x}\frac{\partial x}{\partial s} + \frac{\partial f}{\partial y}\frac{\partial y}{\partial s} \tag{B.3}$$

$$\frac{\partial f}{\partial r} = \frac{\partial f}{\partial x}\frac{\partial x}{\partial r} + \frac{\partial f}{\partial y}\frac{\partial y}{\partial r} \tag{B.4}$$

B.1 First Derivatives

To evaluate the $\frac{\partial f}{\partial x}$ operator, we take,

$$\frac{\partial f}{\partial y} = \frac{\frac{\partial f}{\partial s} - \frac{\partial x}{\partial s}\frac{\partial f}{\partial x}}{\frac{\partial y}{\partial s}} \tag{B.5}$$

$$\frac{\partial f}{\partial y} = \frac{\frac{\partial f}{\partial r} - \frac{\partial x}{\partial r}\frac{\partial f}{\partial x}}{\frac{\partial y}{\partial r}} \tag{B.6}$$

$$\frac{\partial y}{\partial s}\left(\frac{\partial f}{\partial r} - \frac{\partial x}{\partial r}\frac{\partial f}{\partial x}\right) = \frac{\partial y}{\partial r}\left(\frac{\partial f}{\partial s} - \frac{\partial x}{\partial s}\frac{\partial f}{\partial x}\right) \tag{B.7}$$

$$\frac{\partial f}{\partial x} = \frac{\frac{\partial y}{\partial r}\frac{\partial f}{\partial s} - \frac{\partial y}{\partial s}\frac{\partial f}{\partial r}}{\frac{\partial y}{\partial r}\frac{\partial x}{\partial s} - \frac{\partial y}{\partial s}\frac{\partial x}{\partial r}} \tag{B.8}$$

Likewise, the $\frac{\partial f}{\partial y}$ operator is found using

$$\frac{\partial f}{\partial x} = \frac{\frac{\partial f}{\partial s} - \frac{\partial y}{\partial s}\frac{\partial f}{\partial y}}{\frac{\partial x}{\partial s}} \tag{B.9}$$

$$\frac{\partial f}{\partial x} = \frac{\dfrac{\partial f}{\partial r} - \dfrac{\partial y}{\partial r}\dfrac{\partial f}{\partial y}}{\dfrac{\partial x}{\partial r}} \tag{B.10}$$

$$\frac{\partial x}{\partial s}\left(\frac{\partial f}{\partial r} - \frac{\partial y}{\partial r}\frac{\partial f}{\partial y}\right) = \frac{\partial x}{\partial r}\left(\frac{\partial f}{\partial s} - \frac{\partial y}{\partial s}\frac{\partial f}{\partial y}\right) \tag{B.11}$$

and so,

$$\frac{\partial f}{\partial y} = \frac{\dfrac{\partial x}{\partial r}\dfrac{\partial f}{\partial s} - \dfrac{\partial x}{\partial s}\dfrac{\partial f}{\partial r}}{\dfrac{\partial x}{\partial r}\dfrac{\partial y}{\partial s} - \dfrac{\partial x}{\partial s}\dfrac{\partial y}{\partial r}} \tag{B.12}$$

B.2 Second Derivatives

The second derivative terms are obtained using a similar manipulation,

$$\frac{\partial}{\partial s}\left(\frac{\partial f}{\partial s}\right) = \frac{\partial}{\partial s}\left(\frac{\partial x}{\partial s}\frac{\partial f}{\partial x} + \frac{\partial y}{\partial s}\frac{\partial f}{\partial y}\right) \tag{B.13}$$

where the $\dfrac{\partial}{\partial s}$ term is expanded through the chain rule,

$$\frac{\partial}{\partial s}\left(\frac{\partial f}{\partial s}\right) = \left(\frac{\partial x}{\partial s}\frac{\partial}{\partial x} + \frac{\partial y}{\partial s}\frac{\partial}{\partial y}\right)\left(\frac{\partial x}{\partial s}\frac{\partial f}{\partial x} + \frac{\partial y}{\partial s}\frac{\partial f}{\partial y}\right) \tag{B.14}$$

$$\frac{\partial^2 f}{\partial s^2} = \frac{\partial}{\partial x}\frac{\partial x}{\partial s}\frac{\partial f}{\partial x}\frac{\partial x}{\partial s} + \frac{\partial}{\partial y}\frac{\partial y}{\partial s}\frac{\partial f}{\partial x}\frac{\partial x}{\partial s} + \frac{\partial}{\partial y}\frac{\partial y}{\partial s}\frac{\partial f}{\partial y}\frac{\partial y}{\partial s} + \frac{\partial}{\partial y}\frac{\partial y}{\partial s}\frac{\partial f}{\partial y}\frac{\partial y}{\partial s} \tag{B.15}$$

$$\begin{aligned}\frac{\partial^2 f}{\partial s^2} = {} & \frac{\partial x}{\partial s}\left(\frac{\partial}{\partial x}\frac{\partial f}{\partial x}\frac{\partial x}{\partial s} + \frac{\partial}{\partial y}\frac{\partial y}{\partial s}\frac{\partial f}{\partial x}\right) \\ & + \frac{\partial y}{\partial s}\left(\frac{\partial}{\partial y}\frac{\partial f}{\partial y}\frac{\partial y}{\partial s} + \frac{\partial}{\partial y}\frac{\partial y}{\partial s}\frac{\partial f}{\partial y}\right)\end{aligned} \tag{B.16}$$

The chain rule is used to expand the derivatives,

$$\begin{aligned}\frac{\partial^2 f}{\partial s^2} = {} & \frac{\partial x}{\partial s}\left(\frac{\partial x}{\partial s}\frac{\partial^2 f}{\partial x \partial s} + \frac{\partial f}{\partial x}\frac{\partial^2 x}{\partial x \partial s} + \frac{\partial y}{\partial s}\frac{\partial^2 f}{\partial x \partial y} + \frac{\partial f}{\partial y}\frac{\partial^2 f}{\partial x \partial s}\right) \\ & + \frac{\partial y}{\partial s}\left(\frac{\partial x}{\partial s}\frac{\partial^2 f}{\partial y \partial x} + \frac{\partial f}{\partial x}\frac{\partial^2 x}{\partial y \partial s} + \frac{\partial y}{\partial s}\frac{\partial^2 f}{\partial y^2} + \frac{\partial f}{\partial y}\frac{\partial^2 y}{\partial y \partial s}\right)\end{aligned} \tag{B.17}$$

Then, $\frac{\partial^2 f}{\partial s^2}$ can be found to be

$$\begin{aligned}\frac{\partial^2 f}{\partial s^2} = \left(\frac{\partial x}{\partial s}\right)^2 \frac{\partial^2 f}{\partial x^2} + \left(\frac{\partial x}{\partial s}\frac{\partial^2 x}{\partial x \partial s} + \frac{\partial y}{\partial s}\frac{\partial^2 x}{\partial y \partial s}\right)\frac{\partial f}{\partial x} \\ +2\frac{\partial x}{\partial s}\frac{\partial y}{\partial s}\frac{\partial^2 f}{\partial x \partial y} + \left(\frac{\partial x}{\partial s}\frac{\partial^2 y}{\partial x \partial s} + \frac{\partial y}{\partial s}\frac{\partial^2 y}{\partial y \partial s}\right)\frac{\partial f}{\partial y} + \left(\frac{\partial y}{\partial s}\right)^2 \frac{\partial^2 f}{\partial y^2}\end{aligned} \tag{B.18}$$

In a similar fashion, $\frac{\partial^2 f}{\partial r^2}$ can be solved for

$$\frac{\partial}{\partial r}\left(\frac{\partial f}{\partial r}\right) = \frac{\partial}{\partial r}\left(\frac{\partial x}{\partial r}\frac{\partial f}{\partial x} + \frac{\partial y}{\partial r}\frac{\partial f}{\partial y}\right) \tag{B.19}$$

where the $\frac{\partial}{\partial r}$ term is expanded via the chain rule

$$\frac{\partial}{\partial r}\left(\frac{\partial f}{\partial r}\right) = \left(\frac{\partial x}{\partial r}\frac{\partial}{\partial x} + \frac{\partial y}{\partial r}\frac{\partial}{\partial y}\right)\left(\frac{\partial x}{\partial r}\frac{\partial f}{\partial x} + \frac{\partial y}{\partial r}\frac{\partial f}{\partial y}\right) \tag{B.20}$$

$$\frac{\partial^2 f}{\partial r^2} = \frac{\partial}{\partial x}\frac{\partial x}{\partial r}\frac{\partial f}{\partial x}\frac{\partial x}{\partial r} + \frac{\partial}{\partial y}\frac{\partial y}{\partial r}\frac{\partial f}{\partial x}\frac{\partial x}{\partial r} + \frac{\partial}{\partial y}\frac{\partial y}{\partial r}\frac{\partial f}{\partial y}\frac{\partial y}{\partial r} + \frac{\partial}{\partial y}\frac{\partial y}{\partial r}\frac{\partial f}{\partial y}\frac{\partial y}{\partial r} \tag{B.21}$$

$$\begin{aligned}\frac{\partial^2 f}{\partial r^2} = \frac{\partial x}{\partial r}\left(\frac{\partial}{\partial x}\frac{\partial f}{\partial x}\frac{\partial x}{\partial r} + \frac{\partial}{\partial y}\frac{\partial y}{\partial r}\frac{\partial f}{\partial x}\right) \\ +\frac{\partial y}{\partial r}\left(\frac{\partial}{\partial y}\frac{\partial f}{\partial y}\frac{\partial y}{\partial r} + \frac{\partial}{\partial y}\frac{\partial y}{\partial r}\frac{\partial f}{\partial y}\right)\end{aligned} \tag{B.22}$$

The chain rule is used to expand the derivatives,

$$\begin{aligned}\frac{\partial^2 f}{\partial r^2} = \frac{\partial x}{\partial r}\left(\frac{\partial x}{\partial r}\frac{\partial^2 f}{\partial x \partial r} + \frac{\partial f}{\partial x}\frac{\partial^2 x}{\partial x \partial r} + \frac{\partial y}{\partial r}\frac{\partial^2 f}{\partial x \partial y} + \frac{\partial f}{\partial y}\frac{\partial^2 f}{\partial x \partial r}\right) \\ +\frac{\partial y}{\partial r}\left(\frac{\partial x}{\partial r}\frac{\partial^2 f}{\partial y \partial x} + \frac{\partial f}{\partial x}\frac{\partial^2 x}{\partial y \partial r} + \frac{\partial y}{\partial r}\frac{\partial^2 f}{\partial y^2} + \frac{\partial f}{\partial y}\frac{\partial^2 y}{\partial y \partial r}\right)\end{aligned} \tag{B.23}$$

Then, $\dfrac{\partial^2 f}{\partial r^2}$ can be found and expressed as

$$\begin{aligned}\frac{\partial^2 f}{\partial r^2} = {} & \left(\frac{\partial x}{\partial r}\right)^2 \frac{\partial^2 f}{\partial x^2} + \left(\frac{\partial x}{\partial r}\frac{\partial^2 x}{\partial x \partial r} + \frac{\partial y}{\partial r}\frac{\partial^2 x}{\partial y \partial r}\right)\frac{\partial f}{\partial x} \\ & + 2\frac{\partial x}{\partial r}\frac{\partial y}{\partial r}\frac{\partial^2 f}{\partial x \partial y} + \left(\frac{\partial x}{\partial r}\frac{\partial^2 y}{\partial x \partial r} + \frac{\partial y}{\partial r}\frac{\partial^2 y}{\partial y \partial r}\right)\frac{\partial f}{\partial y} + \left(\frac{\partial y}{\partial r}\right)^2 \frac{\partial^2 f}{\partial y^2}\end{aligned} \tag{B.24}$$

Now, to solve for $\dfrac{\partial^2 f}{\partial x^2}$, Eqs. (B.18) and (B.24) are solved for $\dfrac{\partial^2 f}{\partial y^2}$

$$\frac{\partial^2 f}{\partial y^2} = \frac{\begin{array}{c}\dfrac{\partial^2 f}{\partial s^2} - \left(\dfrac{\partial x}{\partial s}\right)^2 \dfrac{\partial^2 f}{\partial x^2} - \left(\dfrac{\partial x}{\partial s}\dfrac{\partial^2 x}{\partial x \partial s} + \dfrac{\partial y}{\partial s}\dfrac{\partial^2 x}{\partial y \partial s}\right)\dfrac{\partial f}{\partial x} \\ -2\dfrac{\partial x}{\partial s}\dfrac{\partial y}{\partial s}\dfrac{\partial^2 f}{\partial x \partial y} - \left(\dfrac{\partial x}{\partial s}\dfrac{\partial^2 y}{\partial x \partial s} + \dfrac{\partial y}{\partial s}\dfrac{\partial^2 y}{\partial y \partial s}\right)\dfrac{\partial f}{\partial y}\end{array}}{\left(\dfrac{\partial y}{\partial s}\right)^2} \tag{B.25}$$

$$\frac{\partial^2 f}{\partial y^2} = \frac{\begin{array}{c}\dfrac{\partial^2 f}{\partial r^2} - \left(\dfrac{\partial x}{\partial r}\right)^2 \dfrac{\partial^2 f}{\partial x^2} - \left(\dfrac{\partial x}{\partial r}\dfrac{\partial^2 x}{\partial x \partial r} + \dfrac{\partial y}{\partial r}\dfrac{\partial^2 x}{\partial y \partial r}\right)\dfrac{\partial f}{\partial x} \\ -2\dfrac{\partial x}{\partial r}\dfrac{\partial y}{\partial r}\dfrac{\partial^2 f}{\partial x \partial y} - \left(\dfrac{\partial x}{\partial r}\dfrac{\partial^2 y}{\partial x \partial r} + \dfrac{\partial y}{\partial r}\dfrac{\partial^2 y}{\partial y \partial r}\right)\dfrac{\partial f}{\partial y}\end{array}}{\left(\dfrac{\partial y}{\partial r}\right)^2} \tag{B.26}$$

By equating Eq. (B.25) and Eq. (B.26), $\dfrac{\partial^2 f}{\partial x^2}$ can be solved for

$$\frac{\partial^2 f}{\partial x^2} = \frac{\left(\dfrac{\partial y}{\partial s}\right)^2 \dfrac{\partial^2 f}{\partial r^2} + a + b + c - \left(\dfrac{\partial y}{\partial r}\right)^2 \dfrac{\partial^2 f}{\partial s^2}}{\left(\dfrac{\partial y}{\partial s}\right)^2 \left(\dfrac{\partial x}{\partial r}\right)^2 - \left(\dfrac{\partial y}{\partial r}\right)^2 \left(\dfrac{\partial x}{\partial s}\right)^2} \tag{B.27}$$

where,

$$a = \left[\left(\frac{\partial y}{\partial r}\right)^2 \left(\frac{\partial x}{\partial s}\frac{\partial^2 x}{\partial x \partial s} + \frac{\partial y}{\partial s}\frac{\partial^2 x}{\partial y \partial s}\right) - \left(\frac{\partial y}{\partial s}\right)^2 \left(\frac{\partial x}{\partial r}\frac{\partial^2 x}{\partial x \partial r} + \frac{\partial y}{\partial r}\frac{\partial^2 x}{\partial y \partial r}\right)\right]\frac{\partial f}{\partial x} \tag{B.28}$$

$$b = 2\left[\left(\frac{\partial y}{\partial r}\right)^2 \frac{\partial x}{\partial s}\frac{\partial y}{\partial s} - \left(\frac{\partial y}{\partial s}\right)^2 \frac{\partial x}{\partial r}\frac{\partial y}{\partial r}\right]\frac{\partial^2 f}{\partial x \partial y} \tag{B.29}$$

$$c = \left[\left(\frac{\partial y}{\partial r}\right)^2 \left(\frac{\partial x}{\partial s}\frac{\partial^2 y}{\partial x \partial s} + \frac{\partial y}{\partial s}\frac{\partial^2 y}{\partial y \partial s}\right) - \left(\frac{\partial y}{\partial s}\right)^2 \left(\frac{\partial x}{\partial r}\frac{\partial^2 x}{\partial x \partial r} + \frac{\partial y}{\partial r}\frac{\partial^2 y}{\partial y \partial r}\right)\right]\frac{\partial f}{\partial y} \tag{B.30}$$

Likewise, $\frac{\partial^2 f}{\partial y^2}$ can be found using

$$\frac{\partial^2 f}{\partial x^2} = \frac{\begin{array}{c}\frac{\partial^2 f}{\partial s^2} - \left(\frac{\partial y}{\partial s}\right)^2 \frac{\partial^2 f}{\partial y^2} - \left(\frac{\partial x}{\partial s}\frac{\partial^2 x}{\partial x \partial s} + \frac{\partial y}{\partial s}\frac{\partial^2 x}{\partial y \partial s}\right)\frac{\partial f}{\partial x} \\ -2\frac{\partial x}{\partial s}\frac{\partial y}{\partial s}\frac{\partial^2 f}{\partial x \partial y} - \left(\frac{\partial x}{\partial s}\frac{\partial^2 y}{\partial x \partial s} + \frac{\partial y}{\partial s}\frac{\partial^2 y}{\partial y \partial s}\right)\frac{\partial f}{\partial y}\end{array}}{\left(\frac{\partial x}{\partial s}\right)^2} \tag{B.31}$$

$$\frac{\partial^2 f}{\partial x^2} = \frac{\begin{array}{c}\frac{\partial^2 f}{\partial r^2} - \left(\frac{\partial y}{\partial r}\right)^2 \frac{\partial^2 f}{\partial y^2} - \left(\frac{\partial x}{\partial r}\frac{\partial^2 x}{\partial x \partial r} + \frac{\partial y}{\partial r}\frac{\partial^2 x}{\partial y \partial r}\right)\frac{\partial f}{\partial x} \\ -2\frac{\partial x}{\partial r}\frac{\partial y}{\partial r}\frac{\partial^2 f}{\partial x \partial y} - \left(\frac{\partial x}{\partial r}\frac{\partial^2 y}{\partial x \partial r} + \frac{\partial y}{\partial r}\frac{\partial^2 y}{\partial y \partial r}\right)\frac{\partial f}{\partial y}\end{array}}{\left(\frac{\partial x}{\partial r}\right)^2} \tag{B.32}$$

By equating Eq. (B.31) and Eq. (B.32), $\frac{\partial^2 f}{\partial y^2}$ can be found.

$$\frac{\partial^2 f}{\partial y^2} = \frac{\left(\frac{\partial x}{\partial s}\right)^2 \frac{\partial^2 f}{\partial r^2} + d + e + f - \left(\frac{\partial x}{\partial r}\right)^2 \frac{\partial^2 f}{\partial s^2}}{\left(\frac{\partial x}{\partial s}\right)^2 \left(\frac{\partial y}{\partial r}\right)^2 - \left(\frac{\partial x}{\partial r}\right)^2 \left(\frac{\partial y}{\partial s}\right)^2} \tag{B.33}$$

where,

$$d = \left[\left(\frac{\partial x}{\partial r}\right)^2 \left(\frac{\partial x}{\partial s}\frac{\partial^2 x}{\partial x \partial s} + \frac{\partial y}{\partial s}\frac{\partial^2 x}{\partial y \partial s}\right) - \left(\frac{\partial x}{\partial s}\right)^2 \left(\frac{\partial x}{\partial r}\frac{\partial^2 x}{\partial x \partial r} + \frac{\partial y}{\partial r}\frac{\partial^2 x}{\partial y \partial r}\right)\right]\frac{\partial f}{\partial x} \tag{B.34}$$

$$e = 2\left[\left(\frac{\partial x}{\partial r}\right)^2 \frac{\partial x}{\partial s}\frac{\partial y}{\partial s} - \left(\frac{\partial x}{\partial s}\right)^2 \frac{\partial x}{\partial r}\frac{\partial y}{\partial r}\right]\frac{\partial^2 f}{\partial x \partial y} \tag{B.35}$$

$$f = \left[\left(\frac{\partial x}{\partial r} \right)^2 \left(\frac{\partial x}{\partial s} \frac{\partial^2 y}{\partial x \partial s} + \frac{\partial y}{\partial s} \frac{\partial^2 y}{\partial y \partial s} \right) - \left(\frac{\partial x}{\partial s} \right)^2 \left(\frac{\partial x}{\partial r} \frac{\partial^2 x}{\partial x \partial r} + \frac{\partial y}{\partial r} \frac{\partial^2 y}{\partial y \partial r} \right) \right] \frac{\partial f}{\partial y} \tag{B.36}$$

Appendix C

Convected Acoustic Wave Equation Derivation

Though fundamental to our understanding of acoustics and wave propagation, the classical wave equation

$$a_0^{-2}\frac{\partial^2\varphi}{\partial t^2} - \nabla^2\varphi = 0 \tag{C.1}$$

can only be utilized in stationary, homentropic mediums. However, in many cases, mean flow effects can play a significant role in altering both the mode shapes and frequencies of the acoustics in a given medium. Thus, this classical approach must be modified to incorporate the mean flow, resulting in a mean-flow-corrected wave equation. To recover this occurrence of irrotational, isentropic flow, the acoustic wave is related to the velocity potential, thereby combining the fluid dynamics equations into what is known as the convected acoustic wave equation, or the acoustic velocity potential equation [112].

Presently, an alternative derivation to the one presented in Chapter 3 will be shown, as outlined by Campos [88], which begins by taking advantage of a central concept from potential flow theory, known as the acoustic velocity potential, ϕ, which can be manipulated to solve for the acoustic velocity

$$\hat{\boldsymbol{u}} = \nabla\varphi \tag{C.2}$$

and the acoustic pressure,

$$\hat{p} = -\rho_0\frac{\mathrm{d}\varphi}{\mathrm{d}t} \tag{C.3}$$

Regardless of which acoustic wave equation is being solved, expressing it in terms of the velocity potential allows for more straightforward calculations of other flow variables than solving it with a specific flow variable.

With this motivation at hand, the acoustic kinetic energy per unit volume is defined as

$$E_v \equiv \frac{1}{2}\rho_0 v^2 = \frac{1}{2}\rho_0 (\nabla\varphi)^2 \tag{C.4}$$

which is displayed here both with the acoustic velocity and the gradient of the acoustic velocity potential from Eq. (C.2). Likewise, compression energy is shown to be

$$E_p = \frac{p^2}{2\rho_0 a_0^2} = \frac{1}{2}\left(\frac{\rho_0}{a_0^2}\right)\left(\frac{d\varphi}{dt}\right)^2 \tag{C.5}$$

where Eq. (C.3) is substituted to show the role of the acoustic velocity potential here. The difference between (C.4) and (C.5) is then defined as the acoustic Langrangian, shown here as

$$L\left(\varphi;\dot{\varphi},\nabla\varphi;\vec{x},t\right) = E_v - E_p = \frac{1}{2}\rho_0\left[(\nabla\varphi)^2 - a_0^{-2}\dot{\varphi}^2\right] \tag{C.6}$$

where the Lagrangian is explicitly a function of the acoustic velocity potential, position, and time. Furthermore, assuming low Mach number potential mean flow, the Lagrangian can be recast as

$$L = \frac{1}{2}\rho_0\left\{(\nabla\varphi)^2 - a_0^{-2}\left[\dot{\varphi}^2 + 2\dot{\varphi}\left(\vec{v}_0\cdot\nabla\varphi\right)\right]\right\}, v_0^2 \ll a_0^2 \tag{C.7}$$

Then, borrowing from the calculus of variations as applied to acoustics and a classical understanding of mechanics, the action is, by definition, the space-time integral of the Lagrangian,

$$\delta\int L\left(\varphi;\dot{\varphi},\nabla\varphi;\vec{x},t\right)d^3\vec{x}dt = 0 \tag{C.8}$$

When the first variation is removed, the Euler-Lagrange equation reveals itself to be

$$\frac{\partial\left(\partial L/\partial\dot{\varphi}\right)}{\partial t} + \nabla\cdot\left[\frac{\partial L}{\partial\left(\nabla\varphi\right)}\right] = 0 \tag{C.9}$$

which, when Eq. (C.7) is substituted into Eq. (C.9), results in the convected acoustic wave equation,

$$\frac{\partial}{\partial t}\left[\rho_0 a_0^{-2}\left(\dot{\varphi}+\boldsymbol{u}_0\cdot\nabla\varphi\right)\right]+\nabla\left(\rho_0 a_0^{-2}\dot{\varphi}\boldsymbol{u}_0\right)-\nabla\cdot\left(\rho_0\nabla\varphi\right)=0 \tag{C.10}$$

Neglecting the mean flow effects, Eq. (C.10) readily reduces back to Eq. (C.1).

Appendix D

Additional Bidirectional Vortex Engine Acoustic, Vortical, and Energy Plots

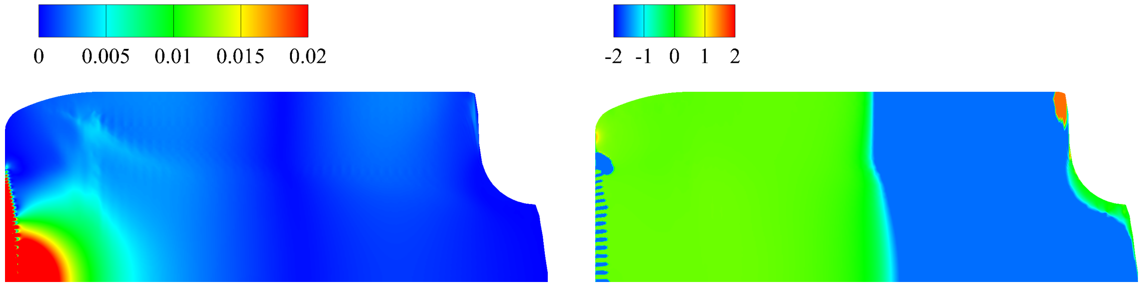

(a) Streamwise velocity magnitude [m/s].   (b) Streamwise velocity phase [rad].

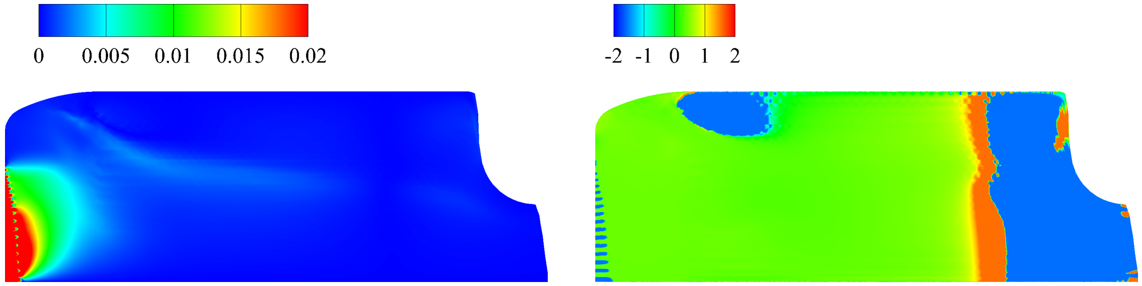

(c) Normal velocity magnitude [m/s].   (d) Normal velocity phase [rad].

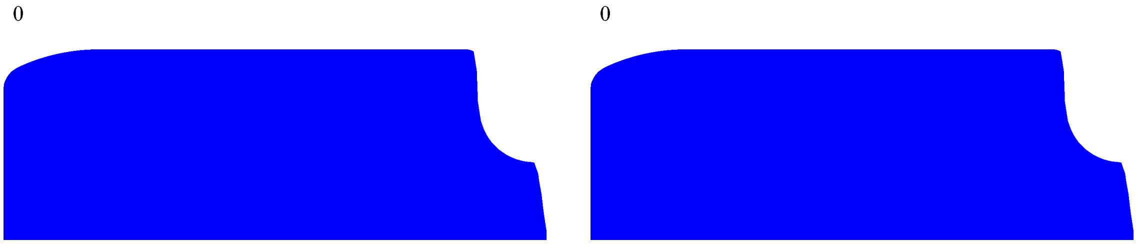

(e) Azimuthal velocity magnitude [m/s].   (f) Azimuthal velocity phase [rad].

Figure D.1: Acoustic velocities for the 2L mode with reacting flow.

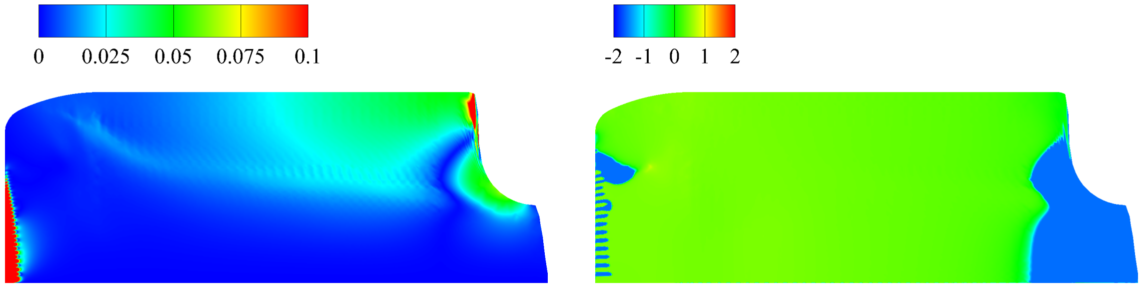

(a) Streamwise velocity magnitude [m/s]. (b) Streamwise velocity phase [rad].

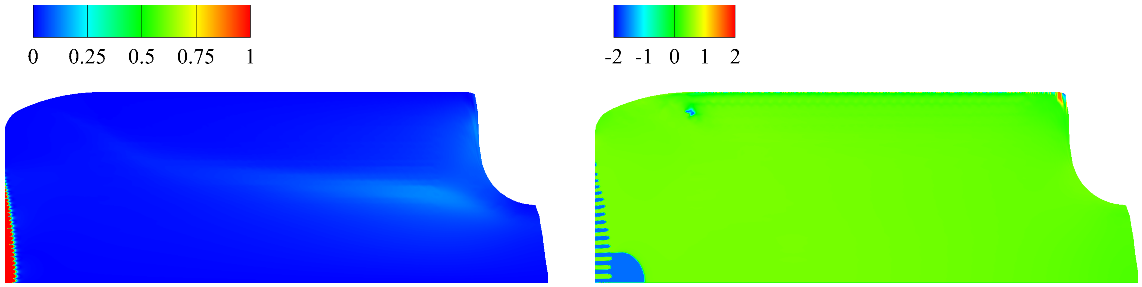

(c) Normal velocity magnitude [m/s]. (d) Normal velocity phase [rad].

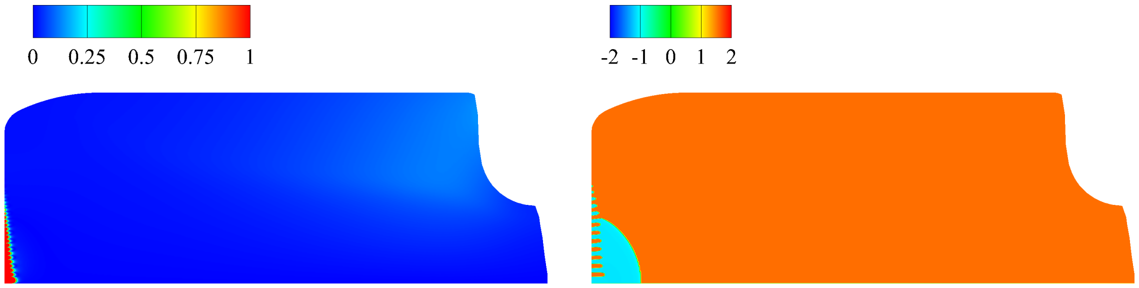

(e) Azimuthal velocity magnitude [m/s]. (f) Azimuthal velocity phase [rad].

Figure D.2: Acoustic velocities for the 2T mode with reacting flow.

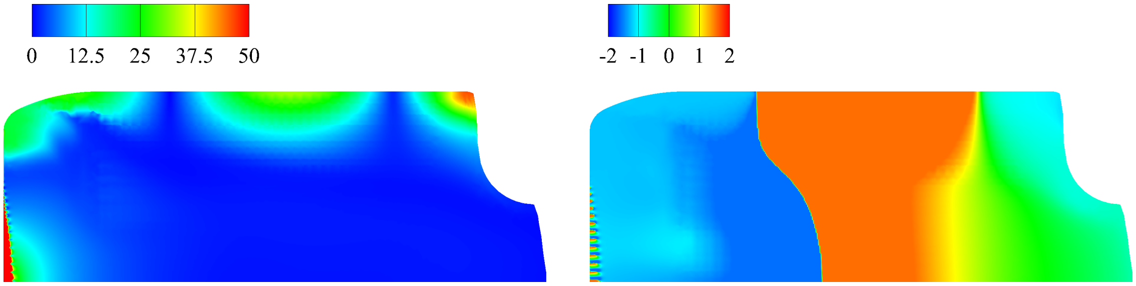

(a) Pressure magnitude [Pa].

(b) Pressure phase [rad].

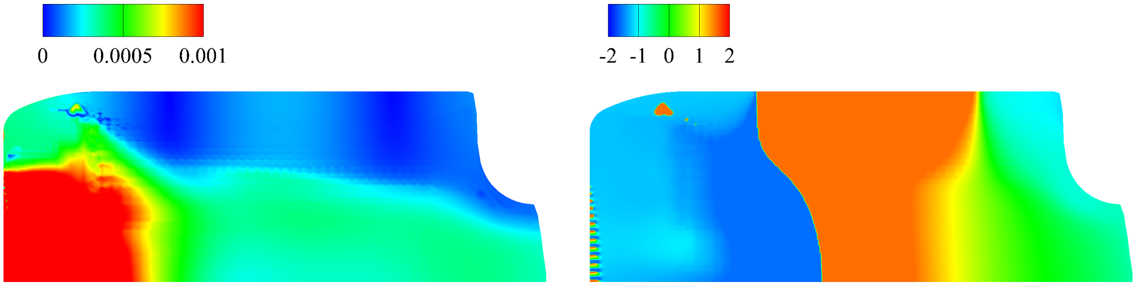

(c) Temperature magnitude [K].

(d) Temperature phase [rad].

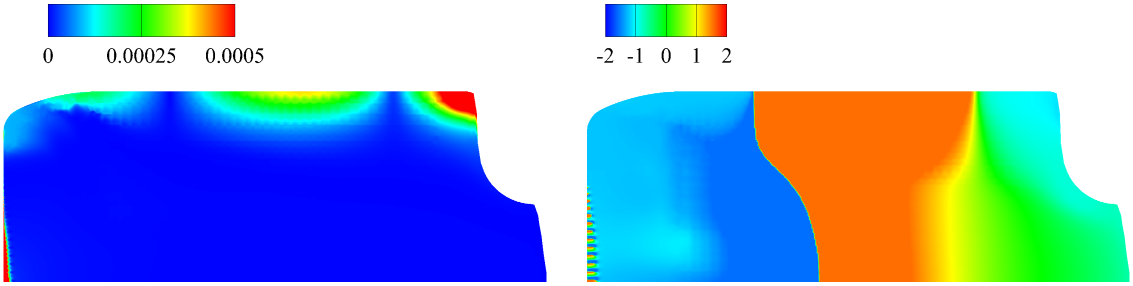

(e) Density magnitude [kg/m^3].

(f) Density phase [rad].

Figure D.3: Acoustic pressure, density, and temperature profiles for the 2L mode with reacting flow.

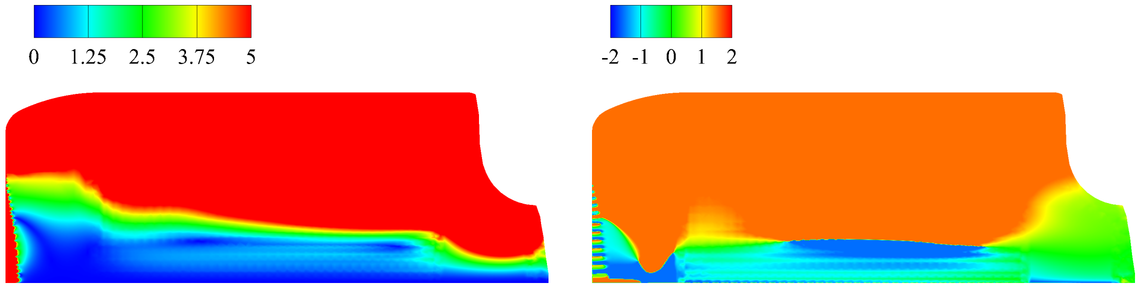

(a) Pressure magnitude [Pa].

(b) Pressure phase [rad].

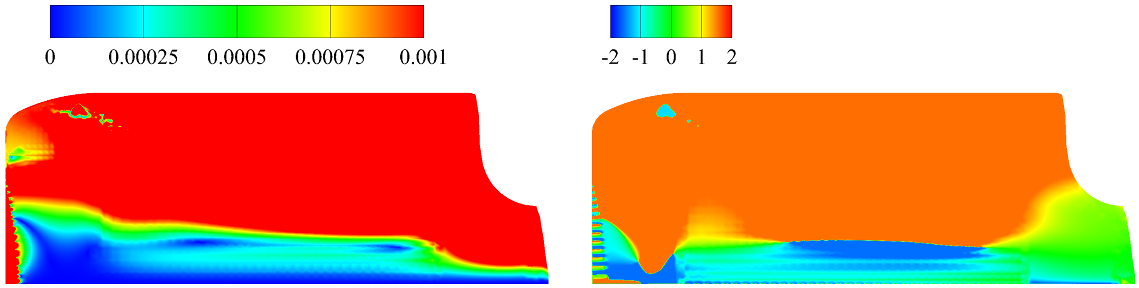

(c) Temperature magnitude [K].

(d) Temperature phase [rad].

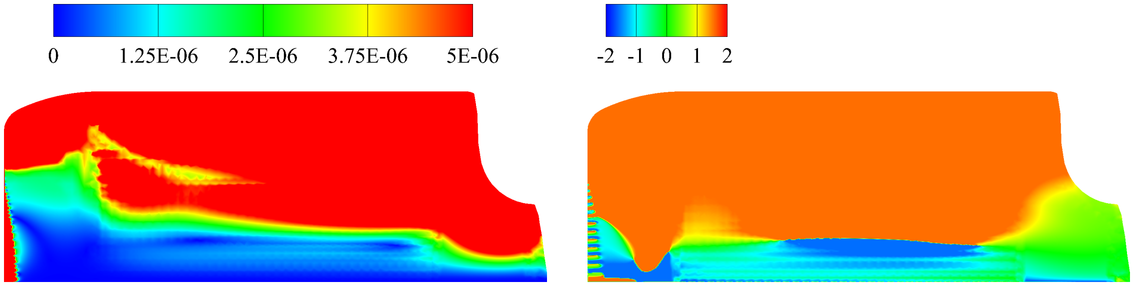

(e) Density magnitude [kg/m^3].

(f) Density phase [rad].

Figure D.4: Acoustic pressure, density, and temperature profiles for the 2T mode with reacting flow.

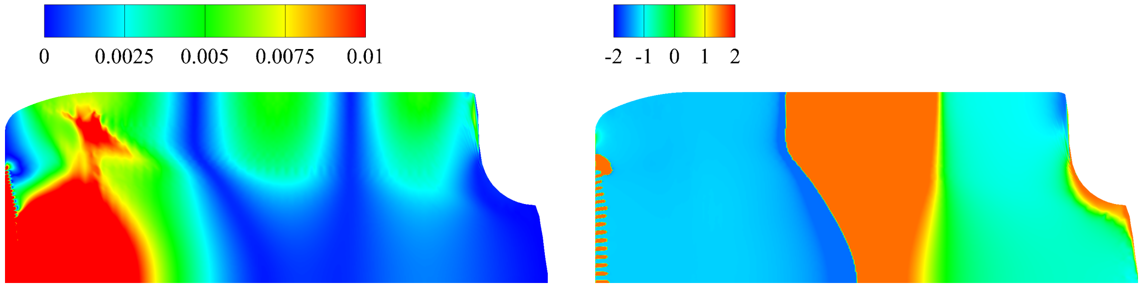

(a) Streamwise velocity magnitude [m/s].

(b) Streamwise velocity phase [rad].

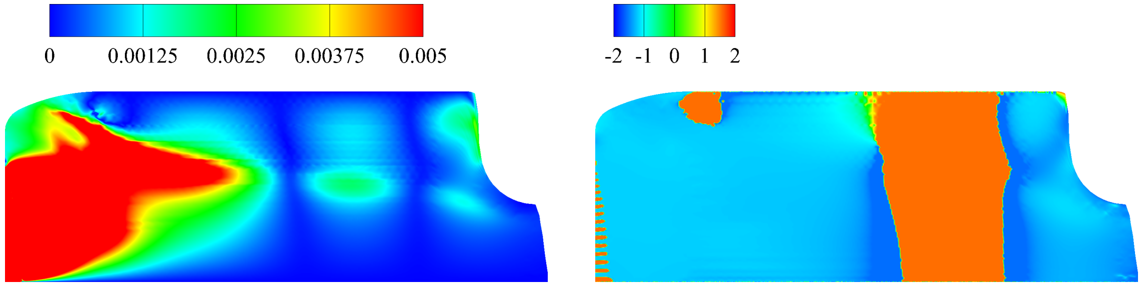

(c) Normal velocity magnitude [m/s].

(d) Normal velocity phase [rad].

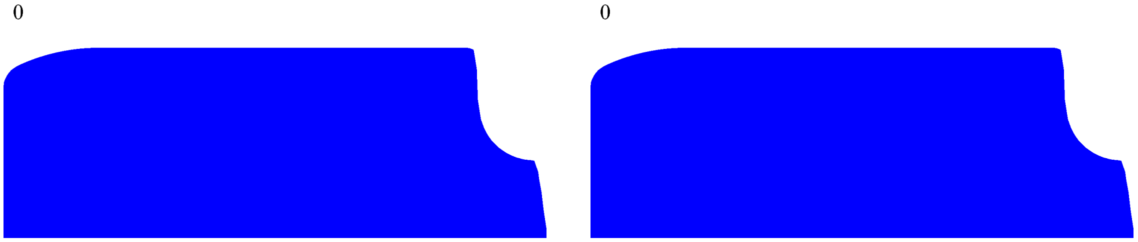

(e) Azimuthal velocity magnitude [m/s].

(f) Azimuthal velocity phase [rad].

Figure D.5: Acoustic velocities for the 3L mode with reacting flow.

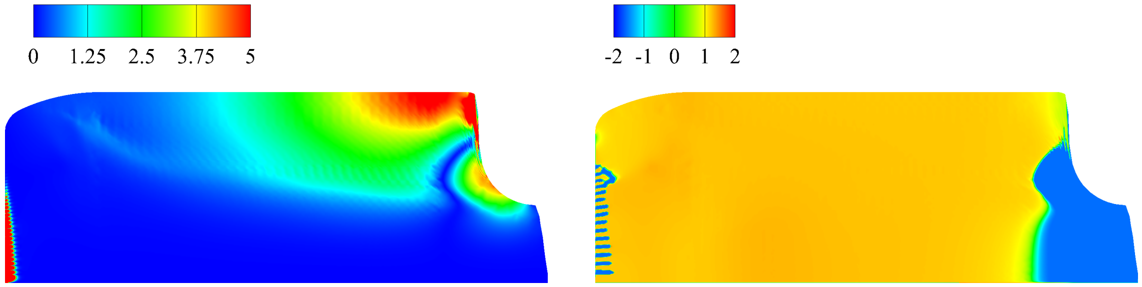

(a) Streamwise velocity magnitude [m/s]. (b) Streamwise velocity phase [rad].

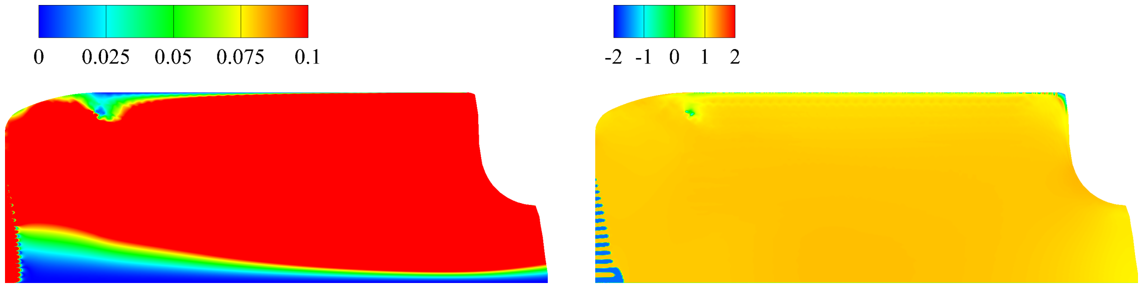

(c) Normal velocity magnitude [m/s]. (d) Normal velocity phase [rad].

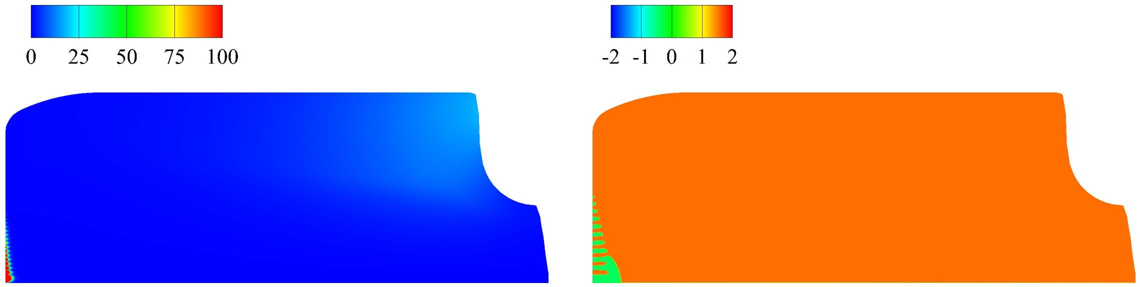

(e) Azimuthal velocity magnitude [m/s]. (f) Azimuthal velocity phase [rad].

Figure D.6: Acoustic velocities for the 3T mode with reacting flow.

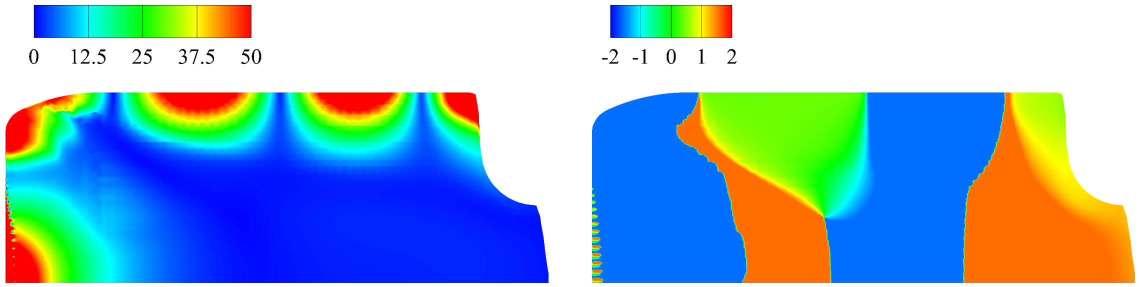

(a) Pressure magnitude [Pa].
(b) Pressure phase [rad].

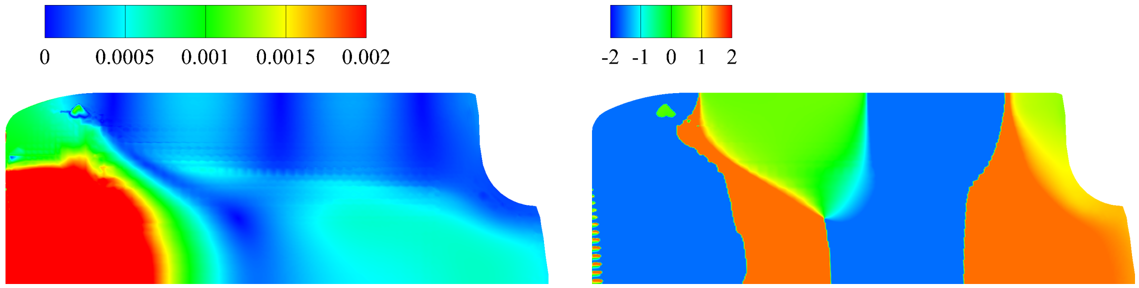

(c) Temperature magnitude [K].
(d) Temperature phase [rad].

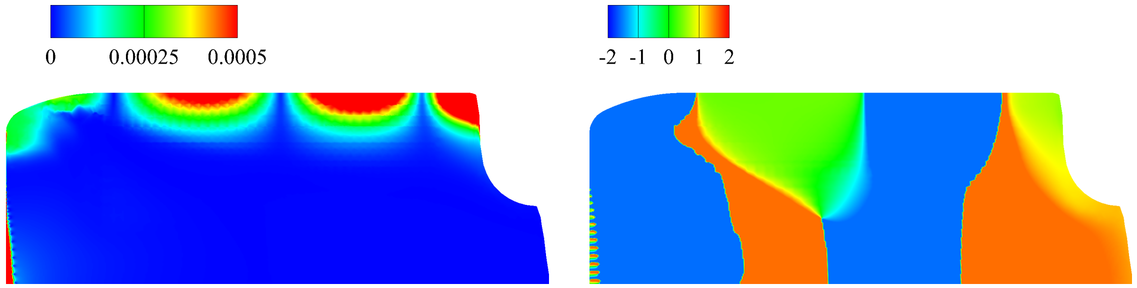

(e) Density magnitude [kg/m^3].
(f) Density phase [rad].

Figure D.7: Acoustic pressure, density, and temperature profiles for the 3L mode with reacting flow.

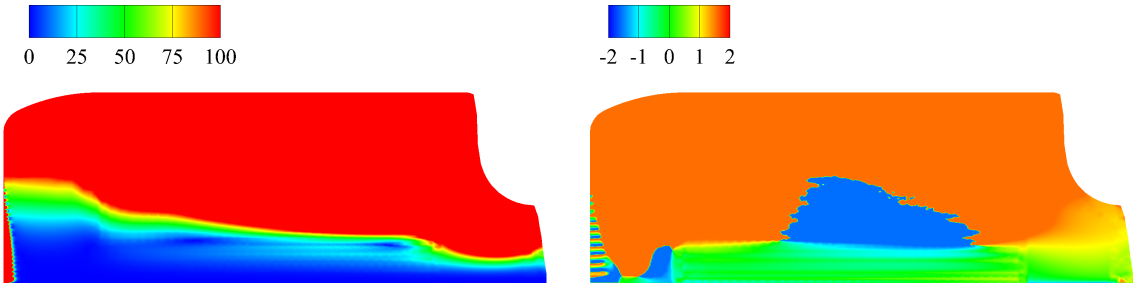

(a) Pressure magnitude [Pa]. (b) Pressure phase [rad].

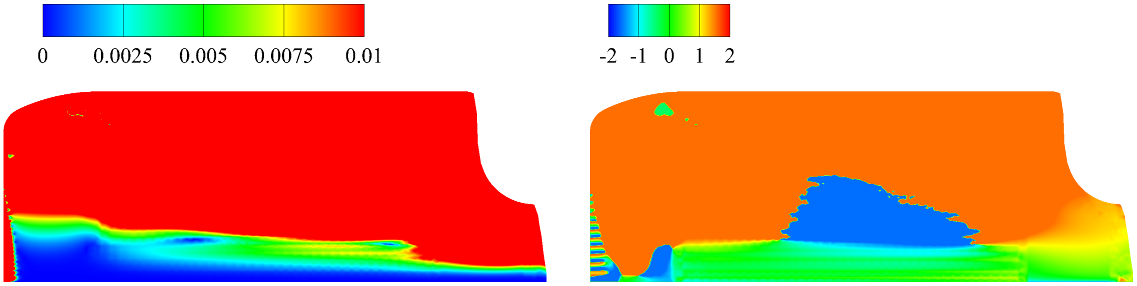

(c) Temperature magnitude [K]. (d) Temperature phase [rad].

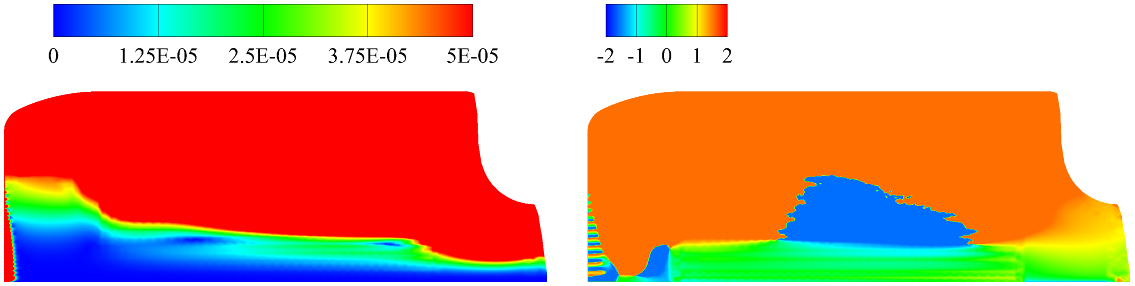

(e) Density magnitude [kg/m^3]. (f) Density phase [rad].

Figure D.8: Acoustic pressure, density, and temperature profiles for the 3T mode with reacting flow.

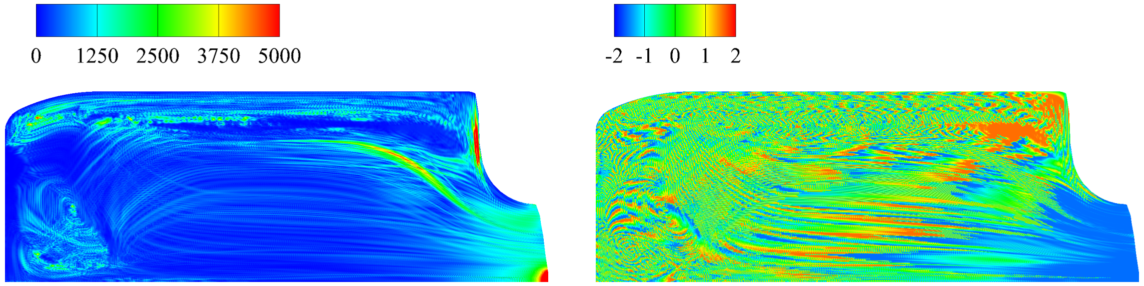

(a) Streamwise velocity magnitude [m/s].

(b) Streamwise velocity phase [rad].

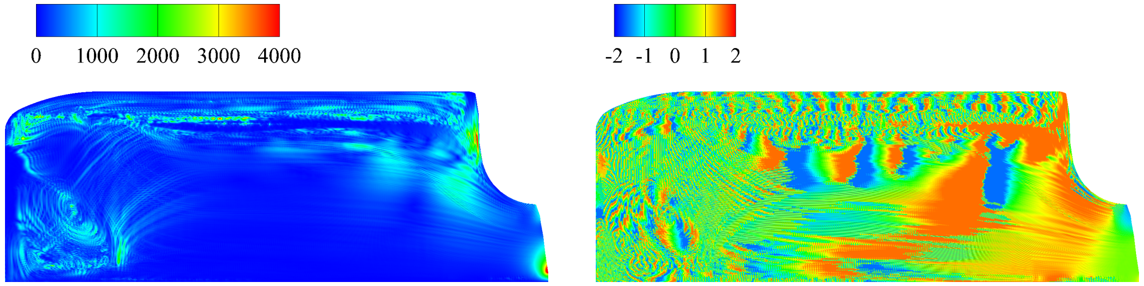

(c) Normal velocity magnitude [m/s].

(d) Normal velocity phase [rad].

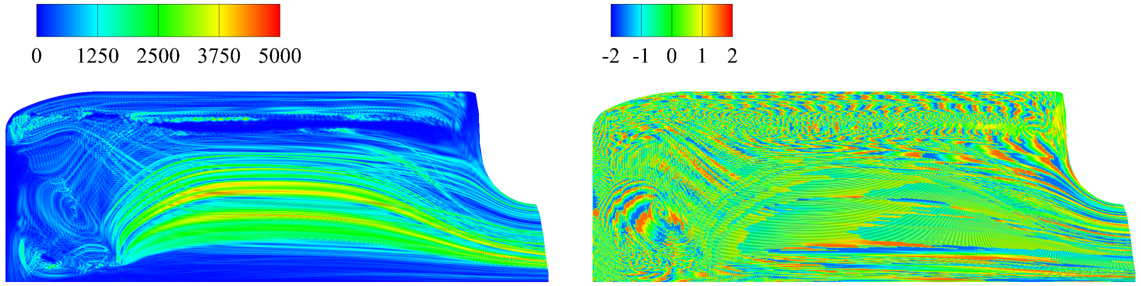

(e) Azimuthal velocity magnitude [m/s].

(f) Azimuthal velocity phase [rad].

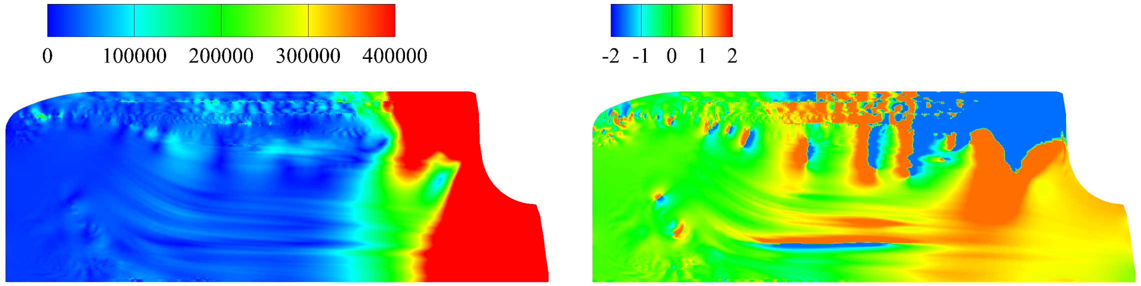

(g) Pressure magnitude [Pa].

(h) Pressure phase [rad].

Figure D.9: Vortical velocities for the 2L mode.

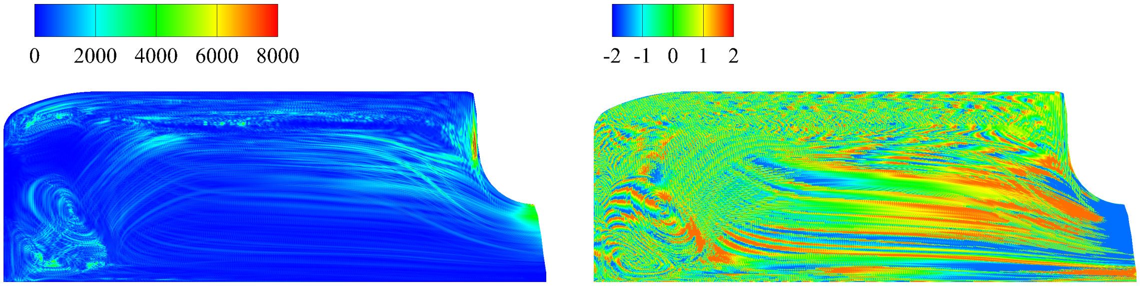

(a) Streamwise velocity magnitude [m/s]. (b) Streamwise velocity phase [rad].

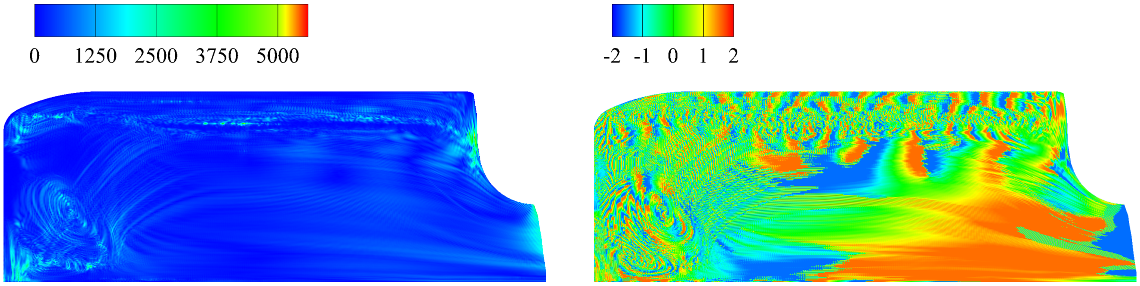

(c) Normal velocity magnitude [m/s]. (d) Normal velocity phase [rad].

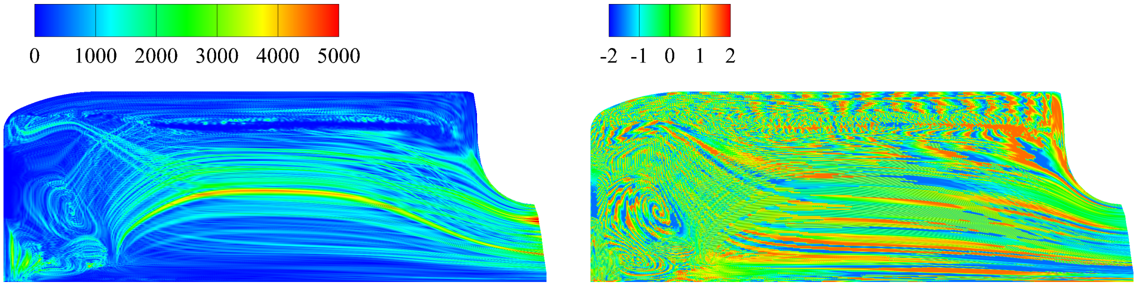

(e) Azimuthal velocity magnitude [m/s]. (f) Azimuthal velocity phase [rad].

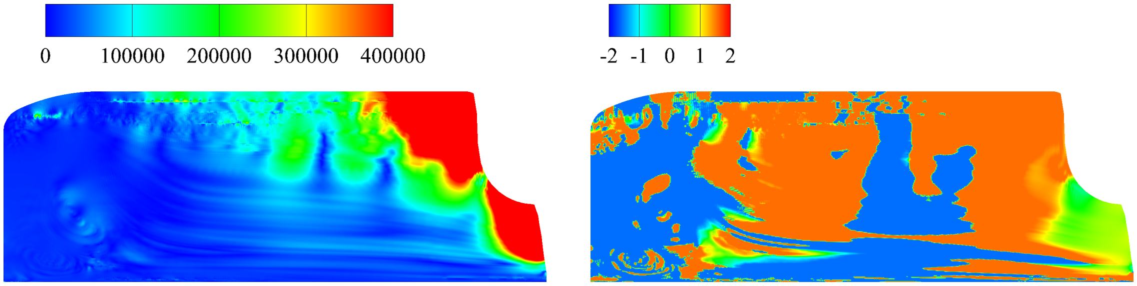

(g) Pressure magnitude [Pa]. (h) Pressure phase [rad].

Figure D.10: Vortical velocities for the 2T mode.

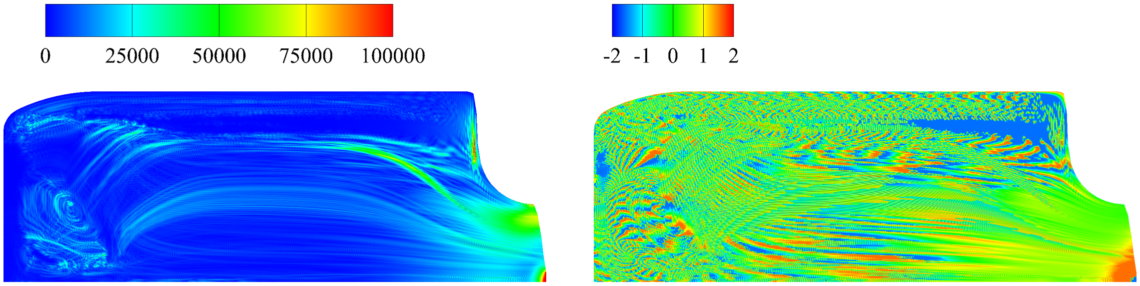

(a) Streamwise velocity magnitude [m/s].

(b) Streamwise velocity phase [rad].

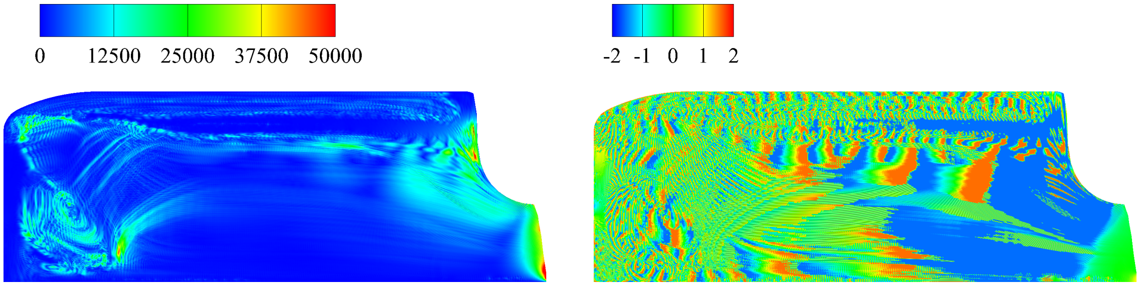

(c) Normal velocity magnitude [m/s].

(d) Normal velocity phase [rad].

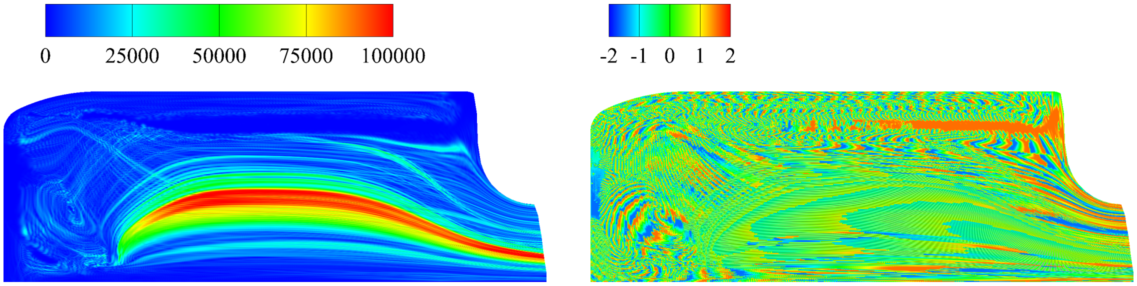

(e) Azimuthal velocity magnitude [m/s].

(f) Azimuthal velocity phase [rad].

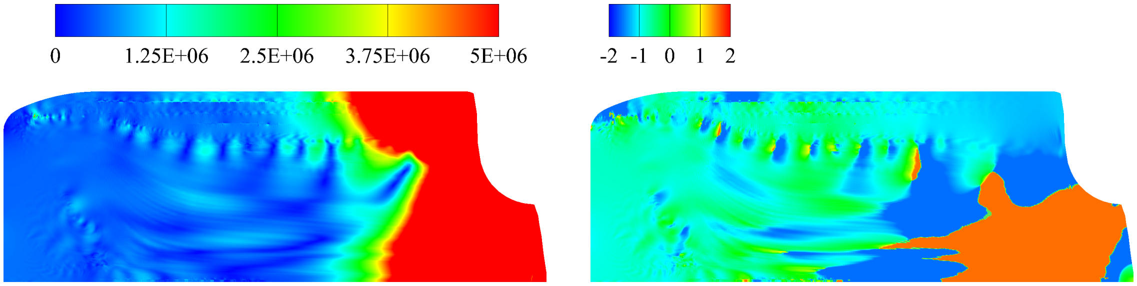

(g) Pressure magnitude [Pa].

(h) Pressure phase [rad].

Figure D.11: Vortical velocities for the 3L mode.

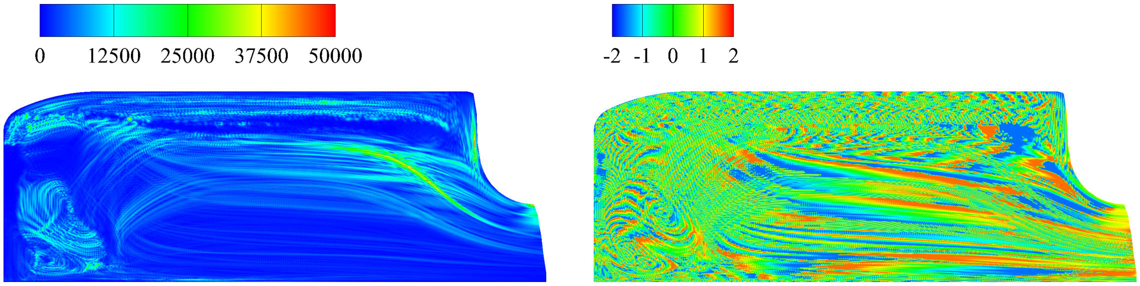

(a) Streamwise velocity magnitude [m/s]. (b) Streamwise velocity phase [rad].

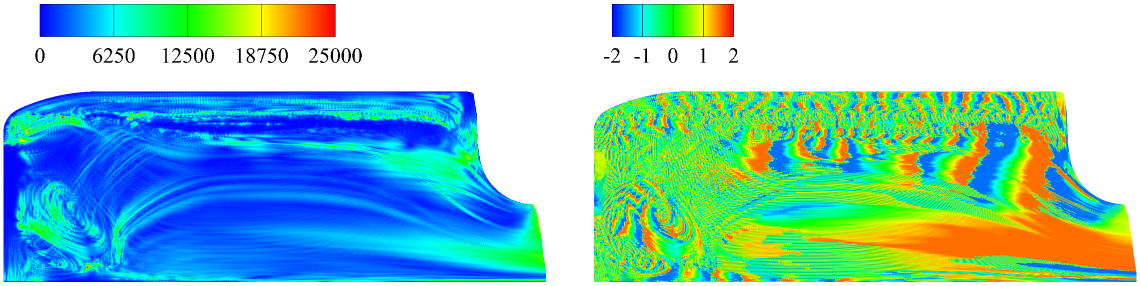

(c) Normal velocity magnitude [m/s]. (d) Normal velocity phase [rad].

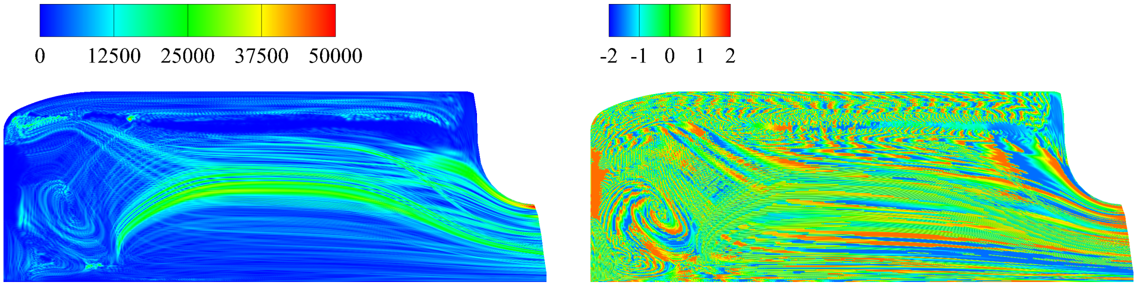

(e) Azimuthal velocity magnitude [m/s]. (f) Azimuthal velocity phase [rad].

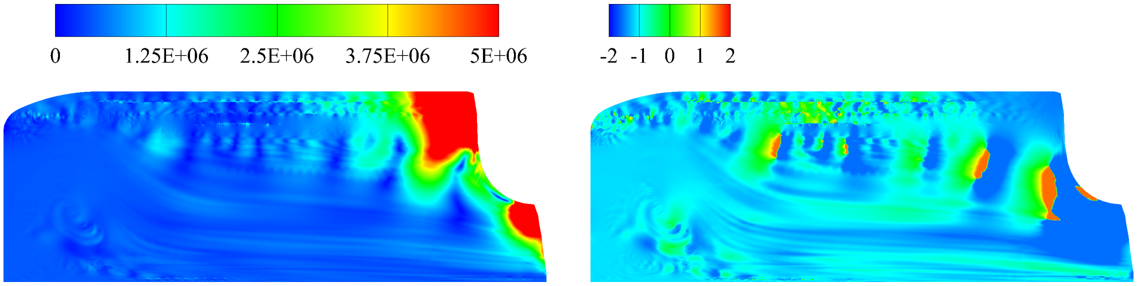

(g) Pressure magnitude [Pa]. (h) Pressure phase [rad].

Figure D.12: Vortical velocities for the 3T mode.

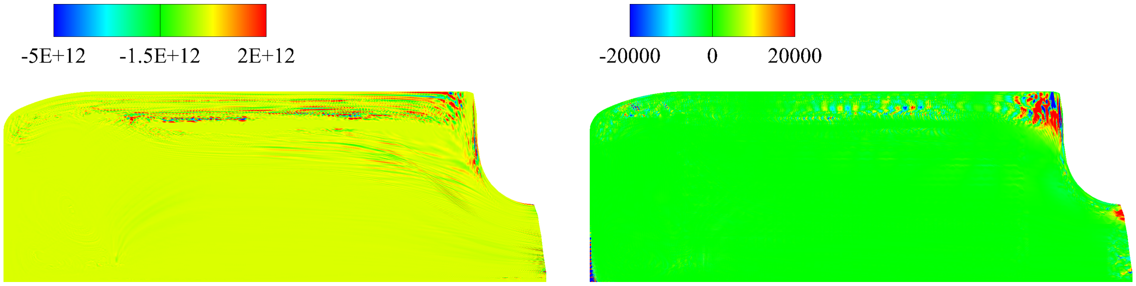

(a) Vortex shedding [W/m^3].

(b) Flow turning [W/m^3].

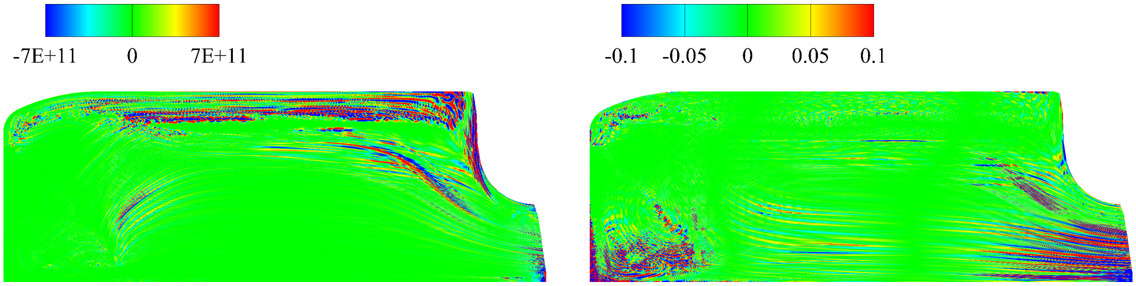

(c) Surface work [W/m^3].

(d) Dissipation [W/m^3].

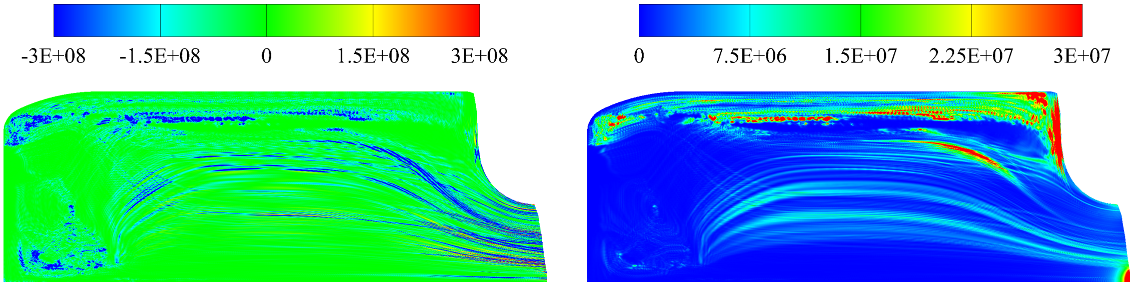

(e) Viscous effects [W/m^3].

(f) E_m^2 [J/m^3].

Figure D.13: Energy integrands for the 2L mode.

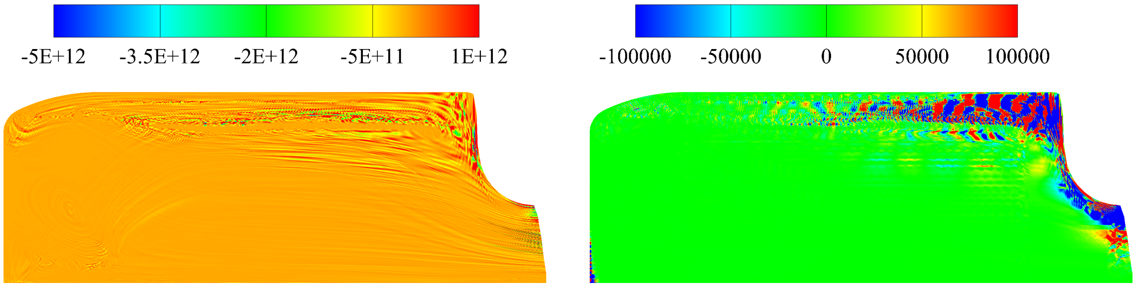

(a) Vortex shedding [W/m^3]. (b) Flow turning [W/m^3].

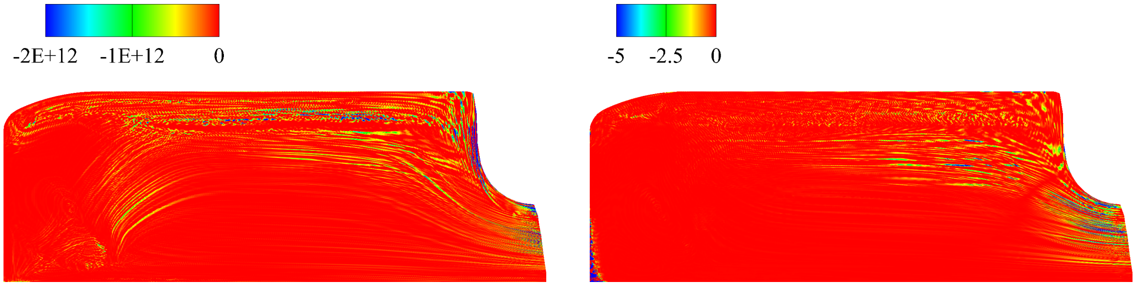

(c) Surface work [W/m^3]. (d) Dissipation [W/m^3].

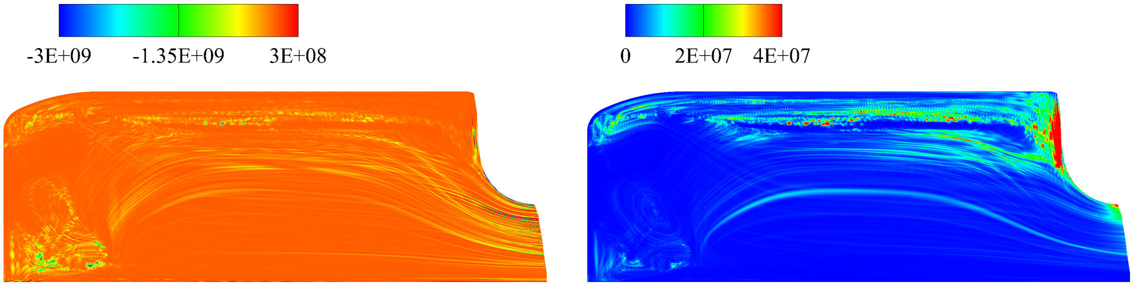

(e) Viscous effects [W/m^3]. (f) E_m^2 [J/m^3].

Figure D.14: Energy integrands for the 2T mode.

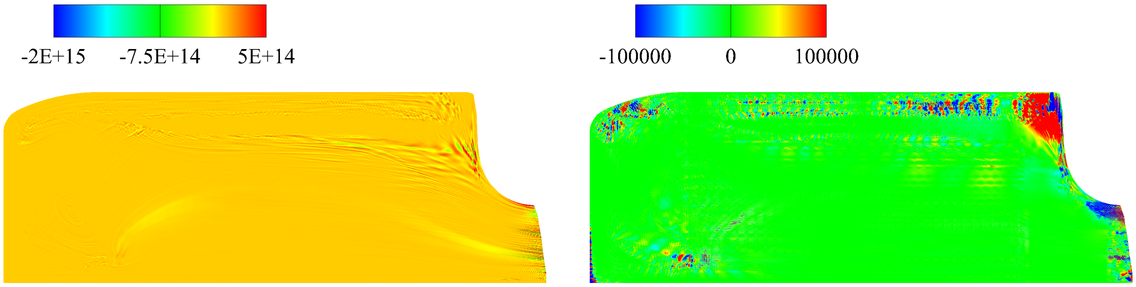

(a) Vortex shedding [W/m^3]. (b) Flow turning [W/m^3].

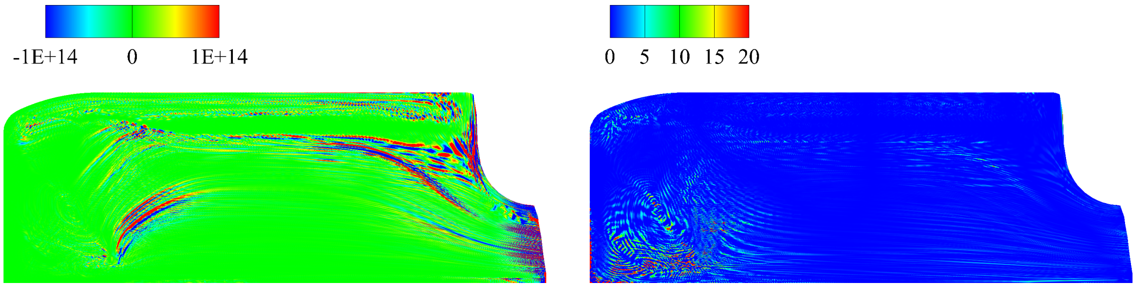

(c) Surface work [W/m^3]. (d) Dissipation [W/m^3].

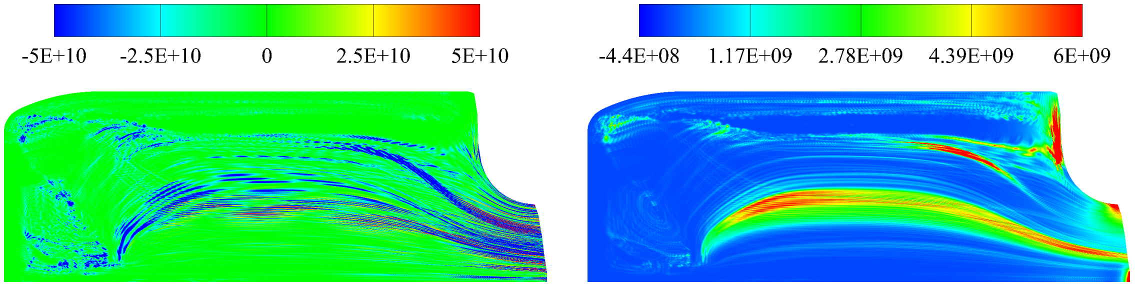

(e) Viscous effects [W/m^3]. (f) E_m^2 [J/m^3].

Figure D.15: Energy integrands for the 3L mode.

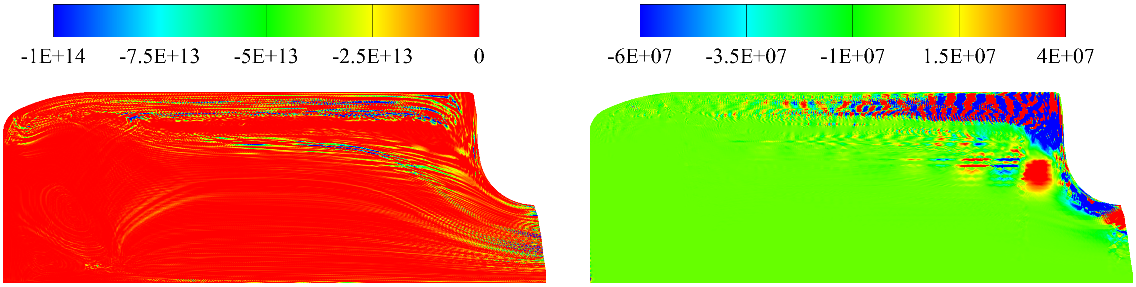

(a) Vortex shedding [W/m^3]. (b) Flow turning [W/m^3].

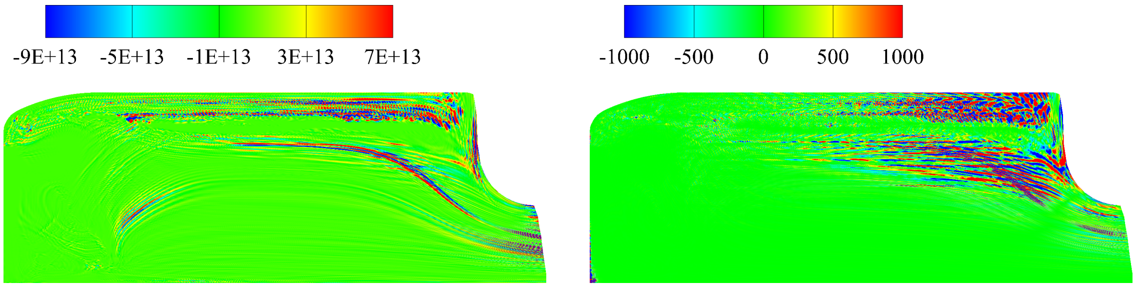

(c) Surface work [W/m^3]. (d) Dissipation [W/m^3].

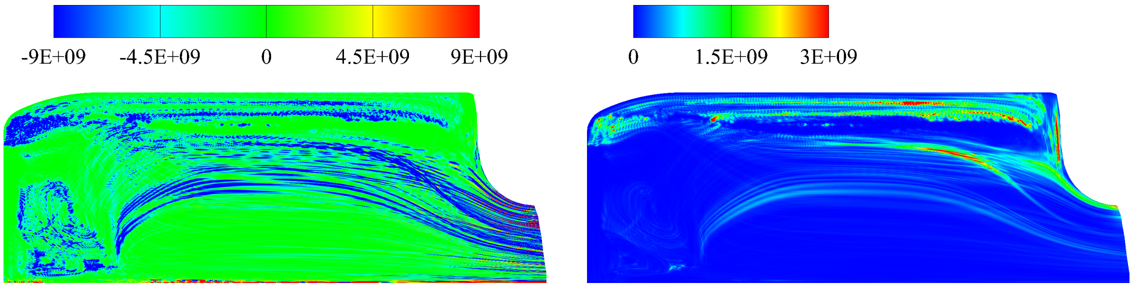

(e) Viscous effects [W/m^3]. (f) E_m^2 [J/m^3].

Figure D.16: Energy integrands for the 3T mode.